Model-Based Ultrasound Imaging for Challenging Acoustic Clutter Suppression

By

Kazuyuki Dei

Dissertation

Submitted to the Faculty of the

Graduate School of Vanderbilt University

in partial fulfillment of the requirements

for the degree of

DOCTOR OF PHILOSOPHY

in

Biomedical Engineering

February 28, 2019

Nashville, Tennessee

Approved:

Brett C. Byram, Ph.D.

Daniel B. Brown, M.D.

Charles F. Caskey, Ph.D.

William A. Grissom, Ph.D.

Michael I. Miga, Ph.D.

To my wife, Karen

and

To all our animals, Feng, Muppet, Buttercups, Sarge, Maisey and Sunny

ACKNOWLEDGMENTS

First and foremost, I would like to express my sincere gratitude for my advisor, Professor Brett Byram, who took a chance with me as his very first graduate student and who gave me an opportunity I could never have imagined. Without his guidance and encouragement, I would not have survived through all the research, writing, manuscripts, abstracts and proceedings that has led to this dissertation.

I would also like to thank all members of my Ph.D. committee: Professor Daniel Brown, Professor Charles Caskey, Professor William Grissom, and Professor Michael Miga, for their insight, time and consideration throughout the qualifying and defense examinations.

I am also grateful to the members of the Biomedical Elasticity and Acoustic Measurement Laboratory (BEAM Lab), which is where I have spent all of my time for the past five years. In particular, many thanks go to Jaime Tierney and Kristy Walsh for sharing their perspectives, encouragement and motivation. Also, a special thanks to Douglas Dumont for his many help and suggestion, especially, when I was extremely nervous at my first conference. I also thank all of the BEAM Lab members in for stimulating discussion and suggestion. Also, I thank Marko Jakovljevic and Will Long for their help on development of a channel data acquisition tool.

I would like to thank the National Institutes of Health for funding my graduate study through research project grants R01-EB020040 and S10OD016216-01. I would like to thank the Ultrasound Division at Siemens Medical Solutions USA Inc. for their in-kind support. I would also like to thank the Vanderbilt Advanced Computing Center for Research and Education (ACCRE) for providing the high-performance computing resources, along with their endless support.

TABLE OF CONTENTS

LIST OF TABLES

LIST OF FIGURES

Chapter 1

BACKGROUND AND INTRODUCTION

Ultrasound is one of the most widely used imaging modalities in medicine [5]. It is non-invasive, real-time and relatively inexpensive when compared with other modalities, like magnetic resonance imaging (MRI) and computed tomography (CT). Ultrasound images are tomographic, offering cross-sectional views of tissue structures [3].

1.1 Clinical Motivation

For decades, ultrasound has been used as a general diagnostic tool with an excellent safety record. Because it is also a real-time imaging method and is readily accessible and affordable, numerous ultrasound applications in the medical field have evolved, including fetal, abdominal, vasculature and cardiac imaging [6].

The ability to provide a real-time high quality ultrasound image is crucial for practical use in a clinical setting because it enables clinicians to diagnose patients quickly, accurately and safely. However, today's high-end clinical ultrasound systems still have limitations associated with image quality *in vivo*, especially when scanning patients who are obese. Such patients possess a large amount of fat in the subcutaneous layer of skin, which is where aberration and reverberation occur. Recent studies have identified aberration and reverberation as primary sources of ultrasound image degradation and artifacts [2, 7]. For these reasons, ultrasound images of obese patients are often of poor and inadequate quality. We, therefore, refer to them as "difficult-to-image" patients [8].

Obesity is a global epidemic affecting many countries of the world [9]. More than half a billion adults worldwide were obese in 2008, an increase of over 100% since 1980 [10]. In the United States, 34.2% of adults were obese in 2012 [11]. Such a dramatic prevalence of obesity is substantially problematic for ultrasound imaging as a diagnostic tool.

Over the past few decades, technology advances have enabled transition from a diagnostic tool to use as a guidance tool for clinical applications, including radiation therapy, ablation treatment and percutaneous biopsy [12]. The role of image-guided intervention in cancer patients has grown dramatically [13]. Ultrasound also plays an important role in image-guided interventional radiology, as a non-invasive and real-time imaging technique.

Ultrasound is used extensively to guide percutaneous biopsies, offering convenience to patients and clinicians, real-time dynamic observation and high availability [14], and it does not expose the patient to ionizing radiation, as a CT scan would. However, conventional ultrasound images are still often of poor quality when compared to CT and MRI images. This may be worse in the presence of an acoustic bright needle, and in general, high levels of clutter will blur images. A poor ultrasound image may cause clinicians to misplace a biopsy needle and increase the number of biopsy passes necessary, therefore impairing the usefulness and benefits of ultrasound when considering efficiency and patient comfort.

1.2 Foundations of Ultrasound Imaging

This section describes fundamental principles of ultrasound imaging, typically, referred to as brightness-mode (B-mode) imaging.

1.2.1 Conventional Beamforming

Ultrasound imaging uses a pulse-echo technique in which short-duration pulses are transmitted into the field of interest, and echo signals reflected from scattering are detected and displayed. Transmitted waves of ultrasound are typically fired with delay on the individual aperture elements so that propagating waves can generate a focused ultrasound beam along the path of transmission, as shown in Fig. 1.1 (a).

Some waves are reflected back (i.e., backscattered) to the transducer and the others either continue to propagate deeper or are absorbed within the propagating media. The

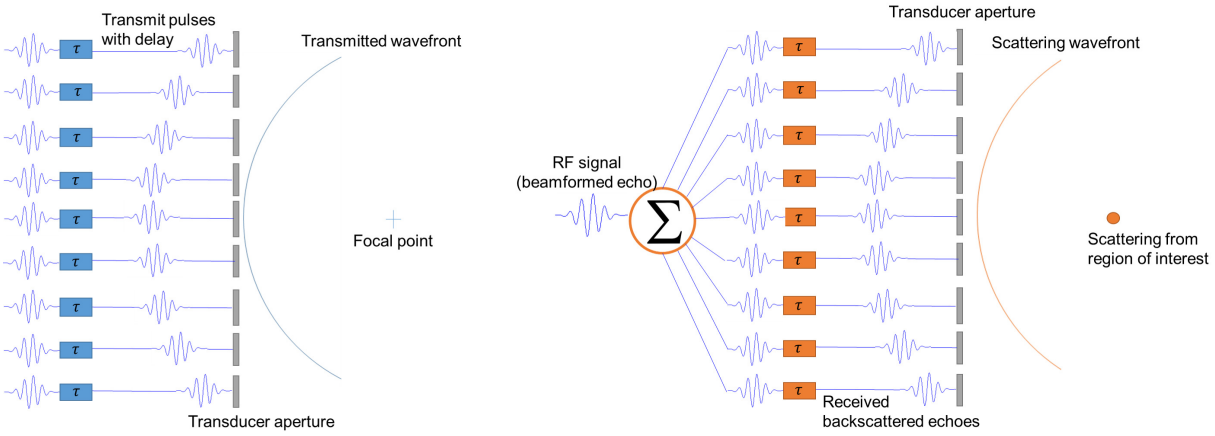

(a) Transmit (b) Receive

Figure 1.1: Conventional delay-and-sum (DAS) beamforming to form ultrasound image using (a) transmitted pulses with delay and focal point, (b) received reflected echo signals scattering from the region of interest [1].

reflected echo signals are received on each aperture element. The received signals are delayed and summed to generate a received ultrasound beam or RF signal (i.e., beamformed echo) as illustrated in Fig. 1.1 (b). This method is conventional beamforming, which is also known as delay-and-sum (DAS) beamforming.

In the process of DAS beamforming, received signals before delay are commonly referred to as undelayed channel data, whereas delayed channel data represents the delayed received signals. We also call channel data aperture domain signals. Fig. 1.2 illustrates an example of (a) undelayed and (b) delayed channel data. The undelayed channel data shows wavefront of scattering signal from a point source in the region of interest. The wave equation with a point source can be written as [15],

$$\nabla^2 p - \frac{1}{c^2}\frac{\partial^2 p}{\partial t^2} = \delta(r - r_0, t), \tag{1.1}$$

where c is the speed of sound (typically, 1540 m/s in soft tissues [5]), r_0 is the point source location, and $\delta(r - r_0, t)$ is the Dirac delta function, with a value of zero for all values of r except for $r = r_0$. To solve the wave equation, we use a Green's function, and consequently,

$$G(k|r - r_0|) = p(|r - r_0|, t) = \frac{1}{4\pi}\frac{e^{-jkR}}{R}, \tag{1.2}$$

where $R = |r - r_0|$ and $k = \frac{\omega}{c}$ is the wavenumber. It shows that scattering echo signals (i.e., pressure waves) from a point source have spherical wavefront, originally indicated by Huygens and Sommerfeld [16]. The curvature shape of the wavefront shown in Fig. 1.2 (a) is consistent with the analytical equation.

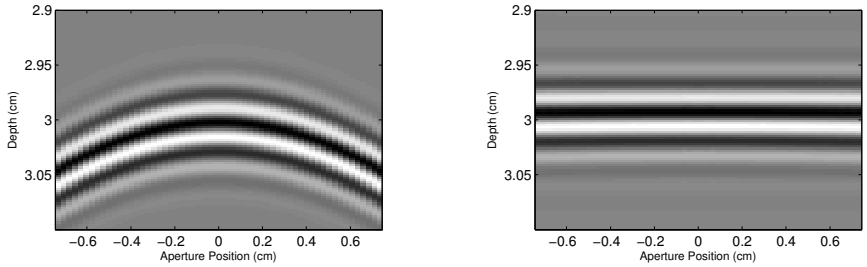

(a) Undelayed (b) Delayed

Figure 1.2: (a) Undelayed Channel Data, (b) Delayed Channel Data.

For a conventional ultrasound system using DAS beamforming, the point spread function (PSF) represents the image response produced by a point source at a particular position in the field (i.e., a two-dimensional (2-D) PSF corresponds to the system response). Fig. 1.3 demonstrates the PSF simulated by Field II with a point source positioned at 3 cm depth. The transducer is modeled with 3 MHz center frequency, 60% fractional bandwidth and a $f/2$ system. Field II is a simulation tool for ultrasound transducer fields and ultrasound imaging based on linear acoustics [17, 18]. Fig. 1.3 (a) and (b) represent the 2-D PSF with no apodization and the lateral PSFs, including rectangular (abbreviated as rect), hamming and gaussian apodization functions (Fig. 1.3(c)). The apodization is a weighted windowing function applied to reduce the side lobe relative to the main lobe (better contrast), while increasing the width of the main lobe (lower resolution). Fig. 1.3 (b) shows that the lateral PSF with no apodization has a narrower main lobe, while the PSFs with hamming and gaussian apodization functions indicate a lower side lobe.

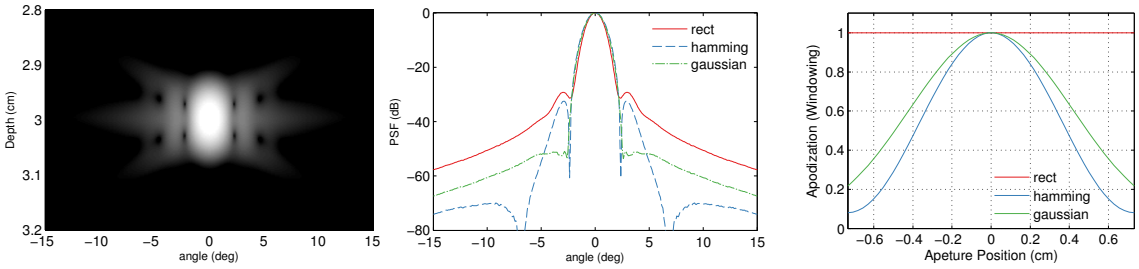

(a) 2-D PSF (b) PSFs (c) Apodization Functions

Figure 1.3: (a) Image of 2-D PSF with no apodization, (b) Plot of PSF with no apodization (i.e., rect), hamming and gaussian, and (c) Plot of apodization functions.

1.2.2 Ultrasound Image Quality Metrics

In ultrasound, spatial resolution and contrast are two well-known image quality metrics in judging and comparing the performance of an ultrasound imaging system. When using a 1-D transducer array to reconstruct a 2D ultrasound image, both axial and lateral resolution are estimated from the operating conditions for the transducer and the ultrasound system used when acquiring imaging data. For example, because the minimal required spatial separation between two reflectors is one-half of spatial pulse length (SPL) to avoid any overlap of returning echoes [3], axial resolution, denoted as res_{axl}, should be given by,

$$res_{axl} = \frac{SPL}{2} = \frac{\lambda_w}{2}\frac{\#ofcycles}{pulse}, \tag{1.3}$$

where the SPL is the number of cycles per transmitted pulse multiplied by the wavelength that is denoted as λ_w. The lateral resolution (res_{lat}) is characterized by the f-number, $f\#$, of the transducer (i.e., the ratio of the focal depth (z_f) to the aperture length (D)), expressed as,

$$res_{lat} = \lambda_w f\# = \lambda_w \frac{z_f}{D}. \tag{1.4}$$

However, when quantifying both axial and lateral resolution, we typically report the full-width at half-maximum (FWHM) of the axial and lateral beam profiles using uncompressed

envelope data.

To assess the contrast performance quantitatively, contrast (sometimes, referred to as contrast ratio (CR)) and contrast-to-noise ratio (CNR) are often used [15]. Both metrics are computed using two specific regions, as shown in Fig. 1.3, with given equations,

$$C = -20 \log 10(\frac{\mu_L}{\mu_B}), \tag{1.5}$$

$$CNR = 20 \log 10(\frac{|\mu_L - \mu_B|}{\sqrt{\sigma_L^2 + \sigma_B^2}}), \tag{1.6}$$

where (μ_L, σ_L^2) and (μ_B, σ_B^2) denote the value of (mean, variance) of the enveloped but uncompressed data inside (i.e., lesion) and outside (i.e., background) the anechoic or hypoechoic structures, respectively. The definition for contrast-to-noise ratio that we use here is based on a metric that was originally termed contrast-to-speckle ratio [19, 20]. Fundamentally, it is a signal-to-noise ratio, where the signal is a target lesion, $\mu_B - \mu_L$, that is embedded in speckle noise, where the noise is estimated using $\sqrt{\sigma_L^2 + \sigma_B^2}$.

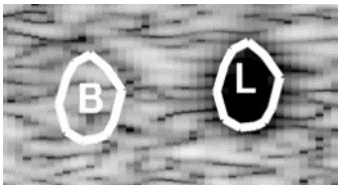

Figure 1.4: An example showing two regions: one is for an anechoic or hypoechoic lesion target and the other for a background, used for computing contrast and contrast-to-noise ratio (CNR).

1.2.3 Ultrasound B-mode Image Formation

Received signals on each individual aperture elements are delayed and summed (i.e., DAS beamforming), as shown in Fig. 1.1 (b). The beamformed signal is called RF data. The RF data is processed to form ultrasound B-mode images. The RF data is Hilbert transformed to obtain the 90° phase shifted signal [21], leading to the I/Q (in-phase and

quadrature) data. The envelope data is the magnitude of the I/Q data. Fig. 1.5 illustrates conventional ultrasound B-mode image formation.

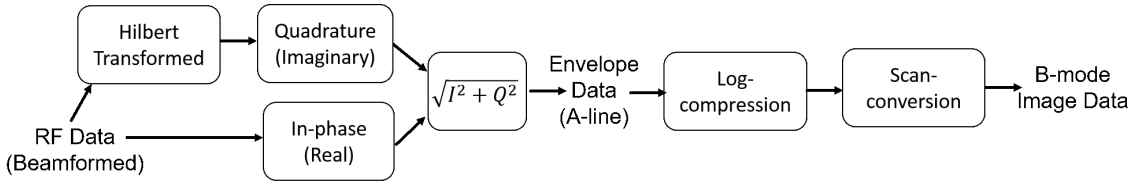

Figure 1.5: Ultrasound B-mode Image Formation after Post-Processing Beamformed RF Data.

1.3 Past, Present and Future of Ultrasound Beamformer

In order to create a real-time high-quality ultrasound image, the ability to steer and focus a transducer array in transmit and receive is significant. In early ultrasound systems, there were limitations on achieving those functions associated with analog electrical circuits. Early analog beamforming ultrasound systems were susceptible to drifting [22]. More than 25 years ago, digitalized devices were introduced. More advanced signal processing schemes were later applied in digital circuits, leading to today's high-end digital beamforming ultrasound systems. Particularly, the availability of advanced high-speed analog-to-digital converters (ADC) made today's state-of-the art ultrasound imaging features possible, including synthetic aperture sequencing (such as dynamic transmit and receive focusing) [23], spatial compounding [24, 25], plane wave imaging [26], share wave elastography [27] and vector flow imaging [28, 29]. This section will review past and present ultrasound beamforming technologies and future potential advances thereof.

1.3.1 Review of Fixed Focus Beamforming

The earliest ultrasound systems were based on analog beamforming, applying relatively simple implementation of the beamforming function [30]. One case was a fixed focus system in both transmit and receive; therein, both transmit and receive delays are computed

for beamforming, respectively, given by,

$$\tau_{\text{Tx}} = \frac{1}{c}\sqrt{(x_{\text{Tx}_e} - x_f)^2 + z_f^2}, \tag{1.7a}$$

$$\tau_{\text{Rx}} = \frac{1}{c}\sqrt{(x_{\text{Rx}_e} - x_f)^2 + z_f^2}, \tag{1.7b}$$

where x_{Tx_e} is the lateral position for each individual transmit aperture element, x_{Rx_e} is the lateral position for each individual receive aperture element, (x_f, z_f) is the location of the fixed focus and c is the speed of sound. However, several significant limitations were immediately apparent, including higher side lobe (lower contrast) and wider main lobe (lower resolution) [31].

1.3.2 Digital Beamforming

In the early 80's, digital beamformers were commercially available, although they were not widely used until the early 90's, due to lack of ADC with a sufficient number of bits and high enough sampling rates [31]. Since state-of-art ADC, covering sufficient specification, was available in the 90's, digital beamforming enabled novel beamformation methods. Digital beamforming is widely used today and provides high quality images by improving spatial resolution (i.e., narrowing a main lobe) and reducing side lobe artifacts to increase contrast [32].

1.3.3 Software-Based Beamforming

In modern ultrasound systems, digital beamforming technique is commonly used. However, digital beamforming, which employs advanced signal processing to improve image quality, requires high computational tasks. In order to reduce the burdensome computational requirements of digital beamforming, digital signal processors (DSPs) [33] or graphics processor unit (GPU) [34] have been employed for back-end signal and image process-

ing units in modern clinical ultrasound systems. Very recently, a pixel-based beamforming was introduced, enabling the software-based image formation [35]. With a trend of using more software in ultrasound systems, software-based beamforming using multi-core DSP or GPU may be a new era of ultrasound beamforming [36, 37]. Henceforth, more novel algorithms for further improvement of image quality and new clinical applications will increase the potential of ultrasound as a critical tool in a multitude of medical applications.

1.4 Causes of Ultrasound Image Degradation Artifacts

There are many potential causes of degradation of ultrasound images, including attenuation, gross sound speed error, phase aberration and reverberation clutter [3, 38, 39, 40, 7, 41]. Recent studies indicate that both phase aberration and reverberation clutter play a major role in degrading image quality [7]. Here, potential causes or mechanisms of degraded ultrasound images are described.

1.4.1 Attenuation

Attenuation is a commonly known effect of ultrasound image degradation, caused by acoustic energy loss through absorption, and a redirection of its energy scattering due to changes in density and compressibility of the propagating medium [15]. Absorption is the process of converting absorbed energy into other energy forms, usually heat in tissue for ultrasound. On the other hand, scattering represents ultrasound wave energy redirected along the path that is different from the incident wave. Attenuation accounts for the effects of both absorption and scattering, suggesting that attenuation has thermal and frequency dependencies. Attenuation is a function of the material and image frequency, and ultimately limits the imaging depth of field.

An important aspect of frequency-dependent attenuation accounts for its effects on a broad bandwidth transmitted pulse. The center frequency (f_c) of such a pulse is downshifted as it progresses, allowing the pulse duration to be increased. The following equation

can be derived analytically [15], indicating that the center frequency is down-shifted as a function of depth, expressed as,

$$f_{c_{down}} = f_c - \frac{\alpha_0 z BW^2}{4\pi^2}, \tag{1.8}$$

where $f_{c_{down}}$ is the down-shifted center frequency, α_0 is the attenuation coefficient, z is the imaging depth and BW is the fractional bandwidth.

1.4.2 Gross Sound Speed Error

Ultrasound beamforming underlying image formation assumes speed of sound *in vivo* to be constant. The speed of sound *in vivo* is commonly assumed to be 1540 m/s in medical ultrasound imaging. However, inhomogeneous tissues have velocities ranging from 1400 m/s to 1650 m/s [38]. These gross sound speed errors significantly degrade ultrasound image quality, reducing contrast and spatial resolution [39]. Fig. 1.6 shows B-mode images, demonstrating image degradation with gross sound speed errors.

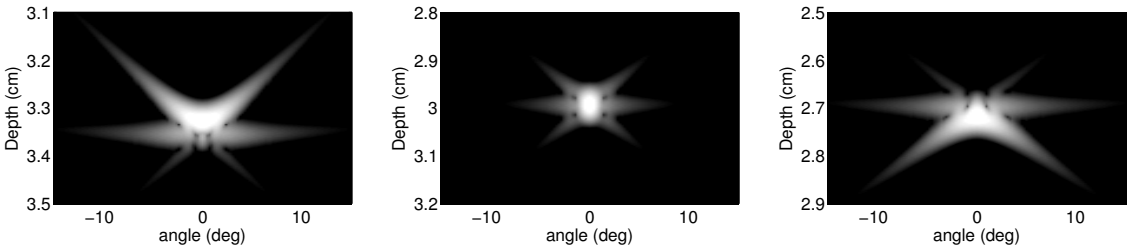

(a) -10% (b) 0% (c) 10%

Figure 1.6: B-mode images with gross sound speed error of (a) -10%, (b) 0%, and (c) +10%
.

1.4.3 Phase Aberration

Phase aberration effects are caused by sound speed inhomogeneities within tissue. The effect distorts the propagating wavefront of the signal of interest throughout inhomogeneous media. Over the past few decades, significant attention has been paid to phase aberra-

tion in order to mitigate the effect, providing many methods to correct distorted wavefronts [40, 42, 43, 44, 45, 46, 47, 48, 49]. However, there are limitations in applying on *in vivo* data, although these phase aberration correction methods show promising results in simulation. Fig. 1.7 shows the impact of aberrated wavefronts on B-mode image degradation, using resolution target simulation results.

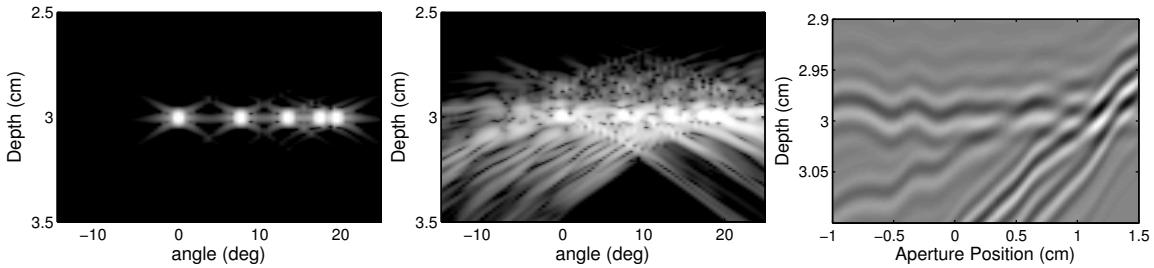

(a) (b) (c)

Figure 1.7: B-mode images of resolution target phantom (a) with unaberrated wavefronts, (b) with aberrated wavefronts. (c) An image showing aberrated wavefronts of the matched delayed channel data of (b).

1.4.4 Multipath Scattering or Reverberation

Multipath scattering is also a primary cause of degraded images, which occurs when multiple-reflected waves and the waves scattering from the region of interest (ROI) arrive at the transducer aperture simultaneously [50]. Reverberation is also multiple reflections generated by a layered, inhomogeneous medium, as illustrated in Fig. 1.8 [2]. Therefore, both multipath scattering and reverberation are an identical phenomenon. Both generate clutter that distorts the appearance of the wavefronts from the region of interest, resulting in image degradation. Fig. 1.9 illustrates that many wavefronts from multipath scattering signals interfere with one another, which generates clutter.

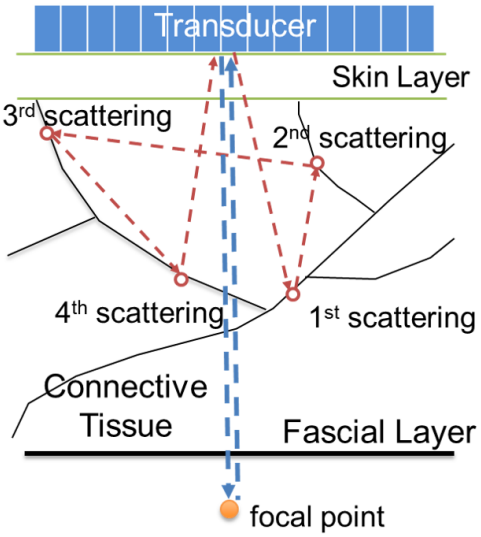

Figure 1.8: Mechanism of multipath scattering and reverberation within tissue [2]. The dotted blue line shows an ideal signal scattering from a focal point (i.e,, region of interest), while the dotted-red line represents multipath scattering signal that returns to the transducer at the same time when the signal of interest arrives to the transducer aperture.

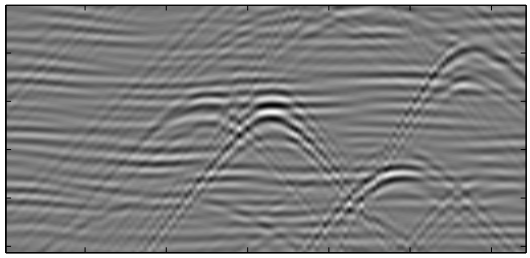

Figure 1.9: An example of cluttered channel data, showing many multipath scattering signals propagating toward a transducer.

1.5 Potential Acoustic Clutter Suppression Algorithms

To date, numerous algorithms for suppressing clutter have been developed, introduced and evaluated, in an attempt to identify the cause of image degradation and improve image quality *in vivo*. In this section, potential clutter suppression algorithms developed by others are reviewed.

1.5.1 Tissue Harmonic Imaging

Tissue harmonic imaging is the most commonly used method and has been successfully translated in diagnostic ultrasound imaging in practice, since it was introduced by Christopher *et al.* in 1997 [51, 52, 53]. Basic principles of tissue harmonic imaging (THI) are to utilize non-linearity of sound propagation in tissue, by receiving reflected signals from tissue at a second harmonic frequency. The second harmonic frequency (f_{hc}) is twice as high as the transmitted frequency (f_c), which is referred to as a fundamental frequency, that is used for fundamental B-mode image (i.e., $f_{hc} = 2f_c$). The received signals at harmonic frequency, which are not contributed by any signals within the transmitted frequency band, are used for a B-mode image reconstruction. Because of the fact that aberrated wavefronts and reverberation cluttered signals are predominant at the fundamental frequency, harmonic B-mode image shows a significant improvement in image quality by suppressing clutter, resulting in higher contrast, better resolution, and near-field artifact reduction. Fig. 1.10 depicts an area of higher order frequencies generation, suggesting that harmonic frequencies are developed around the region of the beam focus and deeper depth, but are not fully developed in the near field [54, 55, 56]. However, some weaknesses of using tissue harmonic images are identified, including higher attenuation of the higher frequency harmonic components due to frequency-dependency attenuation, lower amplitudes of harmonic signals than those of the fundamental frequency waves, resulting that the second harmonic is typically 10 dB below the fundamental when comparing the total power, and a loss in axial

resolution because of the narrowed bandwidth [15, 57].

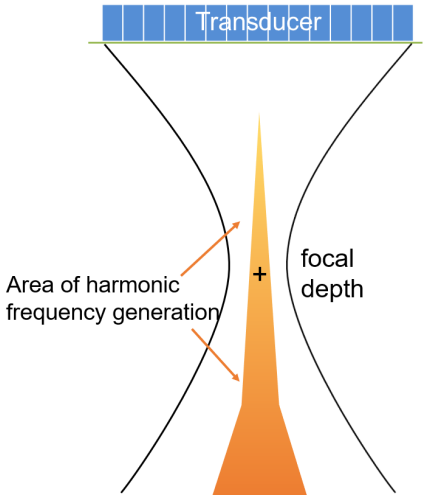

Figure 1.10: Area of higher order harmonic frequencies generation [3]. The figure suggests that harmonic frequencies may not be fully developed in near field.

1.5.2 Time-Reversal Technique

Time-reversal is also a useful technique to suppress reverberation clutter. In time-reversal acoustics, a signal is recorded by an array transducer, time-reversed and then re-transmitted into the medium [58]. The first successful time-reversal experiment was performed by Fink *et al.* The re-transmitted signals propagate back throughout the same medium and refocus on the original source. In other words, the time-reversed signals propagate backwards through the medium and go through all the multipath scattering [59]. As a result, these processes suppress multipath clutter. However, the time-reversal technique requires a point-like source located in a medium due to the limitation of the difficulty of detecting the focal region by a set of transducers [58].

1.5.3 Second-Order Ultrasound Field

Another promising clutter suppression imaging modality is second-order ultrasound field (SURF), which was initially developed by Angelsen *et al.* [60, 61, 62, 63, 64, 65].

With this method, two transmitted pulses containing a low frequency (ranging from 0.2 to 1.2 MHz) and a high frequency (from 1.0 to 10 MHz) are used [62]. The low frequency pulse manipulates the material of medium (i.e., tissues) where the signals are propagating (called manipulation pulse), while the high frequency pulse is a signal used for imaging (called imaging pulse). One imaging pulse is positioned on a peak of the manipulate pulse and the other imaging pulse is on the bottom. The propagation speed of an imaging pulse is modified by a manipulation pulse. The co-propagating imaging pulses become distorted when the manipulation pulse shows non-linear effects. Due to the distortion of the manipulation pulse, a delay between the two imaging pulses is measured with depth. The imaging pulse, therefore, possesses information about the depth of the first scattering that occurred. Based on the information, the imaging pulse then masks multipath scattering, resulting in clutter suppression. The key concept of SURF is to utilize a dual-frequency band technique in which a conventional imaging pulse is manipulated by a lower frequency pulse [65]. SURF imaging shows potential to suppress reverberation clutter components. A possible problem with SURF imaging may be the existence of grating lobes produced when transmitting high frequency pulses. It may also require complex hardware and transducers because of the complicated pulse sequencing.

1.5.4 Short-Lag Spatial Coherence

Recently, Lediju *et al.* introduced a novel clutter suppression algorithm, called short-lag spatial coherence (SLSC) imaging [66]. The approach of SLSC does not apply a conventional delay-and-sum (DAS), but measures the spatial coherence of received echoes to form ultrasound images. The idea of SLSC originated in the van Citter-Zernike theorem, which discussed the applicability of pulse echo measurement by Mallert and Fink [67]. The van Citter-Zernike theorem predicts the spatial coherence of backscattered signals in aperture domain, where the backscattered signals are recorded by individual aperture elements. For instance, the normalized spatial coherence as a function of the lateral lag or distance, l, can

be formulated by

$$\hat{R}(l) = \frac{1}{M-l} \sum_{i=1}^{M-l} \frac{\sum_{k=k_1}^{k_2} s_i(k) s_{i+l}(k)}{\sqrt{\sum_{k=k_1}^{k_2} s_i^2(k) \sum_{k=k_1}^{k_2} s_{i+l}^2(k)}}, \tag{1.9}$$

where $\hat{R}(l)$ is the normalized spatial coherence function, M is the total number of channel elements, the aperture domain signal received by the ith element is denoted by $s_i(k)$, k is the discrete depth or time index, $k_2 - k_1$ is a correlation kernel size of one wavelength. The SLSC beamforming is integration of the spatial coherence function up to the first L lags in (1.9) [68, 66].

$$RF_{SLSC}(k) = \sum_{l=1}^{L} \hat{R}(l). \tag{1.10}$$

SLSC beamforming forms the spatial coherence-based images (not B-mode images) at each depth k of each A-line. For SLSC imaging, L is typically the number of elements corresponding to 1-30% of the transmit aperture [68].

1.6 Aperture Domain Model Image Reconstruction

Byram *et al.* introduced an aperture domain model-based beamforming algorithm that suppresses reverberation clutter and off-axis scattering while preserving signals of interest [69, 70, 41, 50]. This algorithm is called aperture domain model image reconstruction (ADMIRE). An overview of ADMIRE is shown in Fig. 1.11.

In principle, because ADMIRE preserves RF channel data after decluttering, ADMIRE can be combined with other methods, including synthetic aperture techniques [71, 72, 73, 74, 75, 76, 77, 78] and adaptively weighted methods [79, 80, 81, 82, 83, 84], for further improvement in ultrasound image quality. Fig. 1.12 demonstrates an example of combining ADMIRE with minimum variance (MV) beamforming [83, 84] using experimental resolution phantom data. The result (i.e., lateral beam width at -6 dB) obtained from using ADMIRE, followed by MV beamforming, shows some improvements in image quality

when compared to the image and lateral beam profile formed by using ADMIRE alone.

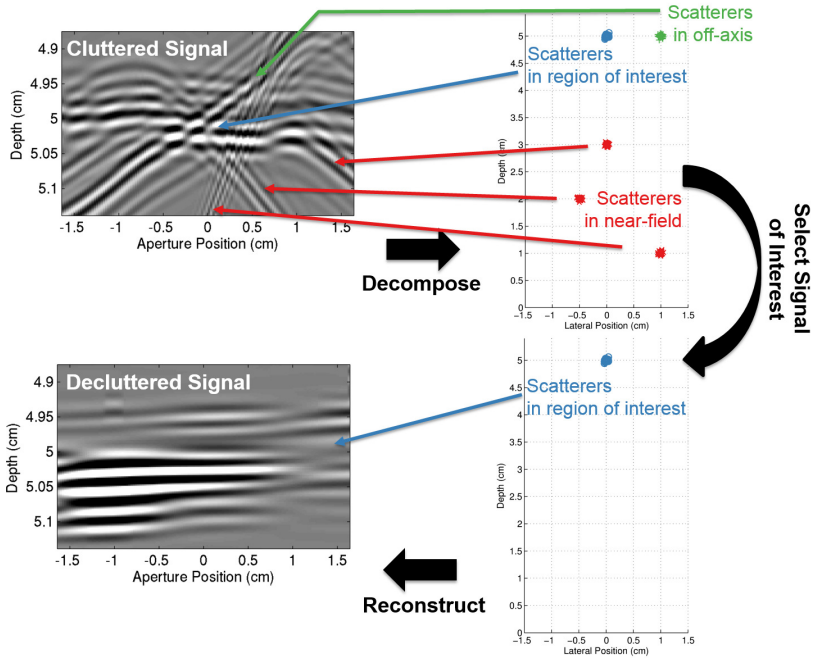

Figure 1.11: Overview of ADMIRE is shown. The cluttered signal (upper left figure) contains signals scattering from the region of interest (blue arrow) and signals scattering from clutter (green and red arrows). After decomposition, ADMIRE identifies and decomposes scattering signal components from the ROI and scattering signals from clutter (upper right figure), and then selects only signals of interest (lower right figure). ADMIRE then reconstructs the decluttered signal (lower left figure).

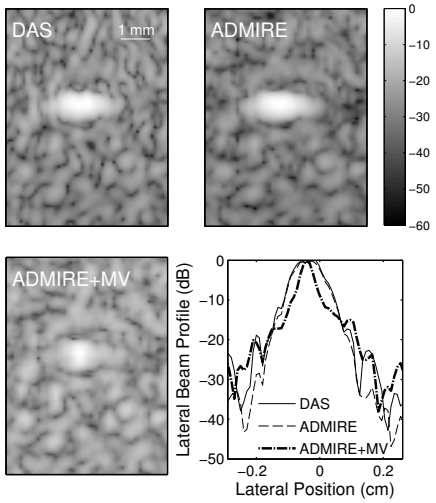

Figure 1.12: An example applying the combination of ADMIRE and minimum variance (MV) beamforming. The imaging data is acquired from an experimental tissue-mimicking (TM) phantom.

A major aim of this dissertation is not only to investigate the model-based beamforming algorithm's ability but to also identify its limitations in suppressing ultrasound acoustic clutter sources, including reverberation, off-axis scattering, wavefront aberration and gross sound speed mismatch. These sources of clutter produce image artifacts, degrading ultrasound images. Based on the findings in the dissertation works, the proposed solutions to address the identified limitations are also reported. The dissertation is organized as follows.

Chapter 2 describes the ADMIRE algorithm and demonstrates preliminary studies to validate the accuracy of the ADMIRE model using simulation data. Model predictor error and model predictors' correlation characteristics are assessed.

Chapter 3 evaluates the ADMIRE algorithm's robustness in the presence of off-axis clutter and sound speed mismatch using simulation performed with Field II and experimental measurements from phantoms and *in vivo* data.

Chapter 4 studies the impact of ADMIRE performance to suppress acoustic clutter in the presence of phase aberration and reverberation. In order to accurately characterize aberrated signals of interest, an adaptive component is introduced to the ADMIRE model to account for wavefront aberration.

Chapter 5 extends ADMIRE evaluation from conventionally focused beam sequences to plane wave transmit sequencing, in conjunction with synthetic aperture focusing (SAF), to insonify a broad field of view. Additionally, this chapter investigates how robustly ADMIRE performs in the presence of random white noise.

Chapter 6 addresses more computationally-efficient methods to implement ADMIRE with otherwise similar performance because ADMIRE is computationally expensive and its lengthy run-time impairs its usefulness. In this study, three different reduced model methods and other strategies to reduce complexity are evaluated.

Chapter 7 proposes contrast ratio dynamic range as a new quality metric. The proposed metric is applied to several beamformers, including DAS, two adaptively weighted beamforming methods, called coherence factor (CF) and minimum variance (MV), SLSC

and ADMIRE. ADMIRE is implemented with different sets of regularization parameters to suggest how the anechoic cyst case can be gamed with regularized methods.

Chapter 8 assesses whether model-based beamforming method or ADMIRE can be an effective tool to provide high quality images in real clinical applications. In this chapter, tissue boundary delineation is assessed using fundamental and harmonic ADMIRE and SLSC for percutaneous biopsy guidance application.

Chapter 9 summarizes this dissertation as to model-based beamforming's ability and its identified limitations. Future work is also proposed.

Chapter 2

DESCRIPTION OF ADMIRE AND PRELIMINARY STUDIES OF MODEL-BASED BEAMFORMING

Portions of this work were published in [69]:

B. Byram, K. Dei, J. Tierney, and D. Dumont, "A Model and Regularization Scheme for Ultrasonic Beamforming Clutter Reduction," *IEEE Transaction on Ultrasonics, Ferroelectrics, and Frequency Controls*, vol. 62, no. 11, pp. 1913-1927, 2015.

2.1 Overview

This chapter describes the ADMIRE algorithm laid out by *Byram et al.* to identify and suppress clutter from off-axis and multipath sources, followed by preliminary studies conducted for validating the model used for ADMIRE. In the studies, we validated the accuracy of the ADMIRE model using Field II simulation data [18, 17]. We also assessed correlation characteristics of ADMIRE model predictors. In this chapter, the ADMIRE model is referred to as a new model [69], while the old model is the previous generation of an ADMIRE like approach that is a linear frequency-modulated sinusoid model, also called a chirp model [41].

2.2 ADMIRE Algorithm

The ADMIRE algorithm models the received wavefronts at the surface of the transducer aperture, which we call the aperture domain. The ADMIRE model accounts for the spherical wavefronts, short-time Fourier Transform (STFT), pulse-bandwidth correction and angular sensitivity, leading to a non-stationary, sinusoidal model [69]. The signal received at the aperture can be analytically expressed in the following form.

$$p_s(x;t,\omega) = \sum_{n=0}^{N-1} A_n(x) e^{j\omega\tau(x;x_n,z_n,\tau_n)}, \tag{2.1}$$

where x is the transducer aperture location, t and ω are the time and frequency to localize the signal, $\tau(x;x_n,z_n,\tau_n)$ is the wavefront delay for a received signal reflecting from point (x_n,z_n) at time τ_n, and N is the number of scatterers arriving at time t. $A_n(x)$ is the amplitude modulation term across the transducer aperture induced by a combination of short-time Fourier Transform (STFT) windowing and element sensitivity (ES),

$$A_n(x) = A_{STFT}(x) A_{ES}(x). \tag{2.2}$$

The first-term of (2.2) is

$$A^2_{STFT}(x) = \int_{t_c-\frac{\Delta t}{2}}^{t_c+\frac{\Delta t}{2}} w^2_{STFT}(t-t_c) w^2_{env}(t-\tau(x;x_n,z_n,\tau_n))\, dt, \tag{2.3}$$

where Δt is the STFT window size, t_c is the middle of the STFT window, w_{STFT} is the window assigned for the STFT, and w_{env} is the axial pulse envelope function. The second-term of (2.2) is addressed by Selfridge *et al.* [85], given by,

$$A_{ES}(x) = \frac{\sin(\frac{\pi w \sin(\theta)}{\lambda})}{\frac{\pi w \sin(\theta)}{\lambda}} \cos(\theta) \tag{2.4}$$

where $\theta = tan^{-1}(\frac{x-x_n}{z_n})$.

In the first step of implementing ADMIRE, dynamic receive delays are applied to RF channel data. The delayed channel data are then short-time Fourier Transformed (STFT). Next, model-fitting is performed on a single frequency component of the post-STFT channel signals at a given depth. The model relating to the response of y can be written in the following form [69],

$$y = X\beta, \tag{2.5}$$

where X is the ADMIRE model matrix with the specific model space sampling for that depth and frequency and β is the model coefficient vector. X and y are then expressed with the following matrices, respectively,

$$X = \begin{bmatrix} \Re\{p_{s_n}(x;t,\omega)\}^\top & -\Im\{p_{s_n}(x;t,\omega)\}^\top \\ \Im\{p_{s_n}(x;t,\omega)\}^\top & \Re\{p_{s_n}(x;t,\omega)\}^\top \end{bmatrix}, \tag{2.6}$$

$$y = [\Re\{S_i(mT,\omega_p)\}\ \Im\{S_i(mT,\omega_p)\}]^\top, \tag{2.7}$$

where $\Re$ and $\Im$ denote the real and imaginary components, respectively, mT is the discrete time index, T is the sampling period of the RF data, ω_p is a discrete frequency, $S_i(mT,\omega_p)$ is the post-STFT signal for a single channel of the aperture, i indexes channel, and $\top$ is the matrix transpose.

The goal of ADMIRE is to take the pressure, $p_s(x;t,\omega)$ measured by the aperture elements and solve for the right side of (2.1). Unfortunately, the problem is ill-posed. Therefore, the model decomposition is performed using elastic-net regularization [86],

$$\hat{\beta} = \arg\min_{\beta}(\|y - X\beta\|^2 + \lambda(\alpha\|\beta\|_1 + (1-\alpha)\|\beta\|_2^2/2)), \tag{2.8}$$

where $\|\beta\|_1$ and $\|\beta\|_2$ denote the L1-norm and the L2-norm, respectively, and α and λ are the parameters used for adjusting the regularization. The parameter of α ranges between 0 and 1 to determine the relative weight of L1 and L2. For an elastic-net regularization solution, the degrees of freedom (DOF) is a function of λ [87] and given by

$$DOF(\lambda) = tr[X_A(X_A^\top X_A + \lambda I)^{-1}X_A^\top], \tag{2.9}$$

where X_A is the active set of the model predictors with non-zero coefficients after model-fitting with a given λ. (Chapter 4 will show that the degrees of freedom play an important role when model mismatch from aberration is present.)

After the model-fit, model predictors within the acceptance region are used to reconstruct decluttered signals. The acceptance zone can be formulated as an ellipse, depending on the lateral and axial resolutions of res_{lat} and res_{axl}, respectively,

$$\left(\frac{x_n - x_r}{c_{lat} res_{lat}}\right)^2 + \left(\frac{z_n - z_r}{c_{axl} res_{axl}}\right)^2 \leq 1, \tag{2.10}$$

where x_r and z_r indicate the center of the acceptance zone, and c_{lat} and c_{axl} are scalable factors to adjust the acceptance region. In this study, res_{lat} is computed by $res_{lat} \approx \lambda_w z \mathcal{F}\{|p_s(x; x_r, z_r, 0)|\}_{BW}$ while the axial sampling is approximated by $res_{axl} \approx 2res_{lat}$, where λ_w is the wavelength, z is the axial depth, $F\{|\cdot|\}_{BW}$ denotes the lateral bandwidth of the model predictor [69, 88]. The signal of interest is reconstructed using

$$y_{ROI} = X_{ROI}\hat{\beta}_{ROI}, \tag{2.11}$$

where y_{ROI} is a decluttered signal, X_{ROI} is the model predictors that are spatially within the acceptance zone, and $\hat{\beta}_{ROI}$ is the corresponding model coefficients. The decluttered signals are then converted into the original time-domain RF channel signals applying the inverse short-time Fourier Transform (ISTFT) [89]. Table 2.1 shows ADMIRE parameters used unless otherwise specified.

Table 2.1: ADMIRE Parameters

Parameter	Value
α	0.9
λ	0.0189 $\sqrt{y^\top y}$
c_{lat}	6
c_{axl}	2
Model space (lateral) [m]	aperture length
Model space (axial) [m]	$\{0.001,\ z_r + (c_{axl} res_{axl})/2\}$
Model sampling (inside) [m]	$\{0.0716 res_{lat},\ 0.286 res_{axl}\}$
Model sampling (outside) [m]	$\{1.43 res_{lat},\ 1.43 res_{axl}\}$
STFT window size	(8log(2))/(2πBWf_0)

($\top$ is the matrix transpose, BW is the fractional bandwidth and f_0 is the center frequency of transmitted pulse.)

2.3 ADMIRE Model Evaluation

For the model assessment, we accounted for wavefront origin, dynamic receive focusing, phase delay time, lateral angular sensitivity and pulse width. Multipath scattering was simulated using a pseudo non-linear tool [4]. We then demonstrated the ability to accurately model individual aperture domain signals from a given origin. Figs 2.1 and 2.2 illustrate examples of wavefronts resulting from multipath scattering, and compared the old and new models against simulated data. The wavefront within the STFT window is sampled for model-fit (i.e., model decomposition). In comparison with the old model [41], the new model is more accurate.

We also quantitatively evaluated a set of model predictor errors with and without an intentional modulation corresponding to γ = 0.75, for the old and new models of ADMIRE. The scaling factor γ was introduced in conjunction with a method for intentionally modulating aperture domain signals, which scales the depth dimension used for calculating the dynamic receive delay, expressed as [69],

$$\tau_{DR_\gamma}(x; x_f, z_f) = \frac{1}{c}\sqrt{(x - x_f)^2 + ((1+\gamma)z_f)^2} + \frac{(1-\gamma)z_f}{c}, \tag{2.12}$$

where τ_{DR_γ} is the intentionally modulated dynamic receive delay, x is the aperture location, (x_f, z_f) are the dynamic receive focal positions, and c is the speed of sound.

Fig. 2.3 presents the model predictor error. The new model has significantly lower model error compared with the old model. Furthermore, when using the intentional modulation method, the region of lowest model error is shifted toward the ROI. These findings also indicate that higher error occurs in the near-field for all model predictors, which may be a limitation of the Field II simulations. Note that ADMIRE uses delayed channel signals without the scaling factor γ unless otherwise specified.

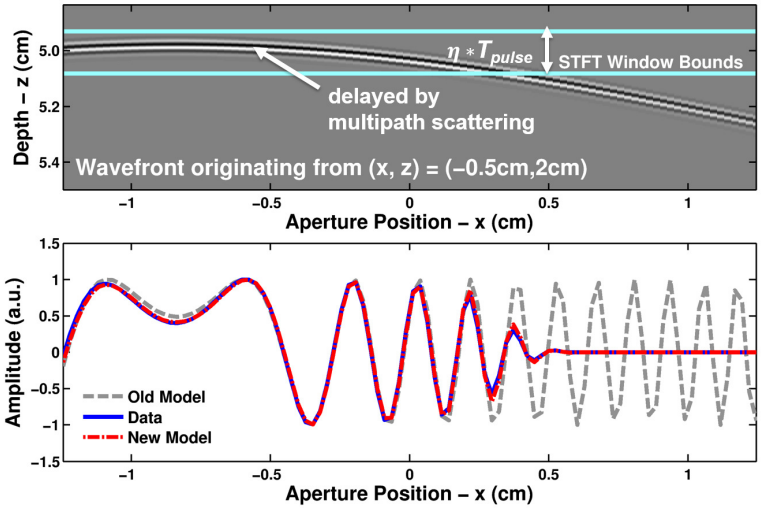

Figure 2.1: Top figure illustrates an example wavefront delayed by multipath scattering. The wavefront originates from 0.5 cm off-axis and 2 cm depth. The receive focus is set at 5 cm depth. The bottom figure shows the post-STFT signal at the center frequency of 3 MHz against the old and new modeled signals.

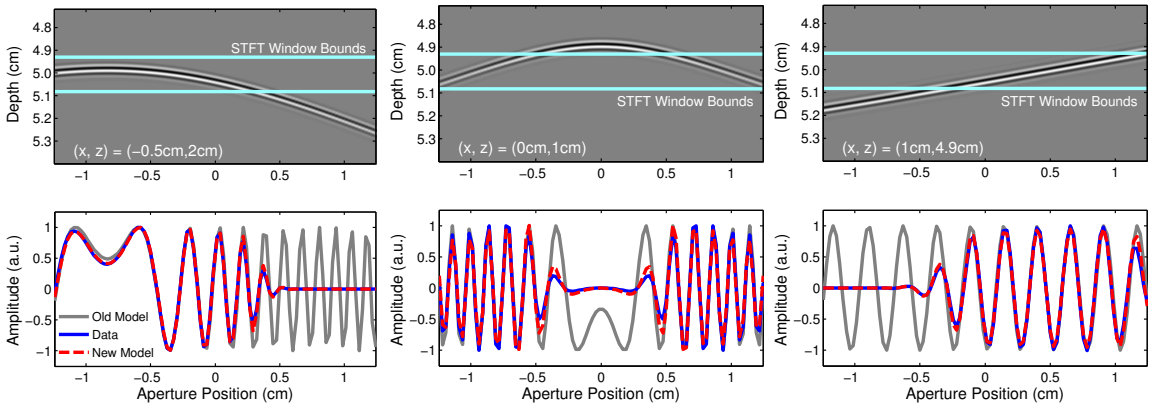

(a) (b) (c)

Figure 2.2: Three additional examples of the time-domain channel data (top figures) and the corresponding aperture post-STFT data (bottom figures) are presented. The examples show the wavefront with several cases of source location (x_n, z_n) and phase delay time (τ_n) after dynamic receive focusing for a region of interest at 5 cm. The post-STFT data against the old and new modeled signals for each case is compared.

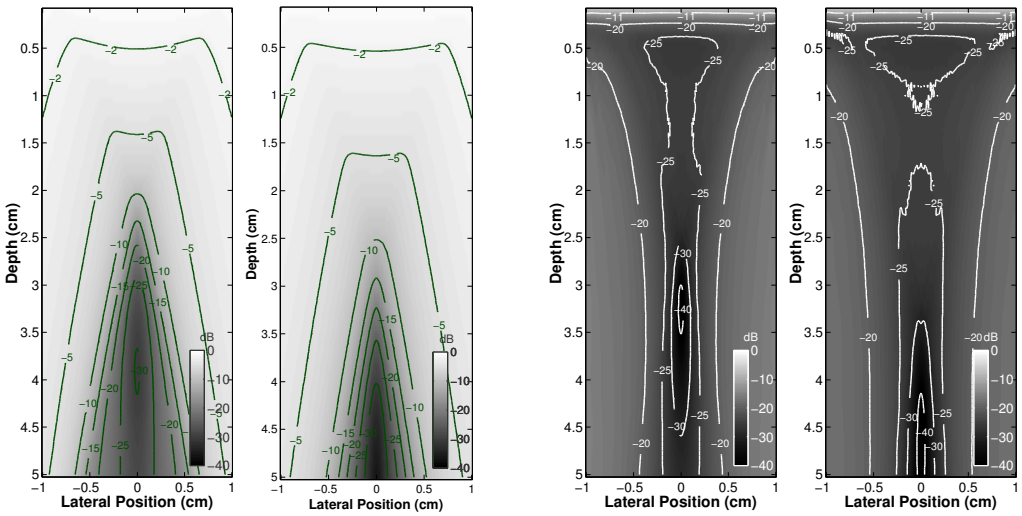

(a) old ($\gamma = 0$) (b) old ($\gamma = .75$) (c) new ($\gamma = 0$) (d) new ($\gamma = .75$)

Figure 2.3: (a) and (b) show the old model error power as a function of spatial coordinates to matched Field-II simulations, while (c) and (d) are the new model error power. Another set of figures is (a) and (c) without intentional modulation, (b) and (d) with an intentional modulation corresponding to γ = 0.75.

2.4 ADMIRE Model Predictors Analysis

We measured the normalized cross correlation (NCC) of ADMIRE model predictors at a specific location, compared to other predictors in the model space. Fig. 2.4 shows the NCC value of ADMIRE model predictors at (a) the focus of 5.0 cm depth on axis and (b) (-0.5 cm, 1.0 cm) in the lateral and axial dimensions, respectively. The correlation in the lateral direction is significantly lower than that in the axial direction. The results are consistent with the ADMIRE model matrix, which is oversampled and predictors are not fully orthogonal.

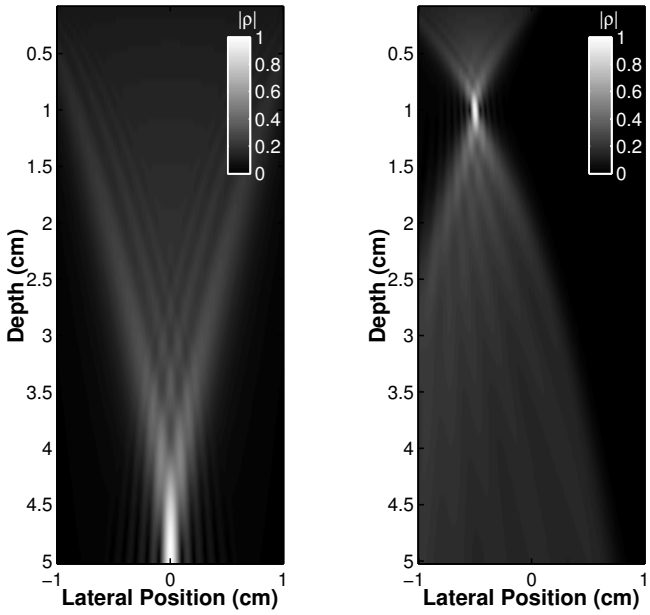

(a) (b)

Figure 2.4: (a) and (b) show the normalized cross-correlation (NCC) of ADMIRE model predictors at the focus of (0, 5.0) cm and at (-0.5, 1.0) cm in the lateral and axial dimensions, respectively. The model predictors are not orthogonality relation, which matches the physics of multipath clutter.

Chapter 3

MODEL-BASED ULTRASOUND BEAMFORMING IN THE PRESENCE OF OFF-AXIS CLUTTER AND SOUND SPEED VARIATION

This work was originally published in [90]:
K. Dei and B. Byram, "A Robust Method for Ultrasound Beamforming in the Presence of Off-Axis Clutter and Sound Speed Variation," *Ultrasonics*, vol. 89, pp. 34-45 2018.

3.1 Introduction

Ultrasound is one of the most widely used imaging modalities in medicine and has been used extensively for diagnosis and therapy due to its real-time, inexpensive and non-invasive features [5]. Ultrasound suffers from many artifacts, which impair image quality and limit its effectiveness [91, 15, 38, 39, 40, 7, 41]. These artifacts degrade the resolution and contrast of an ultrasound image, and subsequently reduce the usefulness of ultrasound in diagnosis and therapeutic guidance [3].

It is well-established that lower point spread function side-lobes are correlated with higher contrast and that narrower main-lobe width provides better spatial resolution. Conventional beamforming, often referred to as delay-and-sum (DAS), in conjunction with a deterministic apodization scheme, such as Hamming, Hann or Gaussian window function, can improve contrast by suppressing side-lobes but at the cost of broadening the main-lobe, which degrades spatial resolution. Alternatively, DAS with rectangular apodization yields better resolution but lower contrast because of higher side-lobes.

In order to address the trade-off encountered with traditional apodization methods, many adaptive beamforming algorithms have been developed and evaluated, including coherence-based adaptive weighting [79, 80, 81, 82], minimum variance beamforming [92, 93, 83, 94, 84], dual apodization using cross-correlation [95, 71, 72], non-linear apodization

techniques such as dual-/tri-apodization with chosen window functions [96], apodization profiling methods using constrained least squares [97, 98] and the second-order-cone optimization [99]. A side-lobe filtering method has also been reported to have had substantial effects on ultrasound image quality [100].

Among those methods, a model-based beamforming algorithm has been also introduced by our group, as described in the preceding chapter. [41, 50, 70, 69, 101]. The algorithm uses a model of received wavefronts on aperture domain signals reflected from scatterers located in the imaging field of interest. The model enables the algorithm to identify scatterer locations and suppress clutter, particularly, off-axis scattering and reverberation artifacts. We refer to the algorithm as aperture domain model image reconstruction (ADMIRE). ADMIRE decomposes the aperture domain signals into clutter and signal of interest components. The clutter component is removed, leaving decluttered channel data behind. While ADMIRE has been shown to suppress reverberation artifacts [69, 102], the primary objective here is to demonstrate whether ADMIRE suppresses off-axis clutter without sacrificing the resolution obtained from an unapodized beam. In this study, the model space is specifically restricted to only depths around the region of interest so that the algorithm primarily accounts for off-axis clutter. Because ADMIRE preserves decluttered channel data, we can also combine ADMIRE with other methods to investigate whether additional post processing techniques further improve image quality. There are many potential algorithms that may enable post-ADMIRE decluttered signals to achieve further off-axis suppression and improve image quality. In this study, we used a coherence factor (CF) weighting technique, which was originally introduced by Mallart and Fink [79], also formalized as a metric by Hollman *et al.* [80]. The coherence factor is useful to weight delayed channel data (i.e., aperture domain signals) without introducing a high computational complexity.

To further evaluate the ADMIRE algorithm, we investigated whether ADMIRE, a model-based beamformer, is robust to model-mismatch caused by deviations in gross sound speed. Clinical ultrasound image formation typically assumes a constant speed of sound of 1540

m/s. However, *in vivo* sound speed is not constant and tissues have velocities ranging from 1400 m/s to 1650 m/s that cause variation in the overall effective sound speed [38]. These gross sound speed deviations degrade image quality by reducing contrast and spatial resolution [39].

In this chapter, we evaluate the algorithm's robustness in the presence of off-axis clutter using simulations performed with Field II and experimental measurements from phantoms and *in vivo data* acquired using an ultrasound imaging system. In simulations, we tested the performance of ADMIRE, ADMIRE plus CF weighting, compared to DAS with and without CF, using point spread functions and resolution target phantoms. We also captured experimental data from a wire phantom, a tissue-mimicking phantom and a human subject liver. In evaluating ADMIRE, we also identified some limitations and demonstrate solutions. Finally, we show the impact of ADMIRE in the presence of sound speed variation from two target simulation cases—1) resolution target and 2) contrast target. In resolution target simulations, we measured the lateral full-width at half-maximum (FWHM) of the main-lobe with respect to a ratio of gross sound speed errors, while image quality metrics (i.e., contrast and contrast-to-noise ratio) and speckle statistics (i.e., speckle signal-to-noise ratio) were used in the case of contrast target simulations.

3.2 Methods

3.2.1 ADMIRE Model Space and Parameters

Fig. 3.1 shows an ADMIRE model matrix and the corresponding model space. As described in the figure, the ADMIRE model space has two subspaces: 1) region of interest (ROI) subspace and 2) clutter subspace. In this study, the model space is specifically restricted to only depths around the region of interest so that the algorithm primarily accounts for off-axis clutter. Table 3.1 shows the parameters used unless otherwise specified.

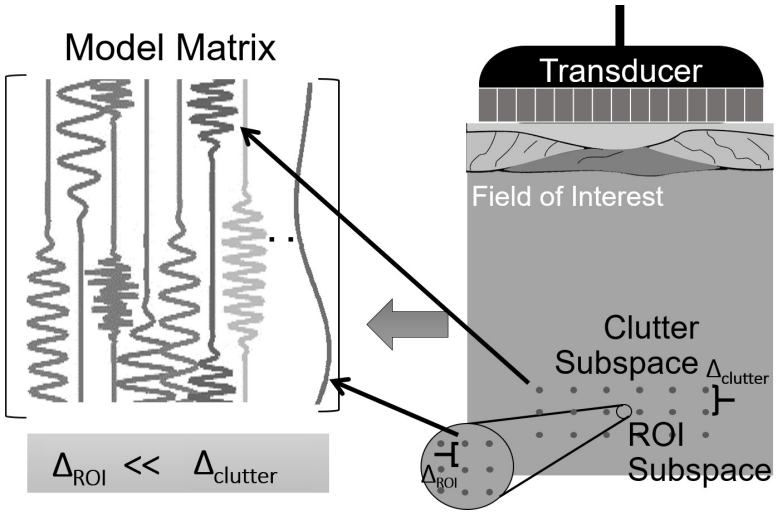

Figure 3.1: ADMIRE matrix of model predictors with the specific model space sampling. The ADMIRE model space has two subspaces: 1) region of interest (ROI) subspace and 2) clutter subspace. The ADMIRE model space is finely sampled in the ROI subspace and coarsely sampled in the clutter subspace. In this study, the model space is specifically restricted to only depths around the region of interest so that the algorithm primarily accounts for off-axis clutter.

Table 3.1: ADMIRE Parameters

Parameter	Value
α	0.9
λ	0.0189 $\sqrt{y^\top y}$
c_{lat}	4
c_{axl}	2
Model space (lateral)	aperture width
Model space (axial)	$z_r \pm (c_{axl} res_{axl})/2$
Model sampling (ROI)	$\{0.0716 res_{lat},\ 0.286 res_{axl}\}$
Model sampling (clutter)	$\{1.43 res_{lat},\ 1.43 res_{axl}\}$
STFT window size	(8log(2))/(2πBWf_c)

$\top$ is the matrix transpose,
BW is the fractional bandwidth and
f_c is the center frequency of transmitted pulse.

Note that the selection of these regularized parameters was determined by simulations findings from a previous study [69].

3.2.2 Coherence Factor

As an additional comparison, we consider the coherence factor on its own and as an additional post-processing after ADMIRE. To further improve image quality, post-ADMIRE decluttered channel data can be combined with other beamforming techniques, including traditional linear apodization methods, minimum variance (MV) beamforming [83, 84] or other advanced beamforming methods. Here, we consider an adaptive weighting approach based on the coherence factor (CF). The coherence factor (CF) is computed using delayed channel signals (i.e., aperture domain signals), defined as [81]

$$CF(k) = \frac{\left|\sum_{m=1}^{M} s(m,k)\right|^2}{M\sum_{m=1}^{M}|s(m,k)|^2}, \tag{3.1}$$

where k is the discrete time index, m indexes aperture element, $s(m,k)$ is the delayed channel signal of element m, and M is the total number of receive aperture elements [79, 80, 81]. We apply CF weighting to beamformed radio-frequency (RF) signals obtained from DAS and ADMIRE, as a post-processing technique.

3.2.3 Simulations

We simulated a point target to demonstrate resolution performance and basic side-lobe suppression performance. We used Field II [17, 18] to conduct the simulations using the parameters indicated in Table 3.2. We modeled a phase array transducer with 3.0 MHz center frequency and 60% fractional bandwidth. We compared point spread functions derived from DAS and ADMIRE beamforming. We also combined DAS and ADMIRE with CF weighting. The resulting point spread functions demonstrate spatial resolution and off-axis energy suppression of each beamforming approach. We then quantified the spatial resolution laterally and axially (i.e., the full-width at half-maximum (FWHM) of the lateral and axial beam profiles).

We also simulated a resolution target phantom—meaning several adjacent point targets—

Table 3.2: Field II Simulation Parameters

Parameter	Value
Number of aperture elements	128
Number of mathematical elements elevationally	11
Number of mathematical elements laterally	7
Height of element	8 mm
Width of element	0.254 mm
Kerf	0.003 mm
Lateral pitch	0.257 mm
Center frequency (f_c)	3 MHz
Sampling frequency (simulation)	120 MHz
Sampling frequency (downsampled)	40 MHz
Bandwidth	60%
Transmit focal depth	3 cm
Transmit/Receive f/#	2.0

using Field II to further evaluate the various algorithms. The simulated resolution phantom mimics a wire phantom image, which is composed of five point targets. We applied the same parameters, as indicated in Table 3.2. The resulting images of the resolution phantom were reconstructed using DAS and ADMIRE, along with CF weighting, denoted as DAS+CF and ADMIRE+CF.

Using the Field II, we continued to simulate a uniform, fully developed speckle background with a density of 25 scatterers per resolution cell [103], in the presence of a single strong scatterer. The Field II parameter settings were the same as indicated in Table 3.2. The single strong scatterer's amplitude was scaled, relative to the background scatterers. We generated imaging data ranging from a single scatterer-to-background speckle ratio (SBR) of 20 dB to 80 dB, given by

$$SBR = 10 \log 10 \left(\frac{\mathrm{P}_{\mathrm{Scatterer}}}{\overline{\mathrm{P}}_{\mathrm{Bkg}}} \right). \tag{3.2}$$

where $\mathrm{P}_{\mathrm{Scatterer}}$ and $\overline{\mathrm{P}}_{\mathrm{Bkg}}$ denote the power of the single scatterer and the average power of background speckle signal, respectively. We then applied DAS, DAS+CF, ADMIRE and ADMIRE+CF, respectively. The resulting images from applying ADMIRE, ADMIRE+CF

include two cases using different values of λ: one is $0.0189\sqrt{y^\top y}$, indicated in Table 3.1, while the other has $0.00189\sqrt{y^\top y}$. Lower values of λ increase degrees of freedom [87]. The degrees of freedom in the first case are in a range between 50 and 70 (i.e., low *df*), while those of the second case are nearly equal to the maximum allowable degrees of freedom (i.e., high *df*). We then evaluated ADMIRE performance.

Finally, we investigated the robustness of the methods in the presence of sound speed inhomogeneities using simulated data. We modeled a phased array transducer with 3.5 MHz center frequency and 60% fractional bandwidth, similar to the point spread function simulation setting summarized in Table 3.2. We used Field II to simulate the received pulse echo signals. The focal depth of the transmit beam was specified at 3 cm, with an f/1.5 system on both transmit and receive beams. The simulated phantoms were a resolution target and a contrast target. The resolution target phantom has a point target placed at 3 cm, while the contrast phantom is an anechoic cyst of a 5 mm diameter circle 3 cm deep in fully developed speckle background. The sound speeds used in the simulation were across a range of 10% above and below the assumed sound speed (i.e., 1540 m/s). We always applied beamforming delays assuming the sound speed was 1540 m/s.

We computed metrics of resolution and contrast as a function of sound speed mismatch. The spatial resolution was quantified by measuring lateral FWHM length in resolution target phantoms, while we computed contrast and contrast-to-noise ratio (CNR) using contrast target phantoms. The contrast and CNR metrics are defined by

$$C = -20\log 10(\frac{\mu_L}{\mu_B}), \tag{3.3}$$

$$CNR = 20\log 10(\frac{|\mu_L - \mu_B|}{\sqrt{\sigma_L^2 + \sigma_B^2}}), \tag{3.4}$$

where (μ_L, σ_L^2) and (μ_B, σ_B^2) denote the value of (mean, variance) of the enveloped but uncompressed image inside (i.e., lesion) and outside (i.e., background) the anechoic struc-

tures, respectively. Along with contrast and CNR, we also measured speckle statistics using

$$SNR_{\text{speckle}} = \frac{\mu_B}{\sigma_B}. \tag{3.5}$$

There are 6 independent speckle realizations generated for the contrast target simulation. We applied image quality metrics to data after DAS and ADMIRE with and without CF weighting.

3.2.4 Experimental Phantom Data

To reinforce the simulation results, we evaluated the methods using experimental data obtained from a wire phantom inside a water bath. We collected the experimental data using a Verasonics Vantage Ultrasound System (Verasonics, Inc., Kirkland, WA) and a C5-2 curvilinear array transducer. 128 A-lines were acquired over a 75° sector. Table 3.3 summarizes the operation settings for the curvilinear probe and the ultrasound system. The experimental data were processed using the same beamforming and post-processing methods as the simulated data.

Table 3.3: Curvilinear Probe and System Setting

Parameter	Value
Sector	75°
Number of elements	128
Pitch	0.425 mm
Center frequency (f_c)	3.125 MHz
Sampling frequency (f_s)	12.5 MHz
Bandwidth	60%
Transmit focal depth	3 cm
Transmit/Receive f/#	1.0
Speed of sound (c)	1540 m/s
in water (c_w)	1480 m/s

Additionally, because we were interested in ADMIRE's ability to preserve speckle texture while suppressing off-axis clutter, we acquired imaging data from a tissue-mimicking

phantom (Multi-Purpose Multi-Tissue Ultrasound Phantom 040GSE, CIRS Inc., Norfolk, Virginia, USA). We used the same settings as in the case of the wire phantom acquisition. The acquired data were reconstructed using the same beamformer with and without CF weighting before B-mode image formation. We quantified image quality metrics, including contrast ratio, CNR and speckle statistics of the B-mode image using the same equations of (3.3), (3.4) and (3.5), respectively.

3.2.5 *In Vivo* Data

We acquired *in vivo* data from a human subject's liver using a Verasonics Vantage Ultrasound System (Verasonics, Inc., Kirkland, WA) and a C5-2 curvilinear array transducer. The acquisition parameters are the same as those in Table 3.3. After data acquisition, we formed B-mode images using DAS and ADMIRE with and without CF weighting. We evaluated the B-mode images qualitatively, while image quality metrics were used for quantitative measurements of the images obtained from each beamforming method. The study was approved by the Vanderbilt University Institutional Review Board.

3.3 Results

Fig. 3.2 shows the set of point spread functions in 2-D (left) and 1-D spaces (right). The spatial resolution is quantified laterally and axially, indicated in Table 3.4. The dynamic range of 2-D point spread function images is 90 dB. The 1-D lateral point spread function derived from ADMIRE demonstrates that the first side-lobes are reduced to -40 dB and off-axis energy is suppressed below -100 dB, while the standard DAS reduced off-axis energy below -50 dB. Along with off-axis energy suppression, it is worth noting that the main-lobe width (-6 dB) of ADMIRE is practically unperturbed. These findings suggest that ADMIRE substantially suppress off-axis energy arriving away from the received focus without any loss in lateral resolution, and that the CF can be integrated with ADMIRE as with DAS.

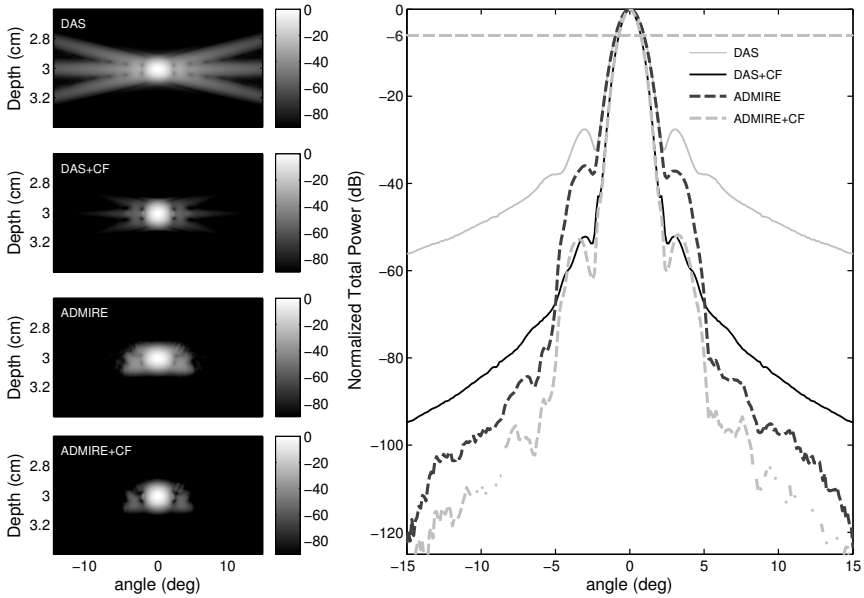

Figure 3.2: Set of 2-D (left) and 1-D (right) point spread functions simulated using standard DAS, DAS+CF, ADMIRE and ADMIRE+CF. The 1-D lateral spread functions (right), which is axially integrated, demonstrate main lobe width and side-lobes level.

Table 3.4: Quantitative Spatial Resolution (-6 dB)

	DAS	DAS+CF	ADMIRE	ADMIRE+CF
lateral (mm)	1.01	0.77	0.99	0.76
axial (mm)	0.60	0.61	0.61	0.63

Fig. 3.2 also demonstrates that DAS+CF provides lower side-lobes and a narrower main lobe than DAS and ADMIRE. The combination of ADMIRE with CF weighting (ADMIRE+CF) may be the most beneficial with respect to improvement of image resolution and contrast based on the point target data.

Fig. 3.3 demonstrates the phantom images with five point targets using DAS, ADMIRE, DAS+CF and ADMIRE+CF. The images are shown with a dynamic range of 80 dB. When comparing these images, ADMIRE shows improvement over DAS, but DAS+CF provides better resolution image than ADMIRE, which is consistent with the 1-D point spread functions in Fig. 3.2. These resulting images also indicate that the combination of ADMIRE with CF weighting may be the best method, when considering only off-axis energy suppression and lateral image resolution.

Along with the simulation results, Figs. 3.4 and 3.5 present the experimental results obtained from the acquired data using a transducer and an ultrasound imaging system. Fig. 3.4 displays the wire phantom images reconstructed using DAS, ADMIRE, DAS+CF and ADMIRE+CF. The resulting images are based on a dynamic range of 100 dB. Comparing four wire images, it is apparent that the use of CF weighting to DAS beamforming significantly improves the wire phantom image, while ADMIRE+CF also shows some improvement compared to the ADMIRE image, suggesting that ADMIRE+CF still provides the best image quality of these four images. The findings from the wire phantom images are consistent with the simulation results we demonstrated. Table 3.5 summarizes lateral and axial resolutions measured from the images in Figs. 3.3 and 3.4. However, when evaluating quantitative results in Table 3.5, both lateral and axial resolutions at 3 cm focus are slightly better with ADMIRE than DAS+CF in the case of wire phantom, which is inconsistent with simulation results. In general, the -6 dB resolution is not changed in a meaningful way, which is consistent with the way ADMIRE was implemented here.

We also evaluated ADMIRE performance with background speckle texture using a tissue-mimicking phantom. Four tissue-mimicking phantom B-mode images are demonstrated in Fig. 3.5. When carefully looking into these images, the ADMIRE may provide high contrast in and around existing cysts. Although adding CF does improve contrast and resolution as expected, it also reduces the background speckle SNR. Table 3.6 summarizes the quantitative results of image quality metrics and speckle statistics in each B-mode image. When comparing the values of measured contrast and CNR, ADMIRE outperforms DAS itself. It is important to note that ADMIRE largely preserves speckle statistics, especially, when compared with the CF weighting method.

Our evaluation of ADMIRE also identified some limitations that are consistent with other advanced beamformers [104]. Fig. 3.6 exemplifies the limitation using a fully developed speckle background with a single bright scatterer. When the single scatterer is 20 dB or even 40 dB higher compared to the background speckle signal, neither DAS nor

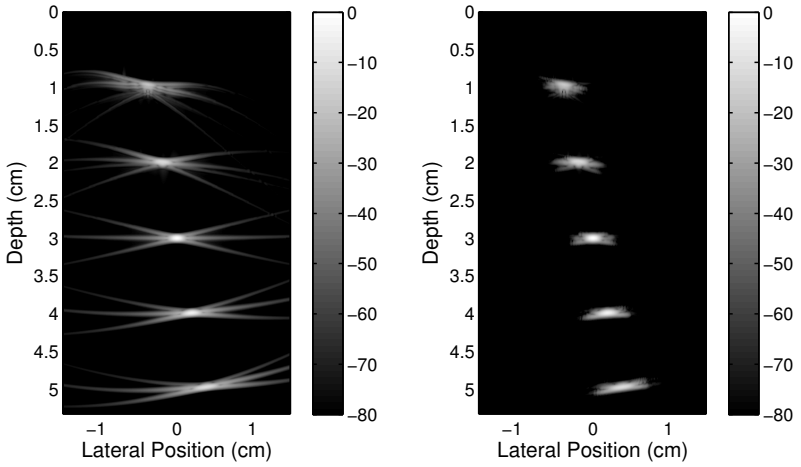

(a) DAS (b) ADMIRE

(c) DAS+CF (d) ADMIRE+CF

Figure 3.3: Simulated resolution phantom images with five point targets, mimicking a wire phantom. The images are formed by using (a) standard DAS, (b) ADMIRE, (c) DAS+CF and (d) ADMIRE+CF. The resulting images can indicate off-axis energy suppression with focused and unfocused targets using each beamforming method. The dynamic range is 80 dB in order to highlight the side-lobes.

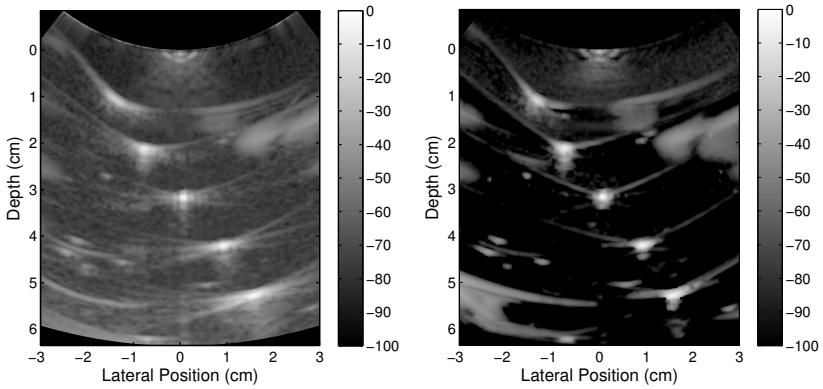

(a) DAS (b) ADMIRE

(c) DAS+CF (d) ADMIRE+CF

Figure 3.4: The experimental wire phantom images reconstructed using four different beamforming methods: (a) DAS, (b) ADMIRE, (c) DAS+CF and (d) ADMIRE+CF. The results obtained from the experimental data are correlated with simulations. The dynamic range is 100 dB to highlight side-lobes and other clutter present. The data were beamformed using sound speed of 1480 m/s.

Table 3.5: Quantitative Spatial Resolutions (-6 dB) of Figs. 3 and 4

Simulated Resolution Phantom		DAS	DAS+CF	ADMIRE	ADMIRE+CF
lateral (mm)	@(-0.4, 1.0) cm	1.49	1.09	1.42	1.03
	@(-0.2, 2.0) cm	1.75	1.26	1.73	1.23
	@(0, 3.0) cm	1.09	0.90	1.04	0.83
	@(0.2, 4.0) cm	1.56	1.23	1.50	1.15
	@(0.4, 5.0) cm	2.41	1.73	2.35	1.67
	$\mu_{lateral} \pm \sigma_{lateral}$	1.66 ± 0.48	1.24 ± 0.31	1.61 ± 0.49	1.18 ± 0.31
axial (mm)	@(-0.4, 1.0) cm	0.57	0.62	0.60	0.64
	@(-0.2, 2.0) cm	0.56	0.57	0.58	0.59
	@(0, 3.0) cm	0.43	0.45	0.46	0.48
	@(0.2, 4.0) cm	0.42	0.44	0.46	0.48
	@(0.4, 5.0) cm	0.42	0.43	0.43	0.45
	$\mu_{axial} \pm \sigma_{axial}$	0.48 ± 0.08	0.50 ± 0.09	0.51 ± 0.08	0.53 ± 0.08

Experimental Wire Phantom		DAS	DAS+CF	ADMIRE	ADMIRE+CF
lateral (mm)	@(-1.5, 1.0) cm	1.40	1.24	1.29	1.23
	@(-1.0, 2.0) cm	1.71	1.36	1.40	1.40
	@(0, 3.0) cm	1.43	1.41	1.40	1.36
	@(1.0, 4.0) cm	1.59	1.19	1.44	1.35
	@(1.5, 5.0) cm	1.99	1.61	1.72	1.66
	$\mu_{lateral} \pm \sigma_{lateral}$	1.63 ± 0.24	1.37 ± 0.17	1.45 ± 0.16	1.40 ± 0.16
axial (mm)	@(-1.5, 1.0) cm	1.13	1.11	1.05	1.08
	@(-1.0, 2.0) cm	1.15	1.07	0.89	1.01
	@(0, 3.0) cm	0.78	0.79	0.77	0.78
	@(1.0, 4.0) cm	0.84	0.83	0.85	0.83
	@(1.5, 5.0) cm	0.86	0.85	0.75	0.74
	$\mu_{axial} \pm \sigma_{axial}$	0.95 ± 0.18	0.93 ± 0.15	0.86 ± 0.12	0.88 ± 0.15

Table 3.6: Image Quality Metrics and Speckle Statistics

Beamforming	**Contrast (dB)**	**CNR (dB)**	**$\mathbf{SNR_{speckle}}$**
DAS	13.80	2.65	1.78
ADMIRE	17.33	2.71	1.68
DAS+CF	17.34	-1.29	1.03
ADMIRE+CF	18.40	0.72	1.39

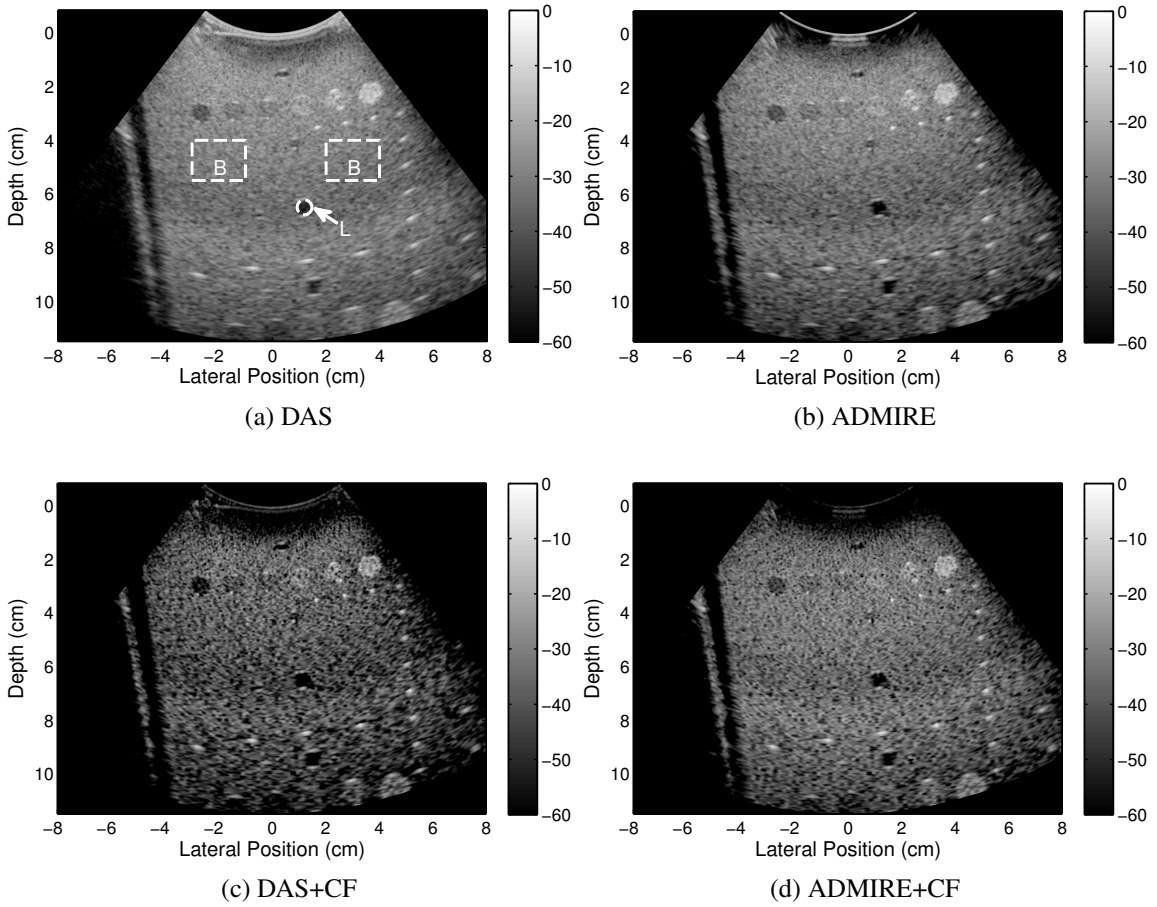

(a) DAS (b) ADMIRE

(c) DAS+CF (d) ADMIRE+CF

Figure 3.5: Tissue mimicking phantom images formed using (a) DAS, (b) ADMIRE, (c) DAS+CF and (d) ADMIRE+CF. The dynamic range is 60 dB. The DAS image in (a) also shows two enclosed areas by white dashed lines and a circle by white solid line (i.e., mask regions) that were used to quantify contrast, contrast-to-noise ratio (CNR) and speckle signal-to-noise ratio ($SNR_{speckle}$) for each imaging data. An 'L' or 'B' denotes lesion or background, respectively.

ADMIRE B-mode images show any noticeable difference, but images with CF weighting decrease speckle texture, especially around the strong scatterer. However, as the ratio between a strong scatterer to the background signal increases, the image resulting from the application of ADMIRE with low degrees of freedom suppresses the background signal in the region of the side-lobes, similar to the CF images. However, DAS maintains background speckle, but the off-axis clutter from the bright scatterer persists. The trend is more definitive when a single scatterer is very strong such as the ratio 60 dB or 80 dB. When comparing the two ADMIRE B-mode images using low and high degrees of freedom, it is apparent that image artifacts around a bright scatterer (i.e., dark region) decrease when implementing ADMIRE with high degrees of freedom; especially, in the case of 60 dB. These results suggest that ADMIRE performance and its limitations depend on deliberate selection of the regularization parameters, especially λ, which sets the degrees of freedom.

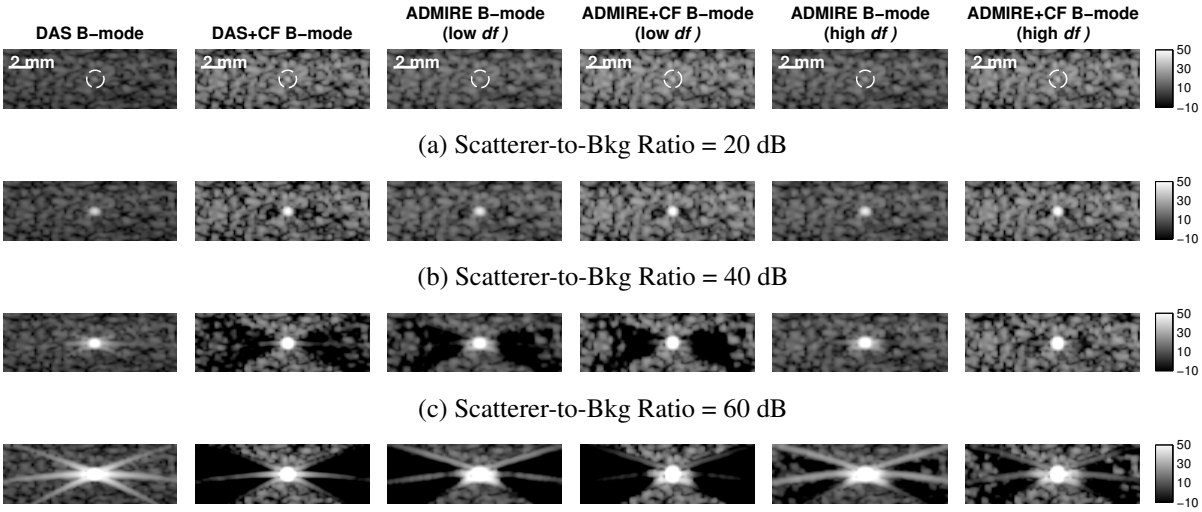

(a) Scatterer-to-Bkg Ratio = 20 dB

(b) Scatterer-to-Bkg Ratio = 40 dB

(c) Scatterer-to-Bkg Ratio = 60 dB

(d) Scatterer-to-Bkg Ratio = 80 dB

Figure 3.6: Speckle-based target simulations in the presence of a strong scatterer (circled) underlying background speckle to identify potential limitations of the various beamforming methods. The strong scatterer is scaled by a scatterer-to-background ratio (SBR) 20 dB, 40 dB, 60 dB and 80 dB. We then apply DAS, DAS+CF, ADMIRE and ADMIRE+CF to compare the resulting images. Two sets of the resulting images from applying ADMIRE and ADMIRE+CF are with low and high degrees of freedom (*df*) cases. The images are scaled so that the speckle background is at 0 dB. The dynamic range of all images is 60 dB (i.e., -10 to 50 dB).

Figs. 3.7 and 3.8 demonstrate the impact of sound speed errors on ADMIRE performance. In Fig. 3.7, ADMIRE shows lower lateral FWHM (i.e., better lateral resolution) than DAS, particularly, in the range of sound speed below 1540 m/s. (Note that Fig. 3.7 (d) reports that the lowest FWHM is measured at $c_{actual}/c_{assumed} = 0.98$ when applying ADMIRE and ADMIRE+CF.) It is noted that DAS+CF and ADMIRE+CF show better resolution than DAS and ADMIRE over the range of sound speed variation. It is also worth noting that the impact of sound speed errors largely mimics traditional beamforming (i.e., standard DAS) and ADMIRE never does worse.

The impact of sound speed inhomogeneities is shown in Fig. 3.8, which shows contrast, CNR and speckle SNR. In general, ADMIRE does not do worse than DAS for moderate deviations in sound speed despite being model-based, which is based on an assumed sound speed. It is interesting that the peak contrast for ADMIRE does occur at a slightly lower sound speed than for DAS, which is consistent with the results seen in Fig. 3.7.

Fig. 3.9 shows four *in vivo* images formed by applying DAS and ADMIRE, before and after CF weighting. We also measured contrast, CNR and $\text{SNR}_{\text{speckle}}$, as indicated in Table 3.7. The quality of the resulting *in vivo* B-mode images suggest that ADMIRE suppresses clutter and provides well-delineated anatomy (i.e., lesions) while preserving tissue speckle texture. However, use of CF weighting after applying DAS and ADMIRE may degrade speckle texture, resulting in lower CNR and lower $\text{SNR}_{\text{speckle}}$. The values of image quality metrics and speckle statistics in Table 3.7 are consistent with the qualitative evaluation of Fig. 3.9. These findings from *in vivo* data are also correlated with results from simulations and experimental phantoms.

Table 3.7: *In Vivo* Image Quality Metrics and Speckle Statistics

Beamforming	**Contrast (dB)**	**CNR (dB)**	**$\text{SNR}_{\text{speckle}}$**
DAS	17.22	3.75	1.82
ADMIRE	28.61	3.63	1.61
DAS+CF	28.25	0.70	1.13
ADMIRE+CF	29.58	1.66	1.27

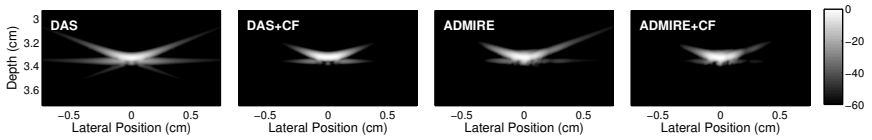

(a) $c_{actual}/c_{assumed} = 0.9$

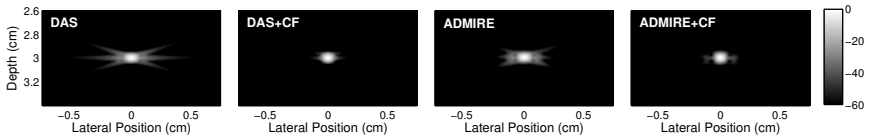

(b) $c_{actual}/c_{assumed} = 1.0$

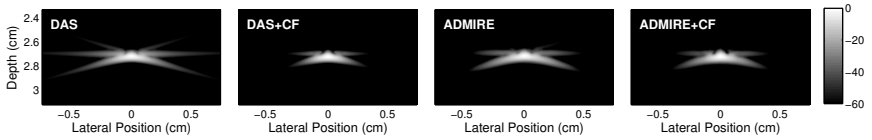

(c) $c_{actual}/c_{assumed} = 1.1$

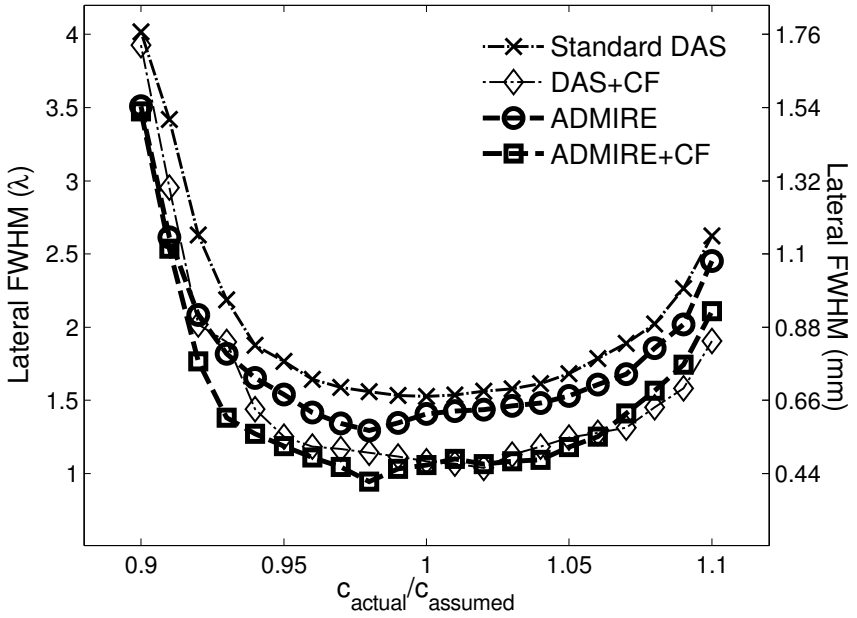

(d) FWHM length as a function of sound speed variation

Figure 3.7: The full-width and half-maximum (FWHM) beam width at the peak on-axis as a function of sound speed error. We apply the assumed sound speed, $c_{assumed}$ = 1540 m/s, and the range of deviation is $\pm$ 10%. The resolution target phantom images obtained from four beamforming methods, with (a) -10%, (b) 0% and (c) $+10\%$ sound speed variation, are shown. The lateral FWHM lengths as a function of sound speed variation are plotted in (d).

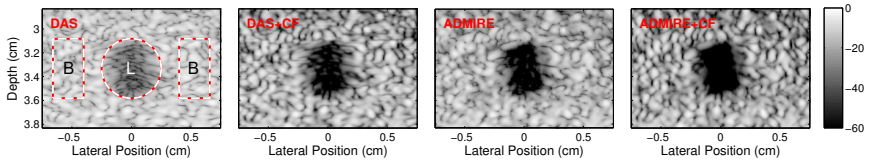

(a) $c_{actual}/c_{assumed} = 0.9$

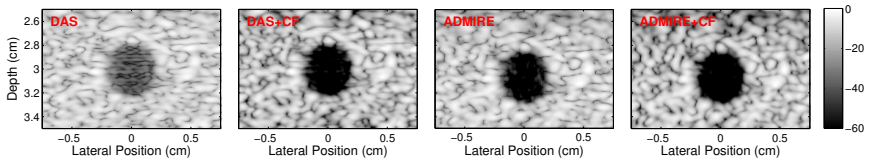

(b) $c_{actual}/c_{assumed} = 1.0$

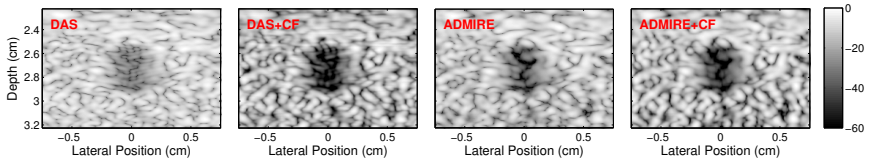

(c) $c_{actual}/c_{assumed} = 1.1$

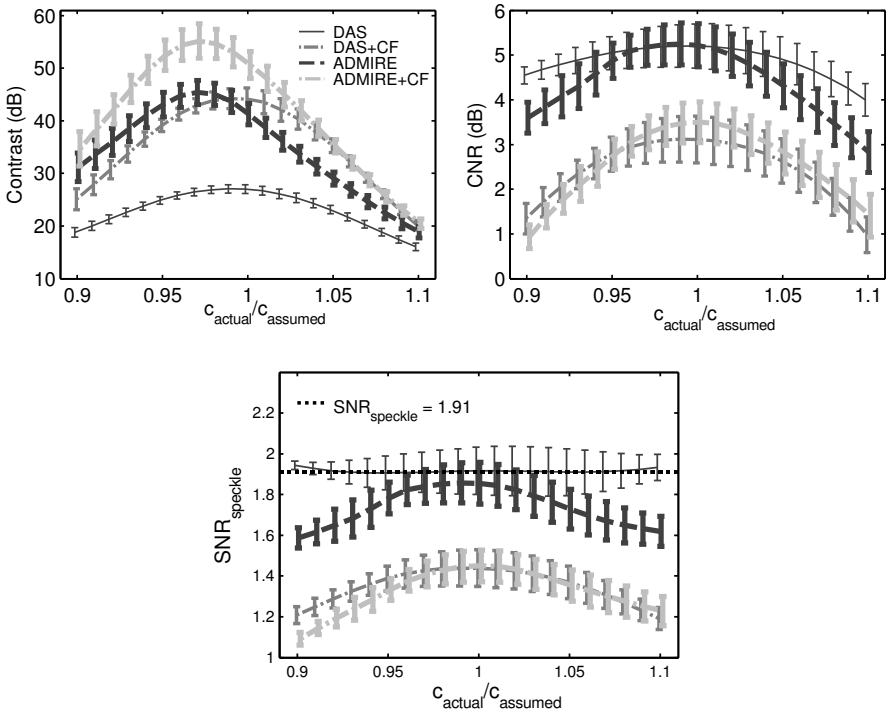

(d) Contrast, CNR and $\text{SNR}_{\text{speckle}}$ as a function of sound speed variation

Figure 3.8: The measurements of contrast, CNR and speckle SNR ($\text{SNR}_{\text{speckle}}$) as a function of sound speed mismatch. The assumed sound speed is $c_{assumed}$ = 1540 m/s with the range of deviation of $\pm$ 10%. The anechoic cyst images formed from four beamforming methods are presented in sound speed mismatch of (a) -10%, (b) 0% and (c) $+10\%$. The DAS in (a) also shows mask regions that were used to quantify contrast, CNR and $\text{SNR}_{\text{speckle}}$ for each image. The regions are indicated by the red and white contour lines with an 'L' or 'B', denoting lesion or background, respectively. The measurement results of contrast, CNR and $\text{SNR}_{\text{speckle}}$ are demonstrated in (d).

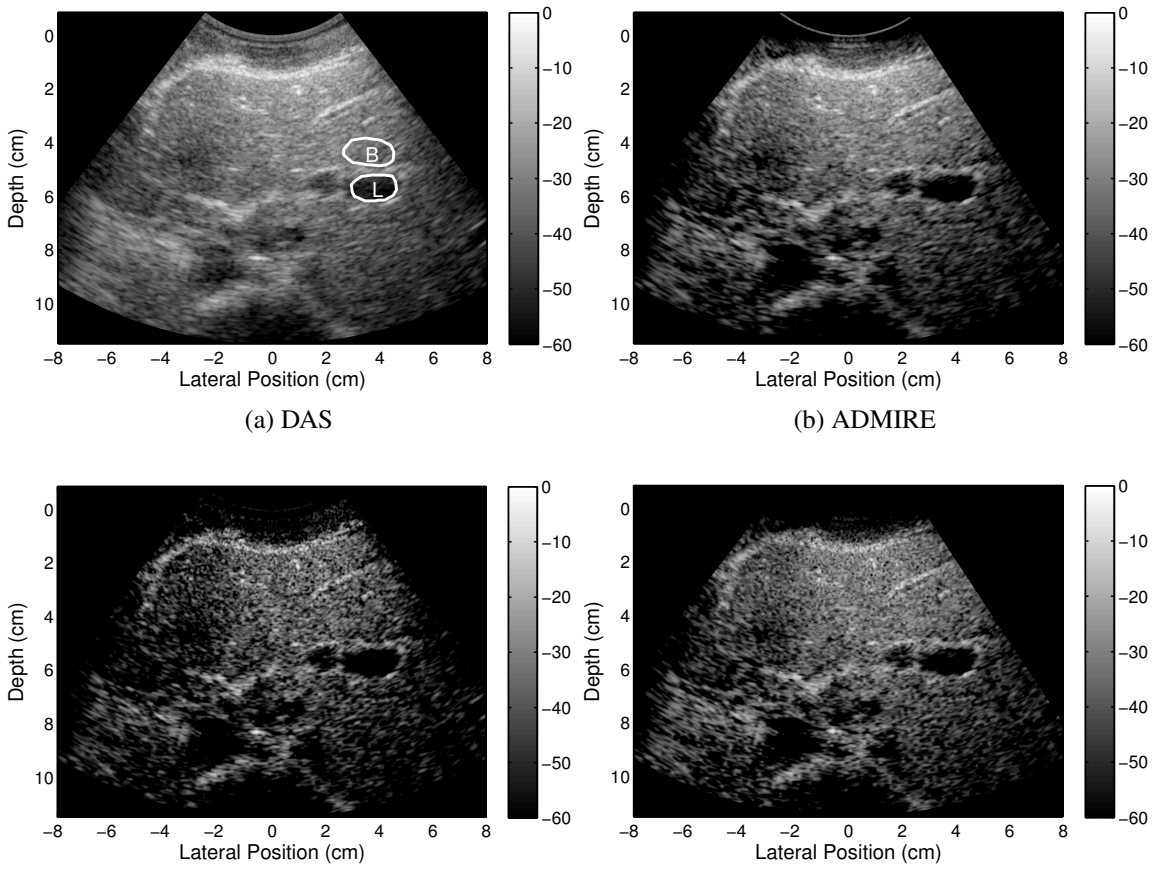

(a) DAS (b) ADMIRE

(c) DAS+CF (d) ADMIRE+CF

Figure 3.9: *in vivo* liver images reconstructed using (a) DAS, (b) ADMIRE, (c) DAS+CF and (d) ADMIRE+CF. The dynamic range is 60 dB. The DAS image in (a) also includes mask regions indicated by the white contour lines with an 'L' or 'B', denoting lesion or background, respectively. The regions were used to measure contrast, contrast-to-noise ratio (CNR) and speckle signal-to-noise ratio ($SNR_{speckle}$) for each B-mode image.

3.4 Discussion

We investigated the robustness of model-based beamforming in the presence of off-axis clutter and sound speed inhomogeneities. The results from simulations and experimental phantom data in Figs. 3.2, 3.3 and 3.4 demonstrate that ADMIRE is useful to substantially reduce off-axis artifacts in B-mode images, and offers flexible features to combine with other beamforming methods. In this study, we show that ADMIRE with CF weighting further improves some aspects of image quality. There are, however, some drawbacks of using CF as an adaptive weighting method. The resulting images after the CF weighting show slightly decreased axial resolution as indicated in Tables 3.4 and 3.5, and the CF weighted images also have lower CNR and lower SNR compared to the images without CF weighting. This is primarily driven by the degradation of background speckle, which is a known problem with CF like techniques. Some of these effects can be mitigated by using the generalized coherence factor (GCF) introduced by Li *et. al* [81]. However, we did not use it to avoid introducing an additional confusing parameter in this study.

We also identified ADMIRE's potential limitations in suppressing clutter, as shown in Fig. 3.6. ADMIRE still has a higher dynamic range than DAS [105]. The results suggest that in some cases ADMIRE may discard wanted signals (i.e., signals of interest), particularly, when low degrees of freedom are used in the presence of high levels of clutter. In general, it is necessary to use higher degrees of freedom with higher clutter scenarios when implementing ADMIRE. For example, applying ADMIRE, with higher degrees of freedom (i.e., lower λ value), mitigated dark region artifacts around a bright scatterer in an image, as demonstrated in Fig. 3.6. It can thus be suggested that it is possible to address these limitations by carefully selecting the ADMIRE tuning parameters. The deliberate selection of ADMIRE parameters may also increase ADMIRE's dynamic range [105]. Dynamic range is an underappreciated quality factor of ultrasound beamforming.

In simulations, we demonstrated that ADMIRE is also robust in the presence of sound speed mismatch. Fig. 3.7 demonstrates that ADMIRE outperforms DAS in lateral resolu-

tion within the range of sound speed variation. We show that the benefits of CF on DAS largely hold for ADMIRE, as well. In evaluating ADMIRE performance using anechoic cyst phantoms, we quantified contrast and CNR using the data inside and outside an anechoic cyst, along with speckle statistics of outside (i.e., background). Referring to Fig. 3.8, although ADMIRE is largely robust to sound speed, it is clear that CNR and $\text{SNR}_{\text{speckle}}$ does degrade with large sound speed mismatch. It is also worth noting that DAS+CF and ADMIRE+CF beamforming boosts contrast, compared to DAS and ADMIRE alone, but the CNR and $\text{SNR}_{\text{speckle}}$ are shown to be much lower than those of DAS and ADMIRE. These findings are consistent with the results reported from tissue-mimic phantom experiment and *in vivo* liver data.

One unexpected finding in this simulation is that the cases applying ADMIRE, with and without CF weighting, provide the best resolution and the highest image contrast at lower sound speed than the beamformed sound speed; e.g., the post-ADMIRE lateral FWHM has the shortest length at $c_{actual}/c_{assumed} = 0.98$, while contrast measured after ADMIRE show the highest peak occurred at $c_{actual}/c_{assumed} = 0.97$. A possible explanation for these results may be related to degrees of freedom selected when implementing ADMIRE. Because gross sound speed deviation increases acoustic clutter, the required degrees of freedom of optimal imaging may increase. As an artifact of this, the resolution appears to improve but eventually at the lost of speckle texture.

Finally, we applied ADMIRE to *in vivo* liver data to assess the results obtained from simulations and phantom experiments. It is no surprise that the ADMIRE B-mode image has a boost over 10 dB in contrast compared with the DAS B-mode image, as indicated in Table 3.7. It could be possible that the ADMIRE *in vivo* images could improve further implementing ADMIRE with a complete model space that also accounts for reverberation clutter. But, the results from the *in vivo* data are largely consistent with the findings from simulations and phantom experiments.

3.5 Conclusions

In this study, we demonstrated that ADMIRE, a model-based beamforming algorithm, substantially suppresses off-axis clutter while preserving resolution, compared to images obtained from DAS. By using post-ADMIRE decluttered channel data, we also showed that ADMIRE, combined with other algorithms, further improves some image metrics. Finally, we demonstrated that ADMIRE is robust to model-mismatch caused by gross sound speed mismatch, indicating its usefulness in real-clinical applications.

Chapter 4

THE IMPACT OF MODEL-BASED BEAMFORMING ON CLUTTERED, ABERRATED WAVEFRONTS

This work was originally published in [101]:

K. Dei and B. Byram, "The Impact of Model-Based Clutter Suppression on Cluttered, Aberrated Wavefronts," *IEEE Transaction on Ultrasonics, Ferroelectrics, and Frequency Controls*, vol. 64, no. 10, pp. 1450-1464, 2017.

4.1 Introduction

Ultrasound is a non-invasive, real-time and affordable imaging modality that is widely used as a diagnostic tool. However, image quality can limit the usefulness of ultrasound. There are many potential causes that degrade ultrasound images, including attenuation, gross sound speed error, phase aberration and reverberation clutter [3, 38, 39, 40, 7, 41]. Over the past few decades, significant attention has been paid to wavefront distortion from sound speed variation throughout inhomogeneous media. The resulting degradation is primarily thought to be arrival time variation called phase aberration. In order to minimize the effects of phase aberration, many methods have been developed to correct distorted wavefronts [40, 42, 43, 44, 45, 46, 47, 48, 49].

Recent studies reveal that both phase aberration and reverberation are primary contributors to degraded image quality [7]. While phase aberration effects are caused by variations in sound speed due to tissue inhomogeneity, reverberation is caused by multiple reflections within inhomogeneous medium, generating clutter that distorts the appearance of the wavefronts from the region of interest [2]. For our purposes, we consider reverberation and multipath scattering to be identical mechanisms of clutter because they both induce a time delay on the echo arrival time. Along with these effects, off-axis scattering, arising from

scatterers located away from the beam's axis also generates clutter and degrades image quality.

There are early studies of multipath scattering in the field of ultrasound in medicine [106, 107, 108, 109, 110]. As an example, Nicolas *et al.* estimated multipath scattering *in vivo* at approximately -30 dB relative to scattering signals of interest [108]. Generally, multipath scattering was disregarded as a negligible contribution compared to the overall quality of the imaging systems at the time. However, more recent work suggests that on modern systems accounting for multipath scattering may be just as important as correcting aberrated wavefronts [7]. This motivated some to reconsider multipath scattering as a significant source of *in vivo* image degradation in need of new methods for correction [58, 111, 112, 64]. Byram *et al.* introduced an aperture domain model-based algorithm that decomposes and suppresses multipath scattering and off-axis scattering, while preserving signals of interest [69, 70, 41, 50]. This algorithm is called aperture domain model image reconstruction (ADMIRE). We can use post-ADMIRE channel data to estimate aberration profile characteristics and determine the relative contributions of reverberation and phase aberration on *in vivo* image quality.

Our motivation for this study is to investigate phase aberration corruption and correction in the presence of reverberation within the context of our ADMIRE algorithm. ADMIRE is useful in this regard because it can declutter the signal while preserving the channel data, which allows us to observe wavefronts before and after decluttering. As part of this, we have previously observed that ADMIRE appears to reduce the aberration in distorted wavefronts[113], but we hypothesized that it would be better to correct for aberrated wavefronts using conventional aberration correction techniques. Therefore, we introduced an adaptive component to the original ADMIRE algorithm, which we refer to as adaptive ADMIRE. The goal of adaptive ADMIRE is to more efficiently suppress clutter, while allowing the aberrated aspects of the signal from the region of interest to pass through the ADMIRE decomposition unaltered so that they can be characterized or corrected using dedicated

approaches. Adaptive ADMIRE has two uses. First, it allows us to test our hypothesis regarding the best way to address aberration, and second, it allows us to more accurately classify phase aberration in the presence of strong reverberation or off-axis clutter.

Here, we describe adaptive ADMIRE and use simulations to show adaptive ADMIRE more efficiently preserves the distortions of aberrated wavefronts. Then, we use ADMIRE, adaptive ADMIRE and conventional techniques to characterize phase aberration on *in vivo* liver data. Finally, because ADMIRE suppresses aberration, we perform a limited evaluation of image quality using simulations and *in vivo* data to determine how ADMIRE and adaptive ADMIRE perform with and without aberration correction.

4.2 Methods

4.2.1 Aberration Estimation Method

We applied a multi-lag technique to estimate aberration profiles [114]. A window of 14 wavelengths was extracted from the data record of each channel [48]. In this method, a channel signal was compared with five neighboring channels in both directions to estimate relative time delay. The relative time delays were estimated using Loupas' 2-D autocorrelation algorithm [115].

In order to determine absolute wavefront delays, the relative delay estimates may be combined into a matrix formulation [116].

$$M\tau_{aber} = \Delta\tau_{aber}, \tag{4.1}$$

where M is the design matrix of channel lags, τ_{aber} is the estimated aberration profile, and $\Delta\tau_{aber}$ are the relative time delay estimates. The estimated aberration profile, τ_{aber}, is computed by solving the pseudo-inverse matrix [114],

$$\tau_{aber} = (M^\top M)^{-1} M^\top \Delta\tau_{aber}. \tag{4.2}$$

4.2.2 Adaptive ADMIRE

In order to enable ADMIRE to effectively preserve phase aberration while decluttering, we introduce adaptive ADMIRE so that we can address aberration directly using conventional methods. We highlight two key steps in converting ADMIRE into adaptive ADMIRE. First, we apply a spatial low pass filter to obtain an initial estimate of aberration, and second, we adapt the ADMIRE model in the region of interest with the estimated aberration profile. Fig. 4.1 presents an overview of adaptive ADMIRE.

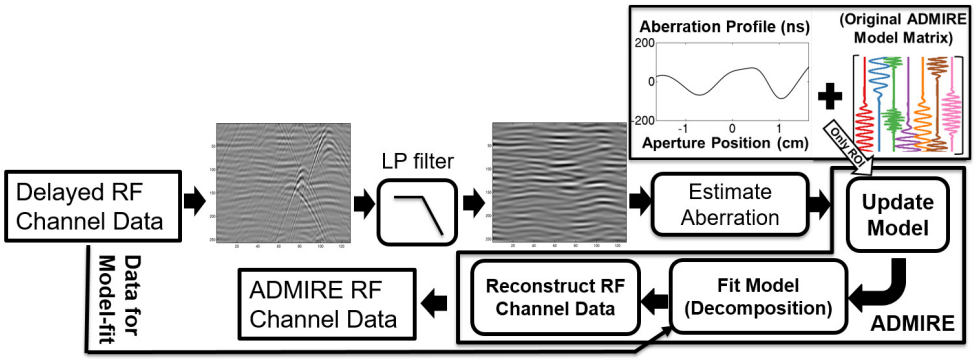

Figure 4.1: Adaptive ADMIRE data flow is illustrated. Aberration profiles are estimated from the data after spatial filtering (LP filter), while the ADMIRE model-fit is applied to the unfiltered channel data. Estimated aberration profiles are used to adaptively update the original ADMIRE model.

The spatial filter is applied to the delayed RF channel data before estimating the aberration profiles [117]. The filter is a low pass filter laterally and an all-pass filter axially, leading to a one-dimensional (1D) spatial filter. The low pass filter in the lateral dimension is just an N-tap finite impulse response (FIR) filter. In this study, we applied a 20-tap zero-phase FIR filter with a spatial cutoff frequency of 0.4 mm^{-1} across the aperture dimension unless otherwise specified [118, 117]. The filter removes high frequency spatial information, but low frequency clutter components from reverberation persist, which is what ADMIRE addresses.

Referring to Fig. 4.1, aberration profiles, τ_{aber}, which are estimated from the data after low pass filtering, are used to adaptively update the original model around the region

of interest by combining the wavefront delay, $\tau(x; x_n, z_n, \tau_n)$ in (2.1), with the estimated aberration profile,

$$\tau_{adapt}(x; x_n, z_n, \tau_n) = \tau(x; x_n, z_n, \tau_n) + \tau_{aber}(x), \tag{4.3}$$

which also impacts the amplitude modulation term $A_n(x)$ in (2.1).

To show the effect of the cutoff frequency, we performed a simulation study and then compared estimated aberration profiles from the filtered data using 0.2 mm^{-1}, 0.4 mm^{-1} and 0.6 mm^{-1} spatial cutoff frequencies, along with applied aberration.

4.2.3 Simulations

To evaluate ADMIRE and adaptive ADMIRE, we performed simulation studies using Field II [17, 18] in the presence of phase aberration and in the presence of multipath scattering and phase aberration. We performed simulations for point targets positioned at 5 cm. We also simulated channel data from diffuse scatterers with a density of 25 scatterers per resolution cell to ensure fully developed speckle [103]. We modeled a linear array transducer with 3.0 MHz center frequency and 60% fractional bandwidth. Table 4.1 indicates simulated transducer parameters, including geometry.

Table 4.1: Field II Simulation Parameters

Parameter	Value
Number of elements	128
Height of element	2 mm
Width of element	0.254 mm
Kerf	0.003 mm
Lateral pitch	0.257 mm
Center frequency (f_c)	3 MHz
Sampling frequency (simulation)	640 MHz
Sampling frequency (downsampled)	40 MHz
Bandwidth	60%
Transmit focal depth	5 cm
Transmit/Receive F/#	1.5

In order to simulate the effects of aberrated wavefronts, a zero-mean, random near-field phase screen was used to model aberration profiles. The aberration model was generated by convolving a Gaussian random process with a Gaussian function [47]. The aberration model was then applied on both transmit and receive to individual mathematical sub-elements, making up the transducer aperture. Aberration levels were characterized by the aberration profile's autocorrelation full-width at half-maximum (FWHM) and the root-mean-square (RMS). Lower autocorrelation FWHM and higher RMS are indicative of increased aberration levels. In principle, the lower autocorrelation FWHM would come from greater spatial variability in the tissues generating the aberration, whereas higher RMS would be related to larger deviations in the average sound speed relative to 1540 m/s along the path to each transducer element. We generated aberrated wavefronts of FWHM = 5.0 $\pm$ 0.1 mm, and RMS = 50 ns [71], and multipath scattering was simulated using a pseudo non-linear adaptation to Field II [4, 119]. We scaled the clutter level of multipath scattering, relative to the signal of interest (SOI) to specified signal-to-clutter ratios (SCR),

$$SCR = 10 \log 10 \left(\frac{\mathrm{P_{SOI}}}{\mathrm{P_{Clutter}}} \right). \tag{4.4}$$

When evaluating clutter, we considered three levels of 0, 10 and 20 dB SCR.

4.2.4 Error Metrics

We quantified aberration profile errors as a function of degrees of freedom

$$err_{aber} = 10 \log 10 \left(\frac{\sum (\tau_{pre} - \tau_{post})^2}{\sum \tau_{pre}^2} \right), \tag{4.5}$$

where τ_{pre} is the profile estimated from the original uncluttered data, and τ_{post} is the data after ADMIRE or adaptive ADMIRE.

We also measured FWHM and RMS percent error as a function of degrees of freedom

$$\%err_{\text{FWHM/RMS}} = \frac{\kappa_{post} - \kappa_{pre}}{\kappa_{pre}} \times 100\%, \tag{4.6}$$

where κ_{pre} is FWHM/RMS values measured on the uncluttered wavefronts, and κ_{post} is measured values after ADMIRE or adaptive ADMIRE.

Along with the above error metrics, we used a root-mean-square error (RMSE) of FWHM/RMS values quantified with aberration profiles from post-filtered and post-adaptive ADMIRE data, as a function of spatial cutoff frequencies

$$RMSE_{\text{FWHM/RMS}} = \sqrt{\frac{\sum(\upsilon_{post} - \upsilon_{applied})^2}{N_{rlz}}}, \tag{4.7}$$

where $\upsilon_{applied}$ are FWHM/RMS values measured on the uncluttered, unfiltered data, υ_{post} are the measured values after spatial filtering or adaptive ADMIRE, respectively. N_{rlz} is the number of realizations.

4.2.5 *In Vivo* Studies

We measured aberration profiles on *in vivo* liver data using ADMIRE and adaptive ADMIRE. The data were obtained from a study approved by the Duke University Institutional Review Board (IRB) with written consent provided by all participants. These data were acquired with a Siemens S2000 and 4C-1 curvilinear array (Siemens Healthcare, Ultrasound Business Unit, Mountain View, CA). Table 4.2 summarizes the *in vivo* data acquisition parameters.

Table 4.2: *In Vivo* Study Design

Data Measurement Parameters	
Parameter	Value
Transducer	4C-1 curvilinear array
Aperture length	3.05 cm
Center frequency (f_c)	4 MHz
Sampling frequency (f_s)	40 MHz
Speed of sound (c)	1540 m/s

Additionally, we computed contrast and contrast-to-noise ratio (CNR) on the B-mode images. Contrast and CNR were computed using

$$C = -20\log 10(\frac{\mu_l}{\mu_b}), \tag{4.8}$$

$$CNR = 20\log 10(\frac{|\mu_l - \mu_b|}{\sqrt{\sigma_l^2 + \sigma_b^2}}), \tag{4.9}$$

where (μ_l, ${\sigma^2}_l$) and (μ_b, ${\sigma^2}_b$) are the value of (mean , variance) of the enveloped but uncompressed data inside and outside hypoechoic structure, respectively.

4.2.6 Resolution Target and Contrast Target Simulations

Field II was used to perform resolution target simulations in the presence of phase aberration, in order to investigate and clarify the effect of ADMIRE and adaptive ADMIRE with and without aberration correction on image quality. We used the parameters in Table 4.1 for the simulations. We simulated two cases: one with resolution targets at the transmit focal depth, and the other with targets shallow to the focus. In the first case, the focal depth for transmit was fixed at a 3.0 cm depth, with a F/1.5 for transmit and receive aperture. Channel data were acquired from a simulated resolution phantom containing five point targets, located at the focal depth with lateral intervals 4, 3, 2 and 1 mm. In the second case the scatterers were fixed, but the focus was moved to 5.0 cm. Other parameters such as F/# and frequency remained constant. We generated two sets of control data from the simulated resolution phantom with no aberration—one using standard delay-and-sum (DAS) beamforming (referred to as DAS only), and the other by applying ADMIRE.

Apart from these unaberrated data, aberrated data were also simulated. We simulated aberrators from a combination of FWHM = 5.0 and 2.5 mm and RMS = 25 and 50 ns, modeled as zero-mean, random near-field phase screens [47]. The selected aberrator levels were consistent with those in the literature for liver and abdominal imaging [120, 121,

122, 123]. As previously described, twelve realizations were simulated for each aberrator case. We then applied normal DAS, ADMIRE and adaptive ADMIRE with and without phase aberration correction. To implement aberration correction, we used the time-shift compensation method with estimated aberration profile for each A-line channel data at a 3.0 cm depth in a 3.6 mm window (4.7 μs) [114]. Unless stated, aberration profiles are estimated from the filtered data using a spatial cutoff frequency of 0.4 mm^{-1} [118, 117].

For a metric of image quality, energy suppression was quantified with the enveloped but uncompressed B-mode data, by computing the ratio of the average intensity from adjacent point targets specified as the sum of power above -10 dB normalized by area ($\overline{I}_{sig}$) and off-axis clutter energy specified as the sum of power below -10 dB normalized by area between the two points ($I_{clutter}$), expressed by clutter ratio (CR),

$$CR = 10 \log 10 \left(\frac{\overline{I}_{sig}}{I_{clutter}} \right). \tag{4.10}$$

We then determined clutter ratios with different lateral separation lengths from DAS only and ADMIRE without aberration. We also measured the following in the presence of aberration: DAS, ADMIRE and adaptive ADMIRE with and without aberration correction. These simulations allowed us to test whether the suppression of phase aberration using ADMIRE has a positive effect on image quality.

We also simulated anechoic cyst phantoms in Field II to further evaluate the performance of ADMIRE and adaptive ADMIRE in highly aberrated wavefronts with and without reverberation clutter. The anechoic cyst was a 5 mm diameter circle 3 cm deep, while the background speckle was fully developed with a density of 25 scatterers per resolution cell [103], as indicated in the above section.

The aberration strength applied to this simulation was FWHM = 2.5 mm and RMS = 50 ns, which is modeled by a zero-mean and random near-field phase screen. We also added reverberation clutter at an SCR of 0 dB using our pseudo non-linear simulation method [4]. We then performed image quality metrics—contrast and CNR measurements indicated in

(4.8) and (4.9). The contrast and CNR values obtained after applying ADMIRE and adaptive ADMIRE were compared to those of DAS, respectively. We also corrected aberrated wavefronts using the same correction method we applied in resolution target simulation. We then measured contrast and CNR from aberration corrected data for DAS, ADMIRE and adaptive ADMIRE, respectively. There are 6 independent speckle realizations prepared for the speckle-based target simulation.

4.3 Results

4.3.1 Aberration Profile Measurements in Simulations

Fig. 4.2 (a) and (b) show two examples of wavefronts and estimated aberration profiles from a point target and diffuse scattering simulations in the presence of phase aberration and in the presence of multipath scattering and phase aberration. The results suggest reverberation clutter could distort the appearance of wavefronts from the region of interest. Both estimated aberration profiles with 0 and 10 dB signal-to-clutter ratios were distorted in the point target and diffuse scattering simulations. Aberration profiles in simulations with a lower clutter level (SCR = 20 dB) are comparable to cases without additional clutter. These results reveal how multipath scattering could impact aberration profile measurements.

4.3.2 Aberration Profile Errors from Simulations

Figs. 4.3 and 4.4 show measured aberration profile errors, including wavefront reconstructions for three different degrees of freedom for the ADMIRE decomposition. Fig. 4.3 shows the first set of results. The first set of results from a point target and diffuse scattering simulations derived from ADMIRE and adaptive ADMIRE in the presence of phase aberration are shown. Results in Fig. 4.3 (a) and (b) suggest ADMIRE suppresses phase aberration when the degrees of freedom are low. In contrast, Fig. 4.3 (c) and (d) show that adaptive ADMIRE preserves phase aberration based wavefront distortion even at low de-

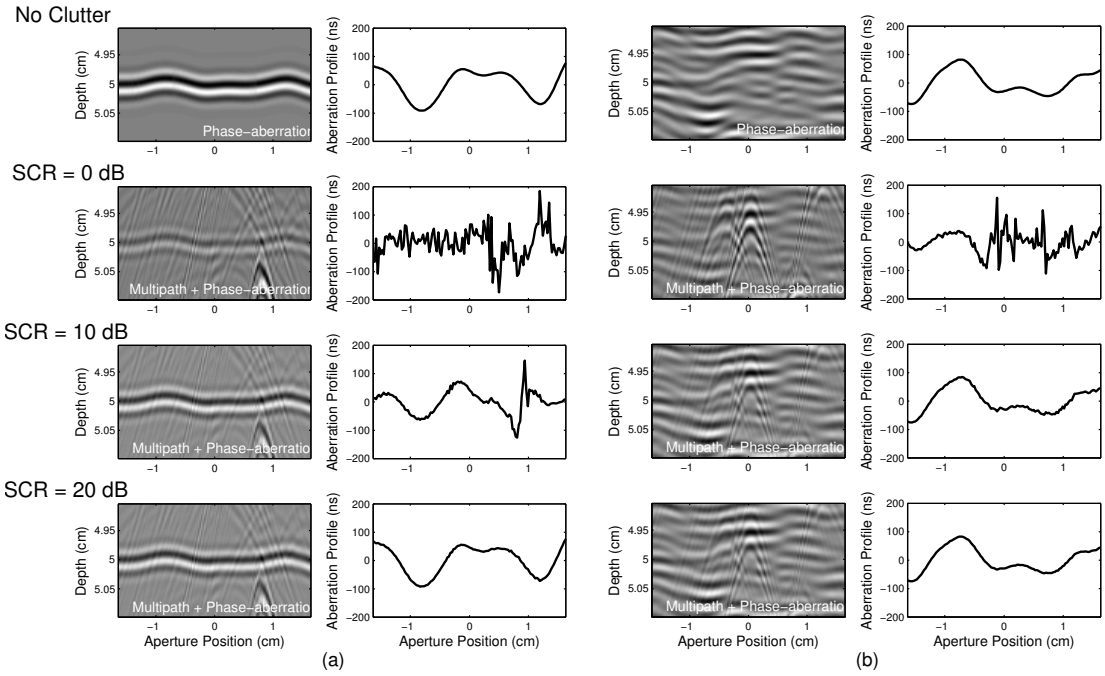

Figure 4.2: Simulations in the presence of phase aberration (No Clutter), and in the presence of multipath scattering and phase aberration with three different clutter levels (SCR = 0, 10 and 20 dB), having (a) a point target and (b) diffuse scattering. Four wavefronts (left) in each case of simulations, with corresponding estimated aberration profiles (right), are shown.

grees of freedom indicating that adaptive ADMIRE produces a more parsimonious model in the presence of phase aberration, meaning that the model produces a better fit with fewer degrees of freedom.

Fig. 4.4 illustrates a point target and diffuse scattering simulations, using ADMIRE and adaptive ADMIRE, in the presence of multipath scattering and phase aberration. Fig. 4.4 qualitatively demonstrates that ADMIRE and adaptive ADMIRE suppress most clutter. Fig. 4.4 (c) and (d) also show that adaptive ADMIRE better preserves phase aberration in the presence of multipath scattering because aberration errors converge with lower degrees of freedom. These findings suggest that adaptive ADMIRE enables us to better characterize reverberation clutter effects and phase aberration by separating these two effects.

Comparing results from a point target and diffuse scattering simulations in the presence of phase aberration (Fig. 4.3) and in the presence of multipath scattering and phase aberration (Fig. 4.4) shows that aberration profiles estimated from diffuse scatterers have larger errors than those in a point target with the same degrees of freedom.

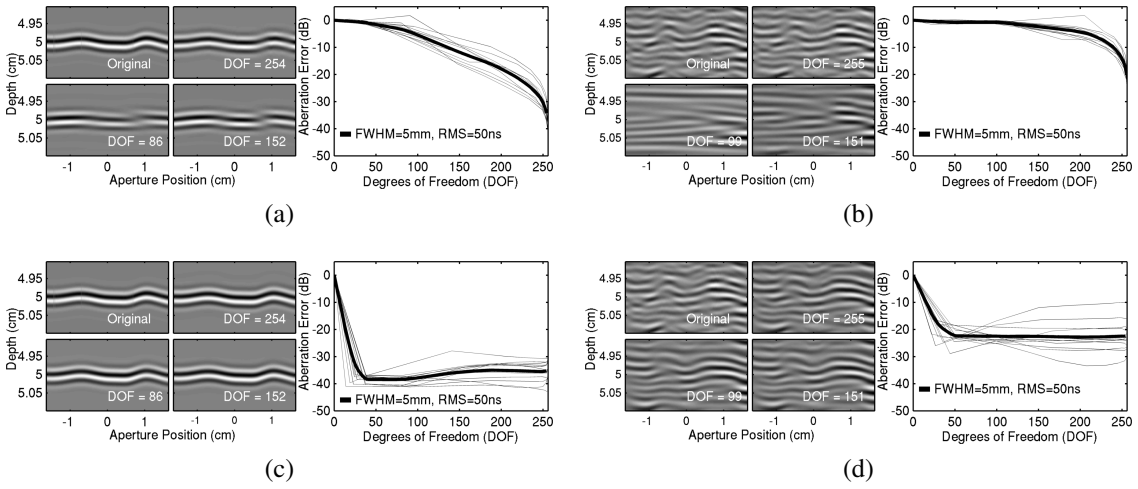

Figure 4.3: Simulations in the presence of phase aberration for a point target using (a) ADMIRE and (c) adaptive ADMIRE, and for diffuse scattering using (b) ADMIRE and (d) adaptive ADMIRE. Three wavefront reconstructions are shown for three different degrees of freedom in the model-fit (left). The error of measured aberration profiles is quantified as a function of degrees of freedom (right).

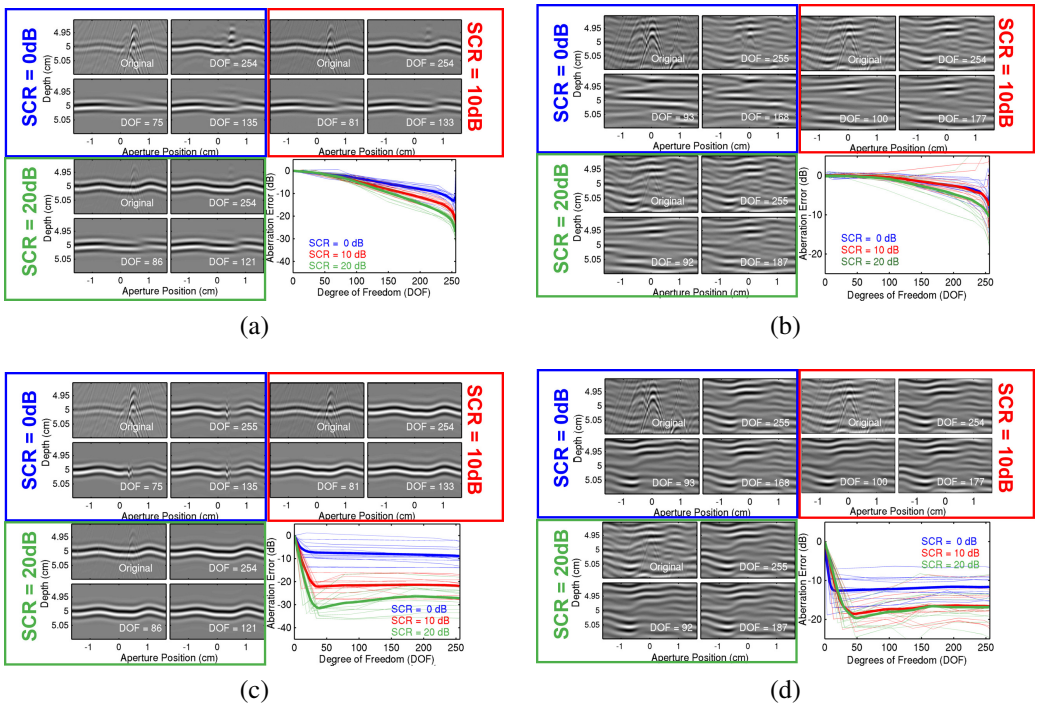

Figure 4.4: Simulation in the presence of multipath scattering and phase aberration with three different clutter levels (SCR = 0, 10 and 20 dB) for a point target using (a) ADMIRE and (c) adaptive ADMIRE, and for diffuse scattering using (b) ADMIRE and (d) adaptive ADMIRE. Each clutter level shows three wavefront reconstructions for three different degrees of freedom in the model-fit. The errors of measured aberration profiles as a function of degrees of freedom are illustrated (lower right).

4.3.3 FWHM and RMS Errors from Simulations

Fig. 4.5 presents the results from diffuse scattering simulations in the presence of multipath scattering and phase aberration, using (a) ADMIRE and (b) adaptive ADMIRE. Comparing the results of RMS errors, the RMS errors resulting from adaptive ADMIRE decrease and converge quickly with lower degrees of freedom, relative to ADMIRE. These results indicate that ADMIRE does not efficiently reproduce aberrated wavefronts with low degrees of freedom, while adaptive ADMIRE reasonably preserves the phase aberration profile. These findings are consistent with those observed with the aberration profile errors.

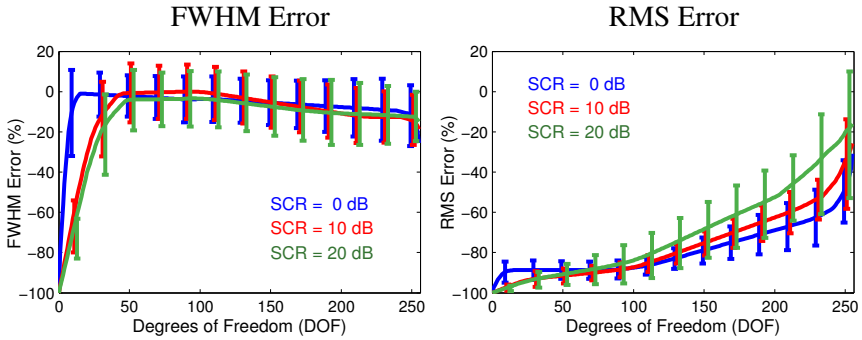

(a)

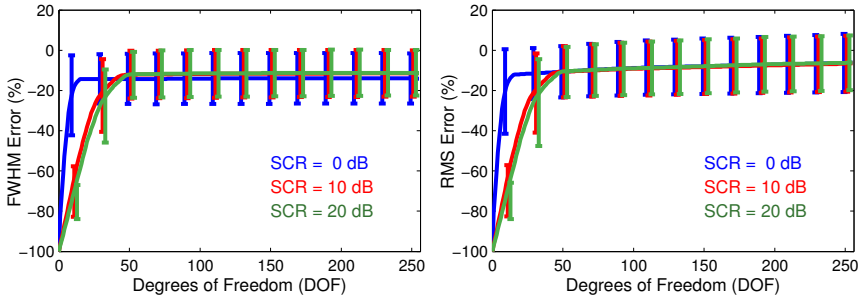

(b)

Figure 4.5: FWHM (left) and RMS (right) errors from diffuse scattering simulations in the presence of multipath scattering and phase aberration with SCR = 0, 10 and 20 dB, using (a) ADMIRE and (b) adaptive ADMIRE. The aberration level is FWHM = 5.0 $\pm$ 0.1 mm and RMS = 50 ns.

4.3.4 Root-Mean-Square Errors of FWHM and RMS from Simulations

Fig. 4.6 shows the results of computing RMSE of aberration profiles' FWHM and RMS values, from several different scenarios, as a function of three spatial filter cutoffs including an unfiltered case. These scenarios included aberrated wavefronts that are uncluttered, and aberrated wavefronts that are cluttered with 0 and 10 dB SCR, but not including 20 dB SCR case because of minimal differences from the uncluttered case. The results of spatial filtering are consistent with the literature [117, 118]. We also observe that spatial cutoff frequencies of 0.4 mm^{-1} and 0.6 mm^{-1} may not make much of a difference in the presence of moderate clutter when comparing wavefronts obtained after filtering and adaptive ADMIRE. These findings suggest that adaptive ADMIRE is effective in preserving the distortion of aberrated wavefronts in the presence of strong clutter environments, in conjunction with spatial filtering with appropriate cutoff frequencies.

4.3.5 Energy Suppression from Resolution Simulations

Because we observed that ADMIRE leads to suppressed levels of aberration, we report some simple results related to image quality. Figs. 4.7 and 4.8 present the simulated resolution phantom and the measured energy suppression with four lateral separation intervals and four sets of different aberration levels at (a) focus at the target depth, (b) focus past the target depth. The simulated data include DAS only, ADMIRE with no aberration, 12 realizations for DAS with aberration, post-ADMIRE and post-adaptive ADMIRE with and without phase aberration correction at (a) focus at the target depth, (b) focus past the target depth, respectively. The simulations reveal several points. First, as expected, phase aberration lowers spatial resolution and degrades image quality due to higher side-lobes. Second, phase aberration correction applied to post-ADMIRE data provides little additional improvement, while DAS and post-adaptive ADMIRE with aberration correction shows some improvement, particularly in the cases with higher aberration levels. Lastly, adaptive AD-

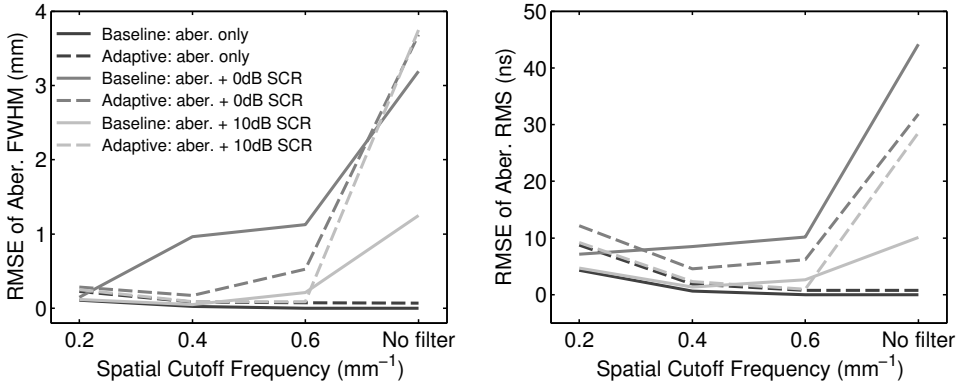

(a)

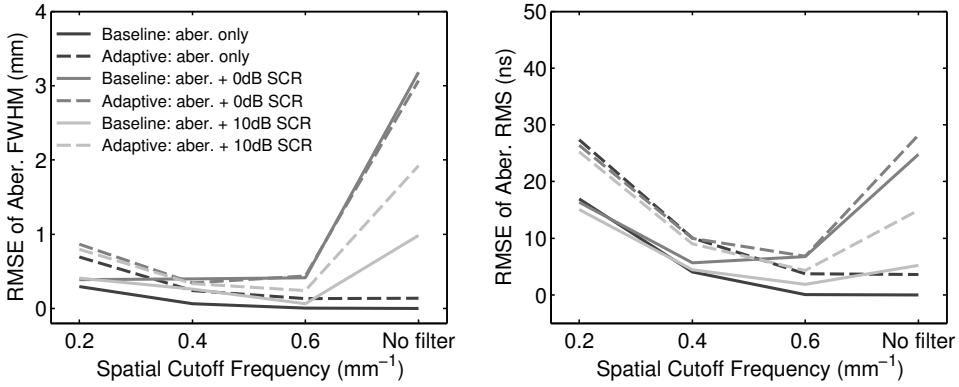

(b)

Figure 4.6: Root-mean-square errors (RMSE) of FWHM (left) and RMS (right) quantified with aberration profiles estimated from post-filter and post-adaptive ADMIRE channel data in the presence of aberration and in the presence of clutter and aberration, using (a) a point target and (b) diffuse scattering simulations. The level of aberrated wavefronts are FWHM = 5.0 $\pm$ 0.1 mm and RMS = 50 ns. The RMSE values of FWHM/RMS are compared with three various spatial cutoff frequencies of 0.2 mm^{-1}, 0.4 mm^{-1} and 0.6 mm^{-1} including an unfiltered case. The degrees of freedom when implementing ADMIRE and adaptive ADMIRE are in a range between 50 and 70.

MIRE plus aberration correction has the most benefit on image quality when the targets are close and at the focus. The results also indicate that the suppression of phase aberration as a result of ADMIRE is useful and beneficial to image quality improvement, but these results are most compelling when targets are far apart.

4.3.6 Simulated Anechoic Cyst Image Quality

Along with the resolution target simulation, we performed contrast target simulations. Fig. 4.9 demonstrates the matched simulated anechoic cyst phantom images formed after applying DAS, ADMIRE and adaptive ADMIRE, with and without aberration correction. When compared to DAS images, ADMIRE and adaptive ADMIRE recover image quality and provide better contrast in and around the cyst region, suppressing image degradation sources (i.e., clutter). Accounting for images after applying aberration correction method, there is no significant improvement before and after correction with qualitative measures, but we still identify small improvement in background speckle patterns in the cases of DAS and adaptive ADMIRE.

To quantify the image data in Fig. 4.9, we computed the values of contrast and CNR, as reported in Fig. 4.10. In the case of DAS with uncluttered and SCR 0 dB clutter environments, aberration correction significantly improves image quality, particularly in CNR. In principle, since adaptive ADMIRE preserves phase aberration during decluttering, we observe that ADMIRE images may have higher contrast than the images formed after applying adaptive ADMIRE, but aberration correction processed after adaptive ADMIRE may recover degraded image quality caused by wavefront distortion. Results obtained from adaptive ADMIRE with aberration correction indicates image quality improvement in contrast and CNR when compared with those values of adaptive ADMIRE. It is also interesting to note that ADMIRE and adaptive ADMIRE may be more robust in the presence of higher clutter environments, together with higher aberrated wavefronts. Additionally, these findings from the contrast target simulations are consistent with the resolution target simulation

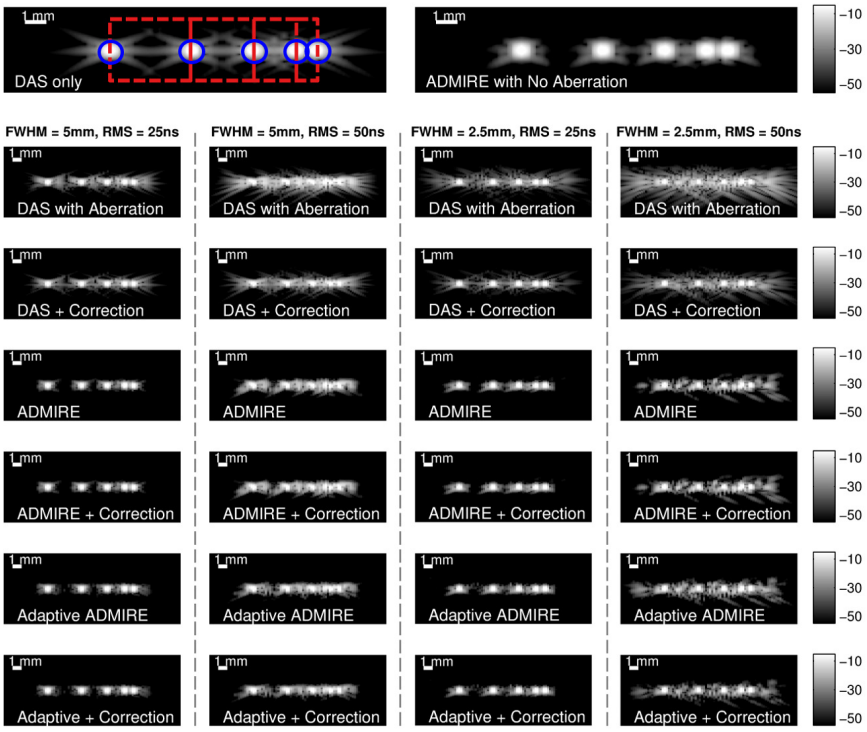

(a)

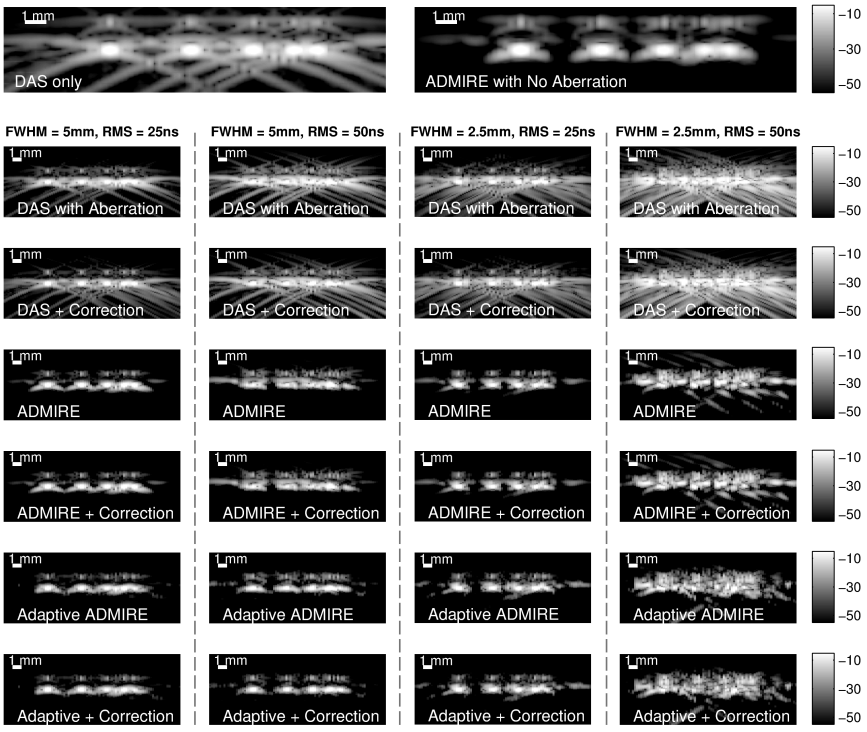

(b)

Figure 4.7: The simulated wire phantom images on resolution target simulations are presented. Four blue circles are the areas used to measure power of enveloped signal, while four sections enclosed by the red dashed lines are the areas used to measure off-axis clutter energy, for lateral separation intervals of 4, 3, 2 and 1 mm, respectively. Two images on the top row are the resolution phantoms of normal delay-and-sum (DAS) and ADMIRE with no phase aberration, respectively. Four sets of the simulated resolution phantom images with different aberrator strengths at (a) focus at the target depth, (b) focus past the target depth are also shown.

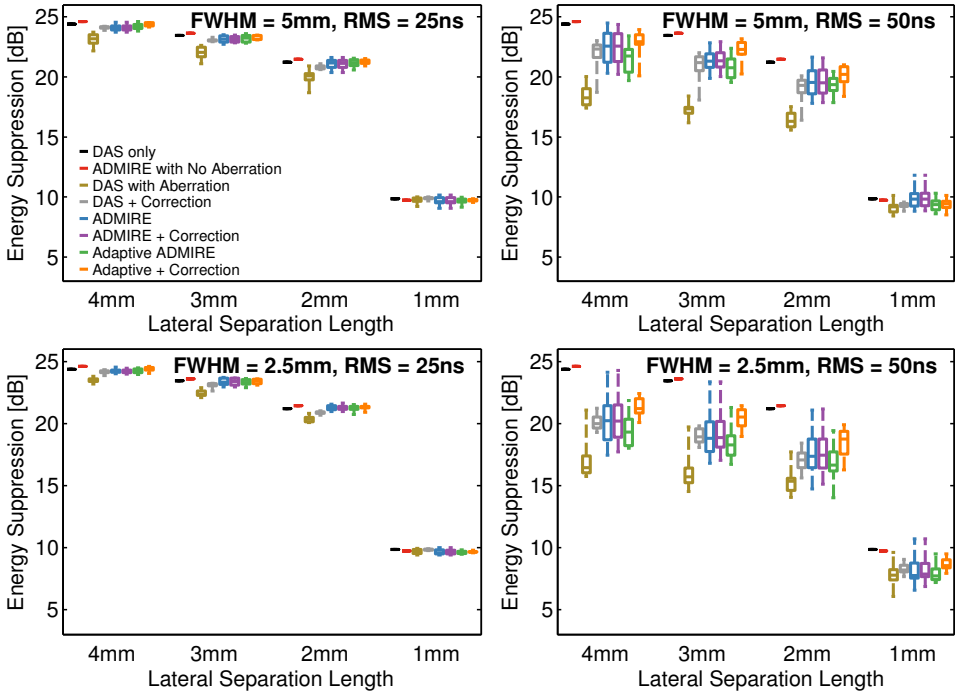

(a)

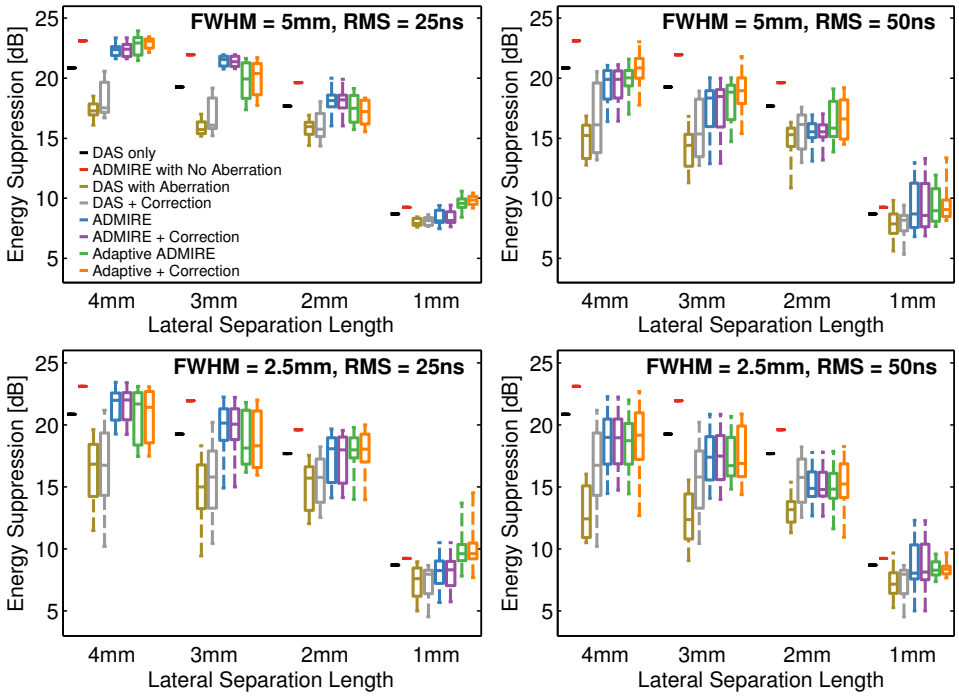

(b)

Figure 4.8: The results of measured energy suppression for several lateral separation lengths are shown as boxplots, including four sets of different aberration levels. Each set of results from the cases at (a) focus at the target depth, (b) focus past the target depth includes DAS only, ADMIRE with no aberration, 12 realizations for DAS with aberration, post-ADMIRE and post-adaptive ADMIRE with and without phase aberration correction applied. Aberration profiles are estimated from the filtered data using a spatial cutoff frequency of 0.4 mm^{-1}.

results in Fig. 4.8.

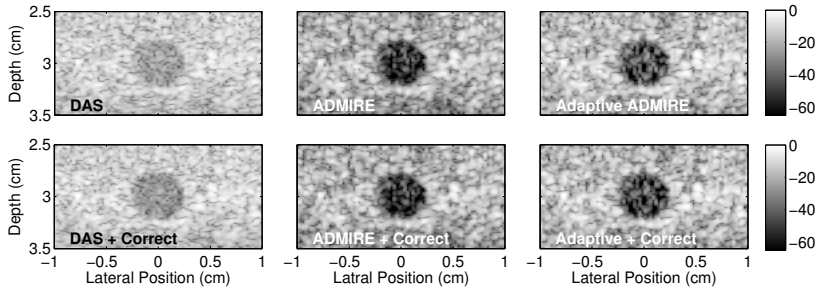

(a)

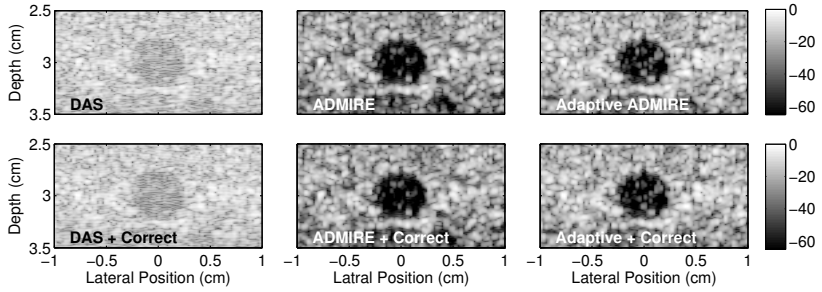

(b)

Figure 4.9: The matched simulated anechoic cyst phantom images formed after applying DAS, ADMIRE and adaptive ADMIRE with and without aberration correction in the presence of aberrated wavefronts with FWHM = 2.5 mm and RMS = 50 ns strength, in the cases of (a) uncluttered and (b) SCR = 0 dB cluttered environments, respectively.

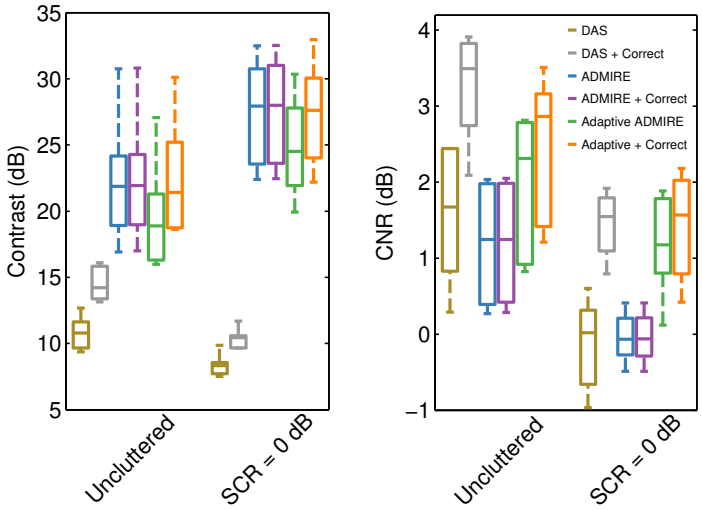

(a) (b)

Figure 4.10: The results of simulated anechoic cyst image quality metrics quantifying (a) contrast and (b) CNR for uncluttered and SCR = 0 dB clutter scenarios, respectively. There are 6 independent speckle realizations prepared for this simulation.

4.3.7 Characterization of Aberration Profiles from *In Vivo* Data

We used 13 sets of *in vivo* liver data to characterize aberration profiles. The aberration profiles' FWHM and RMS were quantified. Fig. 4.11 demonstrates wavefronts and B-mode images obtained from one example case and the matched data after applying ADMIRE, 1D spatial filter (0.4 mm^{-1} cutoff) and adaptive ADMIRE, along with the corresponding estimated aberration profiles. The results indicate that ADMIRE smooths the aberrated wavefronts and suppresses aberration, compared with the wavefronts obtained from post-adaptive ADMIRE data. It is also worth noting that the resulting B-mode images from ADMIRE and adaptive ADMIRE are qualitatively better than other images obtained from the original *in vivo* data and the post-filtered data.

Fig. 4.12 demonstrates effect of the spatial filter on *in vivo* data. Low cutoff frequencies may remove aberrated signals containing high spatial frequency components along with clutter. While, aberration estimation may be less accurate when using high cutoff frequencies due to unsuppressed off-axis or reverberation clutter corrupting aberration measurements. Fig. 4.12 also indicates that there is potential for significant bias based on the spatial filter that is chosen. This trend is particularly noticeable in Fig. 4.12 (a). However, with adaptive ADMIRE, which only uses the spatial filters as an initial estimate of the aberration profile, we observe that adaptive ADMIRE has a much wider range of estimated aberration levels. These *in vivo* results highlight a shortcoming of conventional method and demonstrate the potential role of adaptive ADMIRE for better characterizing aberrated wavefronts when there is little prior knowledge of the degree of wavefront distortion.

4.3.8 *In Vivo* Image Quality

We compare three algorithms—aberration correction, ADMIRE and adaptive ADMIRE. The aberration correction method was applied to post-ADMIRE and post-adaptive ADMIRE data. Results, as shown in Fig. 4.13, demonstrate that ADMIRE and adaptive AD-

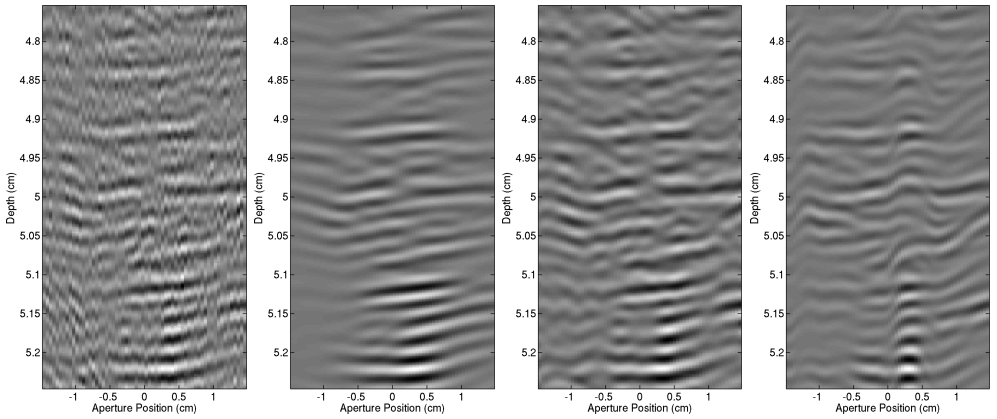

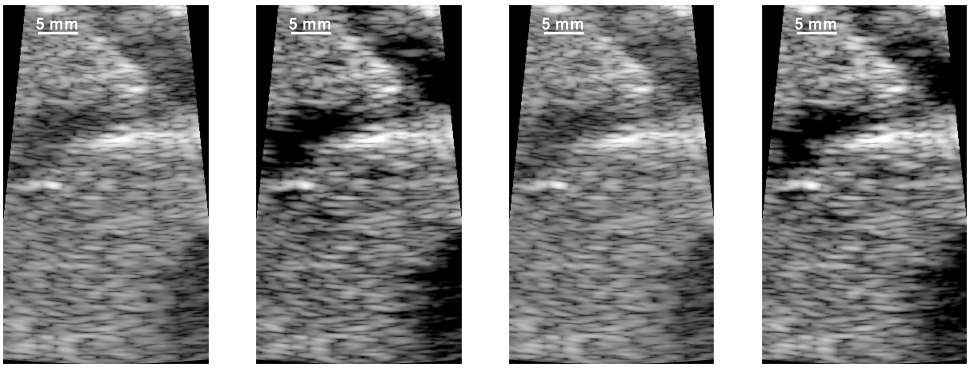

(a) (b) (c) (d)

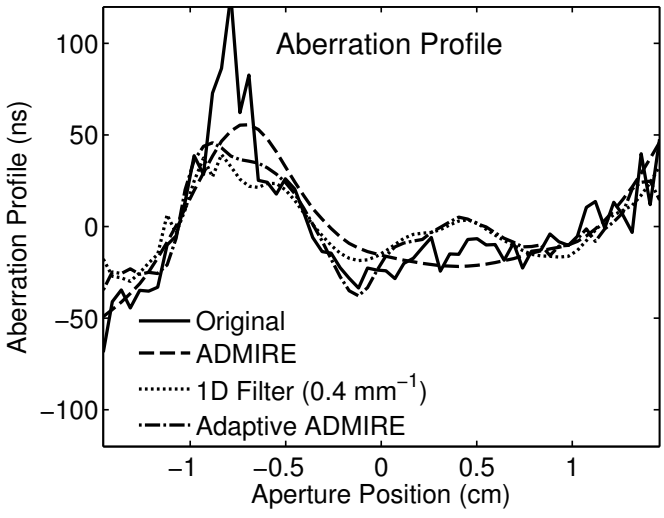

(e)

Figure 4.11: The wavefronts and corresponding B-mode images of (a) the original *in vivo* data, (b) ADMIRE, (c) 1D Filter (0.4 mm^{-1}cutoff) and (d) adaptive ADMIRE are shown, along with (i) the corresponding estimated aberration profiles. The results indicate that ADMIRE, specifically, appears to smooth the wavefront and suppresses aberration while adaptive ADMIRE seems to preserve aberration so it can be characterized more accurately.

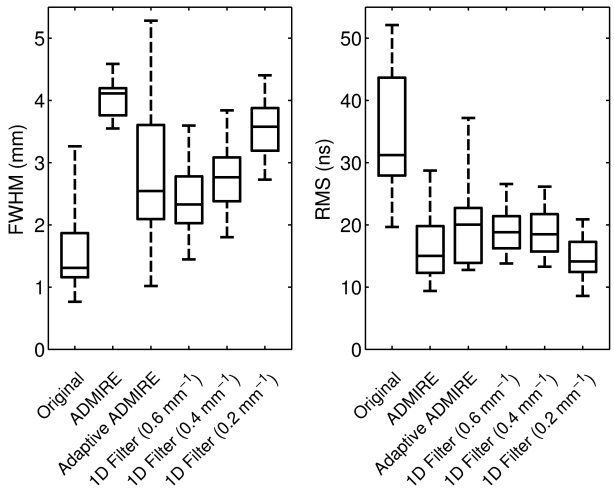

(a) (b)

Figure 4.12: The results of characterization of estimated aberration profiles from *in vivo* data are shown as boxplots. Results are shown for the original *in vivo* data, post-ADMIRE, post-adaptive ADMIRE and post-filtered data with three various spatial cutoff frequencies (0.6, 0.4 and 0.2 mm^{-1}). Aberration profiles are characterized by (a) the autocorrelation length full-width at half-maximum (FWHM) and (b) the root-mean square (RMS).

MIRE improved both contrast and CNR from normal B-mode images. Table 4.3 also summarizes the relative improvements of the contrast and CNR. These results may be based towards ADMIRE because anechoic regions visible in normal B-mode were used to quantify image quality.

Table 4.3: Relative Improvement from Original B-mode (*In Vivo*)

Algorithm	**Contrast Improvement (dB)**	**CNR Improvement (dB)**
Aberration Correction	0.090 ± 0.27	0.076 ± 0.23
ADMIRE	7.1 ± 2.5	0.86 ± 0.92
ADMIRE+Correction	6.8 ± 2.3	0.90 ± 0.89
Adaptive ADMIRE	6.6 ± 2.7	0.87 ± 1.1
Adaptive+Correction	6.5 ± 2.7	0.72 ± 1.1

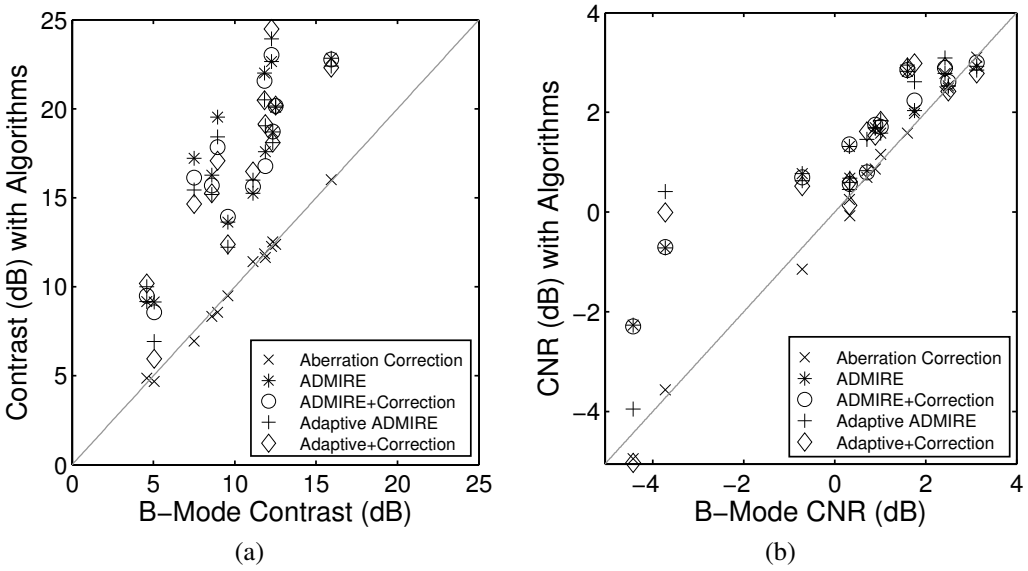

(a) (b)

Figure 4.13: Contrast and contrast-to-noise ratio (CNR) with algorithms are plotted as a function of contrast and CNR of the normal B-mode image. There are 13 contrast and CNR measurements obtained from each algorithm.
(a) Contrast, (b) CNR

4.4 Discussion and Conclusions

Here we considered the role of model-based methods in the presence of aberration. The results show that ADMIRE only preserves phase aberration when the degrees of freedom are high. To make the model more parsimonious in the presence of aberration, we introduced adaptive ADMIRE.

Simulations that included both multipath scattering and phase aberration showed multipath scattering distorts estimates of wavefront aberration, as illustrated in Fig. 4.2. Specifically, aberration levels in the presence of clutter are estimated to be higher than the simulated level of aberration.

We then evaluated ADMIRE and adaptive ADMIRE performance *in vivo*, quantifying aberration profiles. The results, as shown in Figs. 4.7 and 4.8, highlight a shortcoming of conventional filters and demonstrate the potential role of adaptive ADMIRE for better charactering aberrated wavefronts when there is little prior knowledge of the degree of

wavefront distortion. These *in vivo* data results are restricted to abdominal imaging and are consistent with related literature [120], and it is known that levels of aberration are different in other scenarios like breast imaging and echocardiography. Additionally, in this study we applied aberration estimation and correction methods that are simple and basic with fundamental limitations [124]. It is possible that more sophisticated algorithms may yield better results.

As stated above, adaptive ADMIRE has two major aims. The first aim is to establish a tool to test the best way to address aberration, while the second aim is to effectively differentiate aberrated signals of interest from other forms of clutter, and these aberrations are well addressed by aberration correction methods. Based on the findings from simulations, adaptive ADMIRE shows an ability to preserve aberration while decluttering. For instance, results in Fig. 4.4 and Fig. 4.5 demonstrate that adaptive ADMIRE can reproduce original aberrated wavefronts with very low degrees of freedom, compared to ADMIRE. Fig. 4.6 also reveals that adaptive ADMIRE can identify phase aberration effects in the presence of clutter and aberration. These results indicate that adaptive ADMIRE may be useful to accomplish the second aim. However, to increase performance, adaptive ADMIRE should be implemented with a suitable spatial filter. One possible explanation for the benefit seen by ADMIRE and adaptive ADMIRE is the reduction of aberrator integration error after reconstruction.

Finally, we briefly examined the role that ADMIRE and adaptive ADMIRE play on image quality in the presence of wavefront aberration. The results in Figs. 4.8 and 4.10 suggest that ADMIRE plus aberration correction does not provide any additional improvement, but that use of adaptive ADMIRE followed by conventional aberration estimation and correction methods could be the best way to address aberration effects when targets are at the focus. The suggested approach may be more effective in higher aberrated environments, as indicated in Fig. 4.8 with FWHM = 2.5 mm, RMS = 50 ns and FWHM = 5 mm, RMS = 50 ns. The findings are also indicated in the speckle-based target simulation results

demonstrated in Fig. 4.10. While the image quality metrics show that contrast in images obtained from ADMIRE with and without correction is similar to the image contrast from adaptive ADMIRE plus correction, but the ADMIRE CNR values are lower than those of adaptive ADMIRE plus correction. A possible explanation for this may be that we selected low degrees of freedom when implementing ADMIRE with model-mismatch due to local sound speed variation (i.e., phase aberration). ADMIRE with higher degrees of freedom loses contrast but increases CNR. The *in vivo* results (Fig. 4.13) are consistent with those of simulations because most of the features of interest *in vivo* images may be outside of the transmit focus' depth of field, but in some cases adaptive ADMIRE plus correction improves contrast and CNR compared to adaptive ADMIRE. The image quality results also demonstrate that ADMIRE by itself suppresses phase aberration effects along with clutter, providing benefits to image quality compared to conventional methods.

Chapter 5

MODEL-BASED BEAMFORMING WITH PLANE WAVE SYNTHESIS IN MEDICAL ULTRASOUND

This work was originally published in [125]:

K. Dei, J. E. Tierney, and B. C. Byram, "Model-Based Beamforming with Plane Wave Synthesis in Medical Ultrasound," *Journal of Medical Imaging*, vol. 5, no. 2, p. 027001, 2018.

5.1 Introduction

Today's modern ultrasound platforms can provide high quality images *in vivo*. However, imaging artifacts still impair the effectiveness of ultrasound in medicine. To minimize such artifacts, numerous beamformers have been introduced [81, 126, 84, 66]. Aperture domain model image reconstruction (ADMIRE) is one such beamformer that uses a physical model of aperture domain signals, developed by our group [41, 69].

In previous studies, we demonstrated that ADMIRE has the ability to suppresses reverberation artifacts, off-axis clutter and wavefront aberration from *in vivo* B-mode data [69, 101]. ADMIRE also addresses limitations of related beamforming methods because it preserves post-processed channel signals and preserves speckle texture and statistics of normal B-mode. Additionally, the clutter reduction does not impact resolution as other traditional clutter suppression methods like apodization do [102]. Based on these findings, we have established that ADMIRE is an effective tool to reduce artifacts in ultrasound images.

We previously used conventionally focused beam sequences and concentrated on reducing imaging artifacts caused by reverberation. However, because ADMIRE also showed robustness to suppress off-axis clutter in Chapter 3, we were interested in how ADMIRE performs on images obtained from unfocused beams used to insonify a broad field of view.

As reported in the literature, unfocused beam sequences provide lower resolution and lower contrast images compared to focused beams, due to transmit beam broadening [127]. We hypothesize that ADMIRE may be useful to restore image degradation resulting from broad field insonification.

Two common types of waves that allow a single transmit beam to acquire an entire field of view are plane waves and diverging waves [128, 129]. Plane wave sequences have been used in medical ultrasound to obtain higher frame rates, compared to conventional focused beam sequences, especially when imaging non-stationary objects (e.g., dynamic elastography and blood flow imaging [130]). Given the recent interest in using unfocused, full field insonification sequences for high-speed imaging, we explored ADMIRE's potential to suppress clutter resulting from plane wave sequences. [131]. In order to compensate for loss of image quality, while maintaining high frame rates, these sequences often involve the acquisition of plane waves at multiple angles that are then coherently summed to synthesize continuous transmit focusing, a method that we have not evaluated in conjunction with ADMIRE.

The objective of this study is to evaluate the performance of ADMIRE in conjunction with plane wave transmit sequencing and synthetic aperture focusing using simulation, phantom, and *in vivo* data. Because ADMIRE is a nonlinear processing method, we also examine the effect of applying ADMIRE either before or after synthetic aperture focusing on 3 and 11 steered plane waves. We also demonstrate the impact of random noise on the ADMIRE model decomposition and reconstruction. Finally, we identified some limitations of using a conventional software envelope detection method so we demonstrate the benefits of an alternative envelope detector.

5.2 Methods

5.2.1 Simulated and Experimental Data

To conduct this study, we utilized both contrast and resolution phantom data obtained using single and multiple steered plane waves. The base phantom datasets were prepared and distributed for the Plane-wave Imaging Challenge in Medical UltraSound (PICMUS), which was a competitive event using common data, independently organized during the 2016 IEEE International Ultrasonic Symposium [132, 133]. The dataset consists of two sets of phantom data used for evaluating ADMIRE, including 1) simulated phantoms generated using Field II simulation [17, 18], and 2) tissue-mimicking phantom data acquired using a Verasonics ultrasound system (Verasonics Inc., Kirkland, WA, USA) with a linear array transducer (L11-4v). Field II simulation details are indicated in Table 5.1, while Table 5.2 identifies parameters used to acquire RF channel data on the Verasonics platform.

Table 5.1: Field II Simulation Parameters

Parameters	**Values**
Number of elements	128
Width of elements	0.27 mm
Height of elements	5.00 mm
Pitch	0.30 mm
Aperture length	38.4 mm
Center frequency (f_c)	5.208 MHz
Sampling frequency (f_s)	20.832 MHz
Bandwidth	35%
Transmitted pulse	2.5 cycles
f-number	1.75

Table 5.2: L11-4v Linear Probe Setting

Parameters	**Values**
Number of elements	128
Width of elements	0.27 mm
Height of elements	5.00 mm
Pitch	0.30 mm
Aperture length	38.4 mm
Center frequency (f_c)	5.208 MHz
Sampling frequency (f_s)	20.832 MHz
Bandwidth	35%
Transmitted voltage	30 V
Transmitted pulse	2.5 cycles
f-number	1.75

5.2.2 ADMIRE Algorithm and Parameters

In the implementation of ADMIRE, a design matrix of model predictors is constructed using the physical model in (2.1), while we apply the Fourier Transform (FT) to delayed

channel signals at a small range of depths to convert into the frequency domain, as follows.

$$s_i(mT) \xrightarrow{\mathscr{F}} S_i(mT, \omega_p), \tag{5.1}$$

where i indexes channel element, mT is the discrete time index, T is the sampling time period of the channel data, ω_p is a discrete frequency, $s_i(mT)$ is delayed channel signal for channel element i at the discrete time mT, $S_i(mT, \omega_p)$ is the FT signal for a single channel of the aperture i, and $\xrightarrow{\mathscr{F}}$ is the FT operator. We then express a single frequency of the aperture domain signal at a given depth, denoted as y, in the following linear model.

$$y = X\beta, \tag{5.2}$$

where X is the ADMIRE design matrix (i.e., the matrix of predictors) corresponding to a given depth and frequency and constructed from the physical model in (2.1), and β is the coefficient vector for the predictors in X. y, X and β are initially complex: $y \in \mathbb{C}^{\mathbb{M}\times\mathbb{1}}$, $X \in \mathbb{C}^{\mathbb{M}\times\mathbb{N}}$, $\beta \in \mathbb{C}^{\mathbb{N}\times\mathbb{1}}$, where $\mathbb{M}$ is the number of aperture elements and $\mathbb{N}$ is the total number of model predictors, but most efficient solvers only allow real inputs (e.g., code by Friedman *et al.* [134]) so y and X are then expressed with the following matrices, decomposing complex signals into real ($\Re$) and imaginary ($\Im$) components, respectively,

$$y = \Big[\Re\{S_i(mT, \omega_p)\}\ \Im\{S_i(mT, \omega_p)\}\Big]^\top, \tag{5.2a}$$

$$X = \begin{bmatrix} \Re\{p_{s_n}(x;t,\omega)\}^\top & -\Im\{p_{s_n}(x;t,\omega)\}^\top \\ \Im\{p_{s_n}(x;t,\omega)\}^\top & \Re\{p_{s_n}(x;t,\omega)\}^\top \end{bmatrix}, \tag{5.2b}$$

where $\top$ denotes the non-conjugate matrix transpose. The β vector is also adjusted accordingly.

The solution of the linear model in (5.2) is ill-posed. In order to solve the ill-posed inverse problem in (5.2), we perform model decomposition (i.e., model-fitting) using elastic-

net regularization that linearly combine L1 and L2 penalties [86], given by

$$\hat{\beta} = \min_{\beta}(\|y - X\beta\|^2 + \lambda(\alpha\|\beta\|_1 + (1-\alpha)\|\beta\|_2^2/2)), \tag{5.3}$$

where $\|\beta\|_1$ and $\|\beta\|_2$ denote the L1 and L2 norms, respectively, and α and λ terms control the degree and type of regularization. For example, the parameter of α ranges between 0 and 1 to adjust the relative weight of L1 and L2, while the degrees of freedom (df) is a function of λ, as addressed by Tibshirani *et al.* [87].

Because the model decomposition process in ADMIRE reproduces a given wavefront using model predictors, we can identify the spatial location of the decomposed signal within the field of view. Based on the information, we select only energy inside the region of interest and remove scatterers outside this region. In short, model predictors from within the acceptance zone are reconstructed to reproduce the signal of interest (SOI) while rejecting other model predictors. We refer to the reconstructed signals as decluttered signals, given in the following form.

$$y_{SOI} = X_{ROI}\hat{\beta}_{ROI}, \tag{5.4}$$

where y_{SOI} is a decluttered signal, X_{ROI} is the model with predictors that are spatially within the acceptance zone that is accounted for in the region of interest (ROI) and $\hat{\beta}_{ROI}$ is the corresponding model coefficients. When implementing ADMIRE, the acceptance zone is specified as an ellipse, based on the expected lateral and axial resolutions [69] of res_{lat} and res_{axl}, respectively, given by

$$\left(\frac{x_n - x_r}{c_{lat}res_{lat}}\right)^2 + \left(\frac{z_n - z_r}{c_{axl}res_{axl}}\right)^2 \leq 1, \tag{5.5}$$

where x_r and z_r denote the center of the acceptance zone, and c_{lat} and c_{axl} are scalable factors for the acceptance region laterally and axially, respectively. The post-ADMIRE decluttered signals in (5.4) are converted back into the time-domain using the inverse short-

time Fourier Transform (ISTFT) [89].

When applying the ADMIRE algorithm to a specific transmit beam sequencing, two major factors substantially impact performance. One is the spatial sampling of the predictors used to create X in (5.2), while the other is the elastic-net regularization parameters (α and λ) in (5.3). In our previous *in vivo* study using ADMIRE, the model space was finely sampled within the acceptance zone and coarsely sampled outside the region (i.e., the rejection zone) for all depths shallow to the acceptance zone, in order to effectively suppress reverberation artifacts. However, assuming that reverberation will not be a substantial source of degradation in this study, ADMIRE was implemented with the model space confined to the depth around the acceptance zone, allowing the algorithm to focus on off-axis clutter reduction. In this study, we tuned the model space sampling and regularization parameters specifically for each number of summed plane waves. Unless stated, we apply synthetic plane wave focusing before applying ADMIRE [135]. Table 5.3 indicates ADMIRE parameters used in this study.

Table 5.3: ADMIRE Parameters

Parameter	Value
α	0.9
λ	tunable variable
c_{lat}	6
c_{axl}	2
Model space (lateral) [m]	aperture length
Model space (axial) [m]	$z_r \pm (c_{axl} res_{axl})/2$
Model sampling (inside) [m]	$\{0.0716 res_{lat},\ 0.286 res_{axl}\}$
Model sampling (outside) [m]	$\{1.43 res_{lat},\ 1.43 res_{axl}\}$
STFT window size	(8log(2))/(2πBWf_c)

BW is the fractional bandwidth and
f_c is the center frequency of transmitted pulse.

Synthetic focusing is the process whereby the received signals of individual aperture elements are synthetically focused and used to reconstruct images [136, 23, 15]. When using this method, a transmitted pulse can insonify an entire field of interest and the received signals from each transmit pulse are collected and processed to form a B-mode image that

is typically a low resolution image. The resulting sets of low resolution data are coherently summed, providing a high resolution image with dynamic transmit focusing throughout the field of view. The resulting images, after summing data from each steered plane wave image, have high resolution and high contrast compared to a single plane wave image.

5.2.3 ADMIRE Computational Complexity

Compared to delay-and-sum (DAS) beamforming, ADMIRE has additional steps to implement, including the STFT operation, model decomposition, reconstruction, and the inverse-STFT as described previously. These all increase the computational complexity. First, a computational order of $\mathcal{O}(pqr \log q)$ is introduced for the STFT operation, where p is the number of channels, q is the number of samples in each short-time window and r is the total number of windows through depth. Next, model decomposition with an elastic-net regularization technique has a computational cost of $\mathcal{O}(u^3 + u^2 v)$, where u is the number of model predictors actually used in the fit and v is the total number of model predictors in the ADMIRE design matrix X in (5.2b) [86, 69]. This has to be done for every depth and frequency. A computational order of reconstruction is $\mathcal{O}(u)$ times number of depths. Lastly, the inverse STFT has a computational complexity of $\mathcal{O}(r + qr \log q)$ [89]. In summary, when implementing ADMIRE beamforming, the additional computational cost beyond normal DAS beamforming is $\mathcal{O}(r + r(u^3 + u^2 v)w + ru + pqr \log q + qr \log q)$, where w is the number of frequencies used in the model decomposition.

5.2.4 Image Quality Assessment

In order to evaluate ADMIRE's performance, we selected images formed from 1 plane wave and multiple steered plane waves (3, 11, 31 and 75) [135]. We compare results using image quality metrics for anechoic cyst phantom images derived from DAS and ADMIRE. We measured contrast and contrast-to-noise ratio (CNR) using

$$C = -20\log 10(\frac{\mu_L}{\mu_B}), \tag{5.6}$$

$$CNR = 20\log 10(\frac{|\mu_L - \mu_B|}{\sqrt{\sigma_L^2 + \sigma_B^2}}), \tag{5.7}$$

where (μ_L, σ_L^2) and (μ_B, σ_B^2) denote the value of the mean and variance of the enveloped but uncompressed image inside and outside the anechoic structures, respectively. These metrics differ from those chosen by the PICMUS challenge committee [132, 133]. We also compared the point spread functions of resolution target phantoms reconstructed from 1 and 75 steered plane waves, along with linear scan cases having 3 or 4 cm transmit foci. (Note that 75 steered plane waves represent the full set of plane waves acquired.) The linear scan data were not part of the PICMUS challenge. Each set of point spread functions were created using DAS with rectangular window, DAS with Hann apodization, ADMIRE with rectangular window and ADMIRE with Hann apodization on receive.

Apart from the above, it is worth noting that the processing in ADMIRE is nonlinear so that it is important to evaluate two different sequences— i) processing synthetic aperture first, and then applying ADMIRE, and ii) the application of ADMIRE followed by synthetic aperture focusing. Based on this, we investigated ADMIRE images formed by both sequences. We used 3 and 11 steered plane waves with an increment of 0.43°. We qualitatively compared resulting images for 3 and 11 steered plane wave cases with ADMIRE, as well as synthetic aperture focusing only (i.e., DAS). We also quantified the axially integrated power to determine which sequence may be more effective to suppress off-axis energy when applying ADMIRE.

5.2.5 *In Vivo* Evaluation

We applied ADMIRE to *in vivo* carotid artery data, which was also provided by the PICMUS competition as additional data [132, 133]. The dataset includes *in vivo* carotid artery

data collected using the same parameters as indicated in Table 5.2. Data were acquired in the cross section of a carotid artery. We used the same evaluation metrics as described in 5.2.4. We generated DAS B-mode images using single plane wave and multiple steered plane waves (3, 11 and 75) with synthetic aperture focusing. We applied ADMIRE to the data to reconstruct ADMIRE B-mode images.

5.2.6 Evaluation with Additive Random Noise

We also investigated the effects on plane wave image quality when applying ADMIRE in the presence of uncorrelated noise. We used simulated cyst phantom data from the PICMUS using 75 steered plane waves. We then added white Gaussian noise to the channel data with signal-to-noise ratio (SNR) between -20 dB and 60 dB with an increment of 10 dB SNR. We reconstructed B-mode images after applying DAS and ADMIRE, respectively, to compute contrast and CNR using (5.6) and (5.7), respectively.

5.2.7 Proposed Envelope Detection Method

In evaluating post-ADMIRE decluttered signals, we identified limitations associated with the conventional envelope detection method based on the Hilbert transform. In order to minimize the limitations, we implemented envelope detection using an optimum equiripple finite impulse response (FIR) Hilbert filter based on the Parks-McClellan algorithm [137, 138] followed by a fifth-order low-pass Butterworth filter (i.e., IIR LP filter). We examined the effect of using the FIR Hilbert envelope detection when applying DAS and ADMIRE in the presence of various levels of added random noise. Fig. 5.1 illustrates the block diagram of the proposed envelope detection method, which is referred to as FIR Hilbert filter.

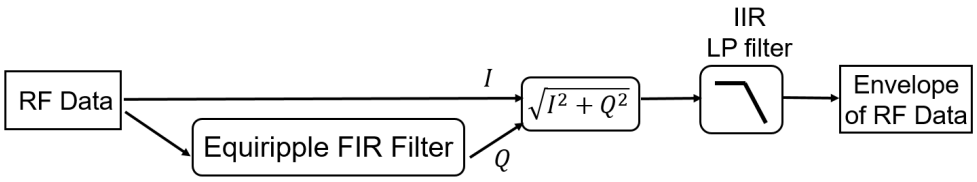

Figure 5.1: The block diagram of the proposed envelope detection method, referred to as the finite impulse response (FIR) Hilbert filter, to fully realize the benefits obtained from using ADMIRE.

5.2.8 Speckle Signal-to-Noise Ratio Measurements

Finally, we compare speckle patterns obtained from ADMIRE to focused and unfocused plane wave sequences. To test this, we simulated and compared a simulated homogeneous phantom with sufficient scatterer density to ensure fully developed speckle [103]. We used Field II simulation [18] with parameters indicated in Table 5.1. In the first case, conventional transmit beam sequences with focal depth of 5 cm were used, while the second case used unfocused beam sequences with 75 steered plane waves synthetically combined. We then applied ADMIRE to each of these two sets of speckle data. Finally, we measured the speckle signal-to-noise ratio (SNR$_{speckle}$) of each case as a function of depth, using

$$SNR_{\text{speckle}} = \frac{\mu_B}{\sigma_B}, \tag{5.8}$$

where (μ_B, σ_B^2) are the same denotation in (5.6) and (5.7). When computing the values of SNR$_{speckle}$, rectangular kernels were applied with 5 mm height and 25 mm width with 98 % overlap.

5.3 Results

Fig. 5.2 demonstrates two sets of different phantom images reconstructed after applying ADMIRE. The first set of results was generated with parameters tuned for focused transmit beams but applied to plane wave sequences, while the second set is with parame-

ters tuned specifically for a single plane wave image sequence. Comparing the two sets of ADMIRE images using different tuning parameters, it is apparent that optimally tuned parameters for a specific sequence substantially impact ADMIRE performance in recovering and improving image quality while preserving speckle statistics.

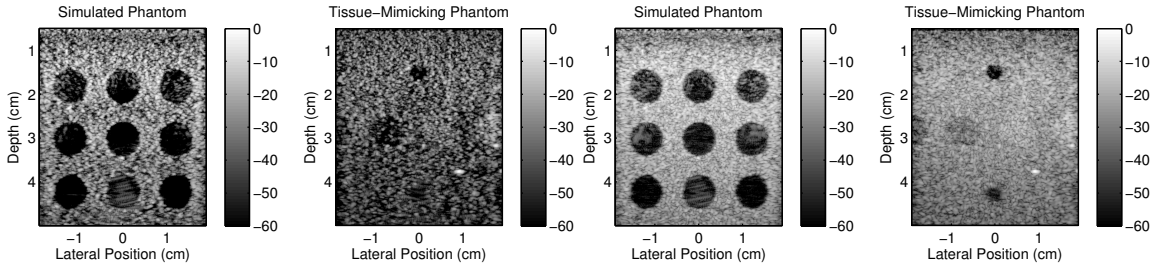

Figure 5.2: Two sets of single plane wave B-mode images of cyst phantoms (simulated (left), tissue-mimicking (right)), obtained from ADMIRE with (a) previously tuned parameters for focused transmit beam sequences and (b) tuning specifically for plane wave imaging.

Fig. 5.3 shows B-mode images of contrast cyst phantoms after applying DAS and ADMIRE beamforming, obtained from 1, 11 and 75 steered plane waves. The 11 and 75 plane wave images were formed after synthetic aperture focusing followed by DAS and ADMIRE. The results of contrast and CNR measurements for these cases (simulated and tissue-mimicking cyst phantoms) including 1, 3, 11, 31 and 75 steered plane waves are plotted as a function of number of steered plane waves in Fig. 5.4. The results of the ADMIRE algorithm are based on parameters tuned for plane wave transmit sequences. These findings suggest that ADMIRE provides a boost to plane wave image quality compared with conventional DAS beamforming. It is also noticeable that improvements in contrast and CNR increase until the number of plane waves reads 11 for both DAS and ADMIRE cases, but after 11 steered plane waves the contrast and CNR values converge.

Next, in Fig. 5.5, we present the outcome of ADMIRE's performance using resolution target phantom simulations with a point target at 3 cm depth on axis. The figure includes sets of 2-D, axially integrated 1-D lateral and 1-D axial point spread functions

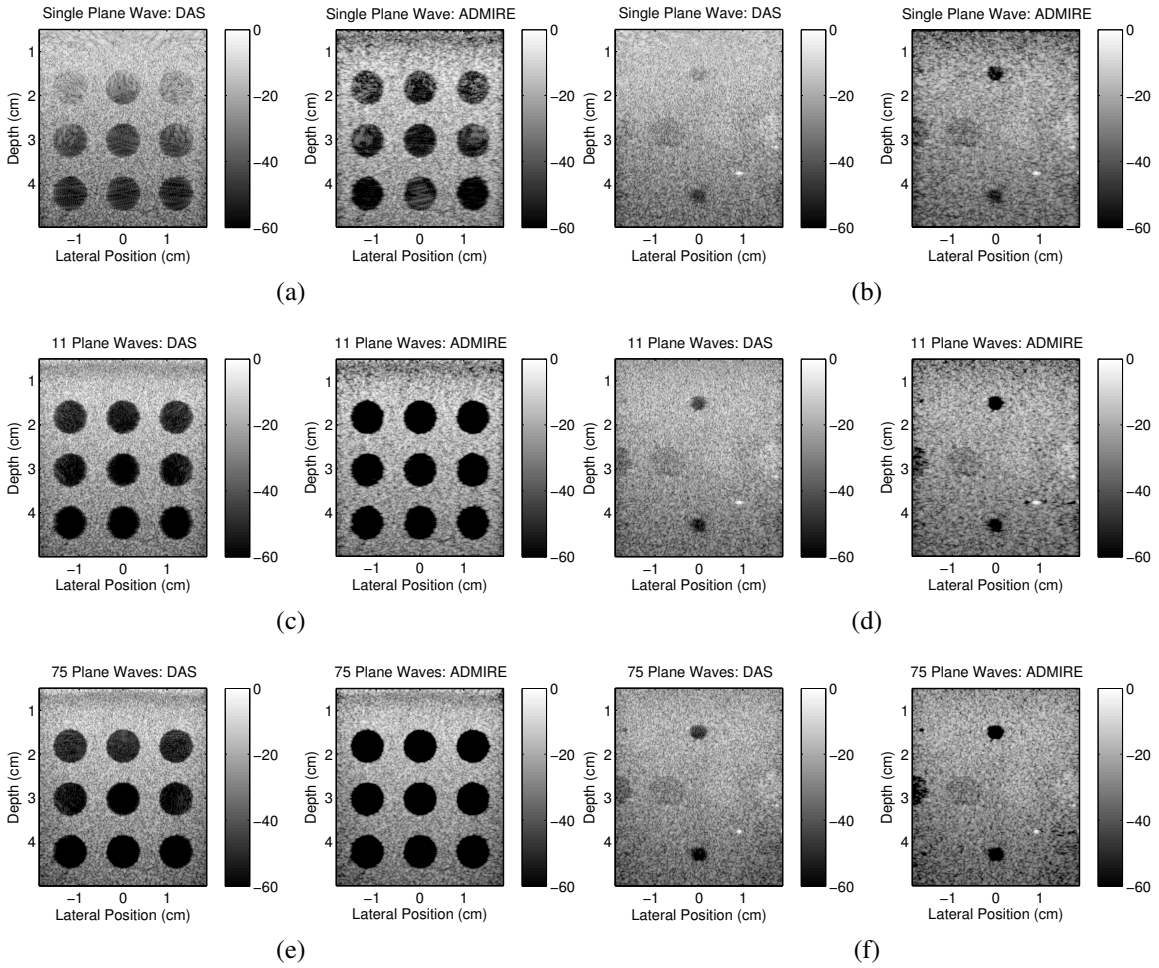

Figure 5.3: Plane wave images formed after applying DAS and ADMIRE, using simulated anechoic cyst phantom (left) and tissue-mimicking phantom (right). Sets of images: (a)-(b), (c)-(d), and (e)-(f) were formed from 1, 11 and 75 steered plane waves with synthetic aperture focusing, respectively.

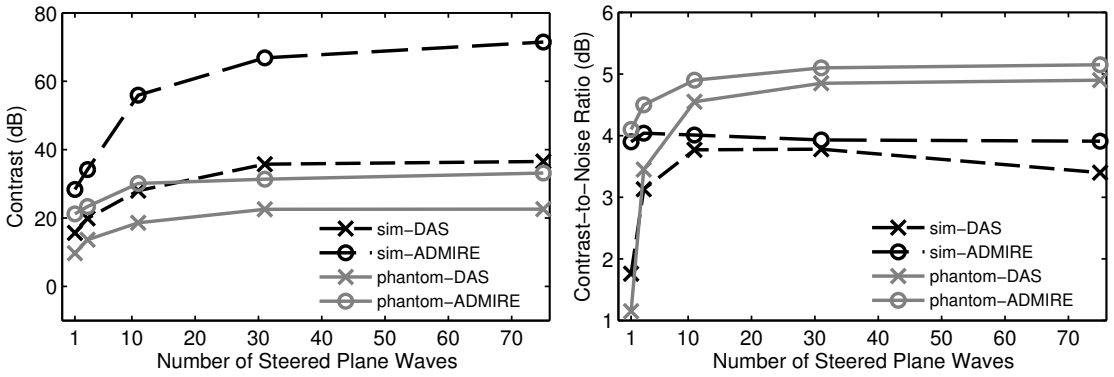

(a) (b)

Figure 5.4: Plot of (a) contrast and (b) CNR measurements for simulated and tissue-mimicking cyst phantoms as a function of number of steered plane waves. The contrast and CNR values are quantified from DAS and ADMIRE B-mode images obtained using 1, 3, 11, 31 and 75 steered plane waves.

derived from applying DAS and ADMIRE with and without Hann apodization. The point spread functions show that ADMIRE significantly reduces side-lobes compared with DAS after applying Hann apodization while preserving the spatial resolution of DAS without apodized beams. It is also interesting to note that Hann apodization after ADMIRE provides further side-lobe reduction; although, this also results in the expected loss of lateral resolution. Note that post-ADMIRE reconstructed images and lateral beam profiles show asymmetries due to the fact that the model matrix, X in (5.2), used in these cases was not constructed symmetrically.

Fig. 5.6 illustrates resolution phantom images obtained from 3 and 11 steered plane waves with synthetic aperture focusing and ADMIRE images formed by two different sequences, along with lateral beam (i.e., axially integrated power) profiles for each case. The results suggest that despite the nonlinear aspect of ADMIRE there is little difference from the order of operation for 3 steered plane waves. In using 11 steered plane waves, however, the application of ADMIRE after synthetic aperture processing is more beneficial than use of ADMIRE before synthetic aperture processing, as shown in Fig. 5.6 (g).

Fig. 5.7 provides *in vivo* carotid artery plane wave images derived from using DAS

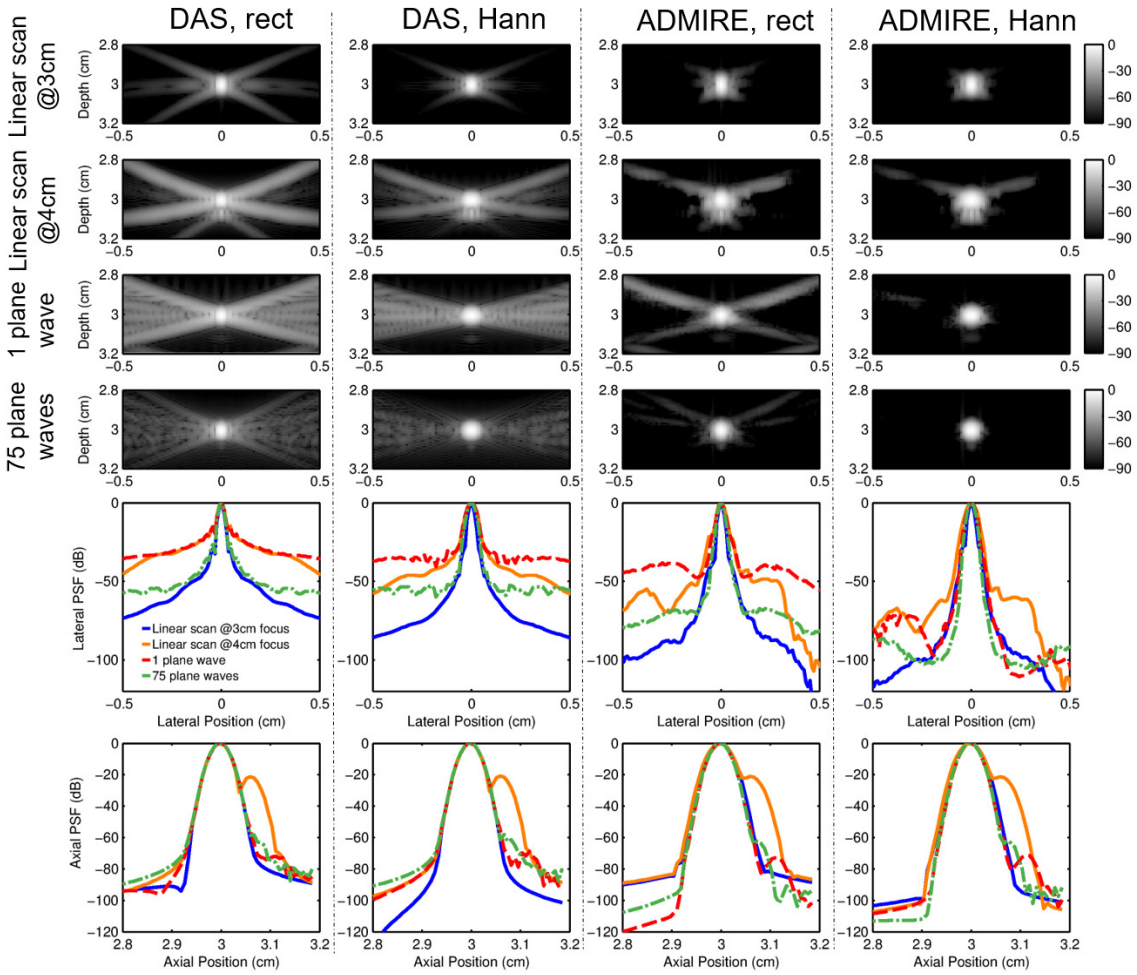

Figure 5.5: ADMIRE assessment using simulated resolution phantoms with a point target 3 cm deep and on-axis, using 1 and 75 steered plane wave(s) acquisition sequences, along with linear scan acquisitions having 3 or 4 cm transmit foci. Sets of 2-D and axially integrated 1-D lateral and 1-D axial point spread functions are demonstrated. Each set of point spread functions was simulated after applying DAS with rectangular window, DAS with Hann apodization, ADMIRE with rectangular window and ADMIRE with Hann apodization.

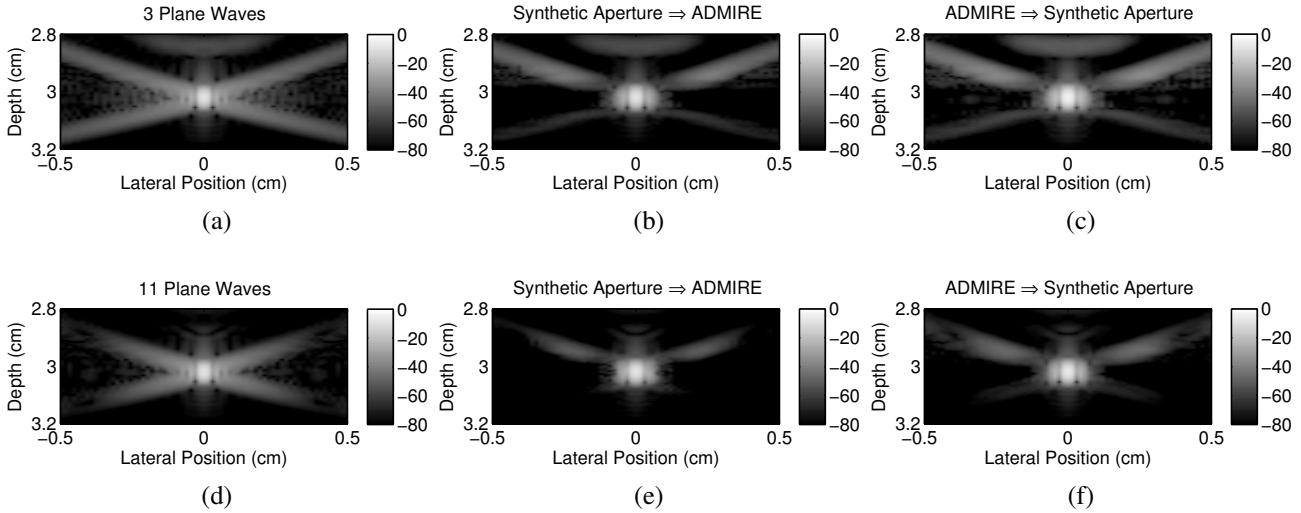

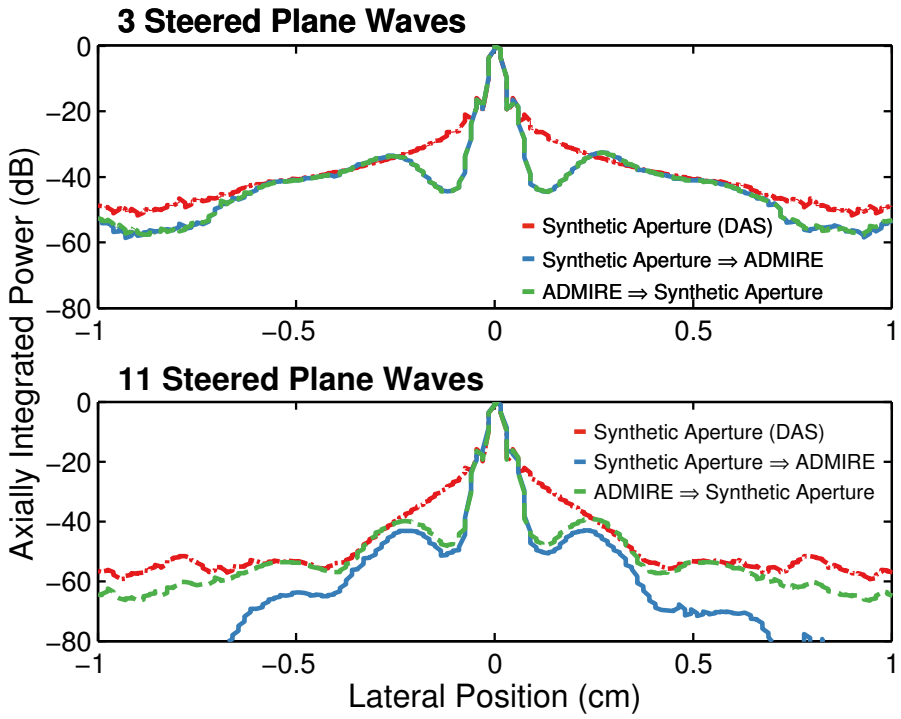

(g)

Figure 5.6: Simulated resolution phantom images obtained from 3 and 11 steered plane waves applying synthetic aperture focusing (DAS), and ADMIRE images with two different sequences: (a) and (d) DAS B-mode images formed after synthetic aperture, (b) and (e) ADMIRE B-mode images obtained with synthetic aperture to ADMIRE sequence, (c) and (f) ADMIRE B-mode images derived from applying ADMIRE followed by synthetic focusing. The corresponding lateral beam (i.e., axially integrated power) profiles are demonstrated for two sets of plane wave acquisition in (g).

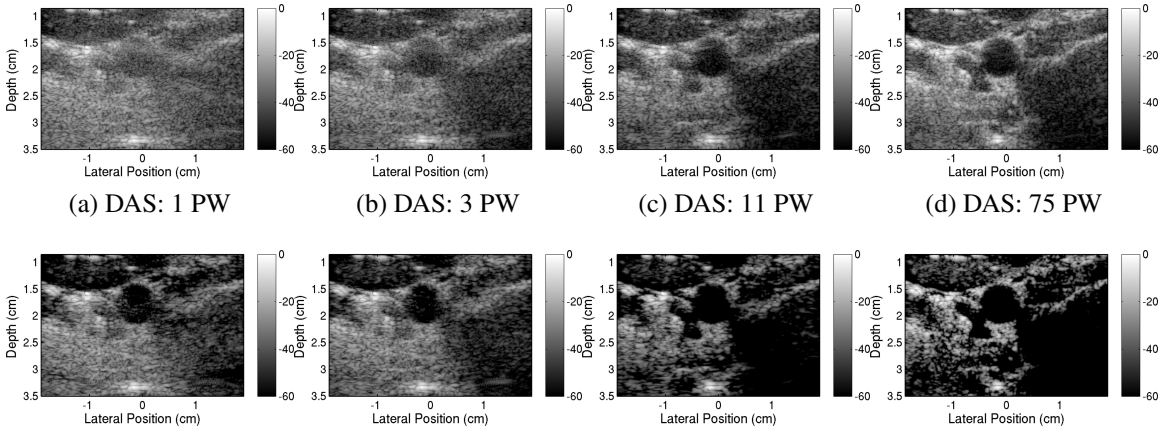

(a) DAS: 1 PW (b) DAS: 3 PW (c) DAS: 11 PW (d) DAS: 75 PW

(e) ADMIRE: 1 PW (f) ADMIRE: 3 PW (g) ADMIRE: 11 PW (h) ADMIRE: 75 PW

Figure 5.7: *in vivo* carotid artery cross-sectional images are demonstrated. The images were obtained from 1, 3, 11 and 75 steered plane waves from left to right. The images on top, (a)-(d) were formed from synthetic aperture focusing only (DAS), while the images below, (e)-(h) were derived using ADMIRE after synthetic aperture focusing.

(top) and ADMIRE (bottom). Images were formed using 1, 3, 11 and 75 steered plane waves. When compared to DAS and ADMIRE B-mode images, we observe qualitative improvements with ADMIRE based on improved anatomical detail. We also evaluated the resulting *in vivo* images quantitatively, using image quality metrics. Table 5.4 reports the results of contrast and CNR measured from the *in vivo* B-mode data, indicating consistency of qualitative measures in Fig. 5.7. Although, for the high plane wave count sets the CNR drops for both ADMIRE and DAS. Part of the challenge seems to be that it is difficult to find a uniform background region for calculating the image metrics.

Fig. 5.8 presents B-modes images of simulated cyst phantoms with added white Gaussian noise, and with varying degrees of channel data SNR between -20 and 30 dB with an

Table 5.4: Results of *In Vivo* Contrast and CNR Measurements

Number of Plane Waves	**1**		**3**		**11**		**75**	
Algorithm	DAS	ADMIRE	DAS	ADMIRE	DAS	ADMIRE	DAS	ADMIRE
Contrast [dB]	10.06	28.43	15.48	28.46	20.27	42.84	23.87	47.38
CNR [dB]	-0.51	2.02	0.60	1.60	0.61	0.10	-1.39	-2.73

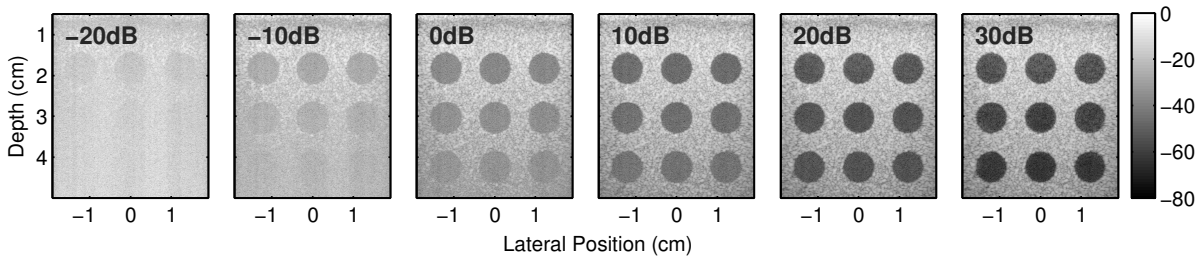

(a) DAS

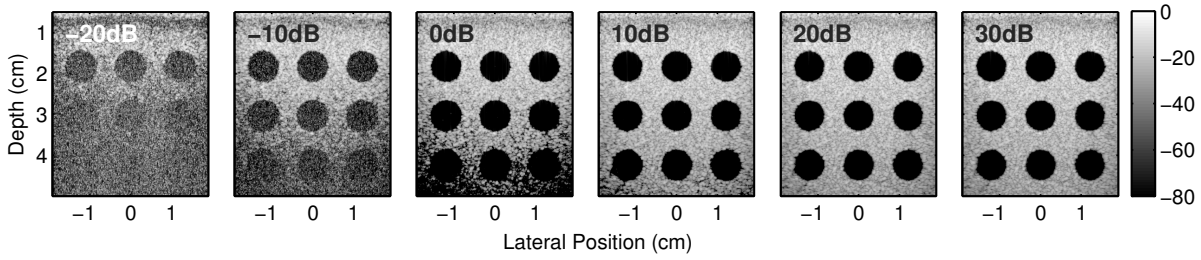

(b) ADMIRE

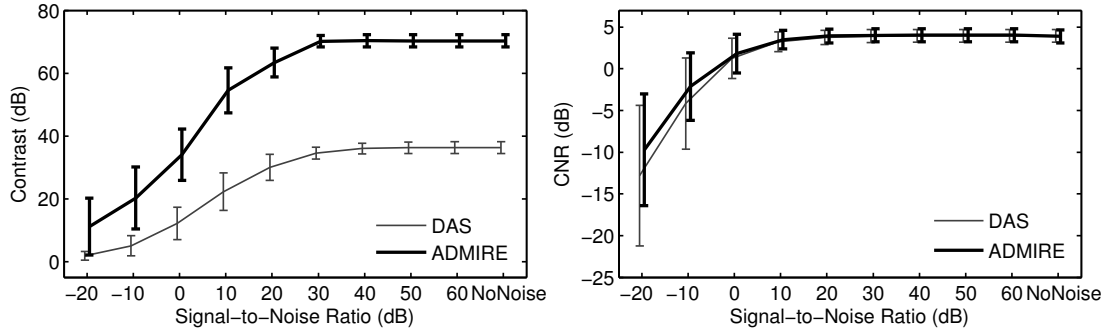

(c) Image Quality Metrics

Figure 5.8: B-modes images of simulated cyst phantoms with added white Gaussian noise with channel data SNR between -20 and 30 dB with an increment of 10 dB SNR, quantified using image quality metrics with additional channel SNR 40, 50, 60 dB plus no noise case. The reconstructed images were obtained from (a) DAS and (b) ADMIRE, along with contrast and contrast-to-noise (CNR) as a function of channel SNRs in (c).

increment of 10 dB SNR. The images in Fig. 5.8 (a) were obtained from DAS, while the images in Fig. 5.8 (b) were formed after applying ADMIRE. We also quantified the data using image quality metrics with additional channel data SNR of 40, 50, 60 dB plus no noise in Fig. 5.8 (c). Unsurprisingly, the results demonstrate that ADMIRE always outperforms DAS in contrast, but it is important to note that the improvements are reduced in high noise scenarios. For example, with an SNR -20 dB, the improvements are at least 10 dB higher in contrast, but with an SNR 10 dB or greater the improvements are over 30 dB in contrast. It can thus be suggested that the improvement gained from applying ADMIRE is better with low noise. There is no substantial improvement in CNR when applying ADMIRE over the range of SNR. It is interesting to note that neither method approaches the theoretical limit of CNR in the presence of fully developed speckle, which is 5.6 dB.

Because we identified limitations associated with the conventional software envelope detection method using the Hilbert transform, we implemented and evaluated our proposed envelope detection method using a FIR Hilbert filter. We also investigated whether the proposed envelope detector impacts the outcome of standard DAS. Fig. 5.9 demonstrates three sets of results obtained from applying ADMIRE with no noise, also from DAS and ADMIRE in the presence of uncorrelated noise with an SNR of 30 dB. Each set of results includes comparisons of 1) envelope data using the conventional and proposed envelope detection methods, along with RF data, and 2) B-mode images using each envelope detector.

In the ADMIRE with and without noise scenario, the enveloped signals (i.e., the red Hilbert Transform lines) in Fig. 5.9 (a) and (b) show much greater amplitude than the actual amplitude of the decluttered RF signals (i.e., the blue lines), degrading image contrast after the log-compression. These findings indicate that decluttered RF signals derived from ADMIRE are degraded by the post processing of image formation. We observe better image contrast using the proposed method in Fig. 5.9 (g) and (h), compared with the images processed by the conventional method in Fig. 5.9 (d) and (e). The DAS case with

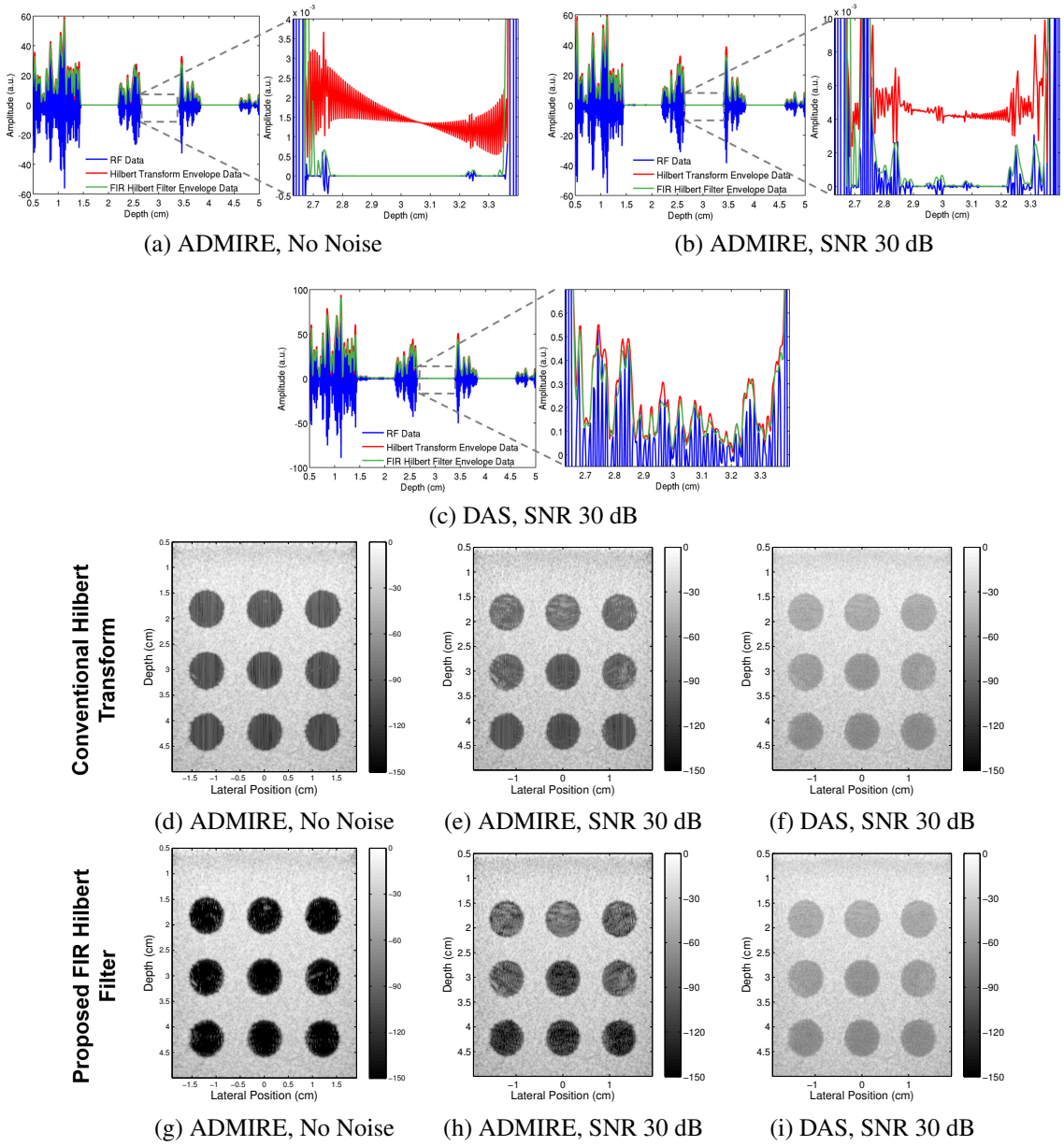

(a) ADMIRE, No Noise (b) ADMIRE, SNR 30 dB

(c) DAS, SNR 30 dB

(d) ADMIRE, No Noise (e) ADMIRE, SNR 30 dB (f) DAS, SNR 30 dB

(g) ADMIRE, No Noise (h) ADMIRE, SNR 30 dB (i) DAS, SNR 30 dB

Figure 5.9: Simulated cyst phantom data reconstructed from ADMIRE with and without noise, followed by using a conventional (Hilbert transform) and the proposed (FIR Hilbert filter) envelope detection methods, along with the matched DAS with noise. The added noise level is channel SNR 30 dB. Both methods are compared using 1) enveloped data along with RF data, 2) B-mode images that have been processed by the conventional Hilbert transform and the proposed FIR Hilbert filter envelope detectors. (Note that we filtered out the low frequency information that can cause Hilbert Transform artifacts before applying both methods.)

channel SNR 30 dB did not indicate the limitation in Fig. 5.9 (f), in comparison with Fig. 5.9 (i).

Quantitatively, we measured the contrast and CNR with respect to channel SNR, as shown in Fig. 5.10. The improvement from applying our proposed FIR filter envelope detector to post-ADMIRE decluttered signals was 7 dB in contrast when the channel data SNR is at least 30 dB or higher. There is no improvement for below 20 dB SNRs. The FIR based envelope detector did not provide any improvement at any SNR when using DAS beamforming. Based on these findings, our proposed envelope detector enables us to fully realize the benefits obtained from the ADMIRE algorithm.

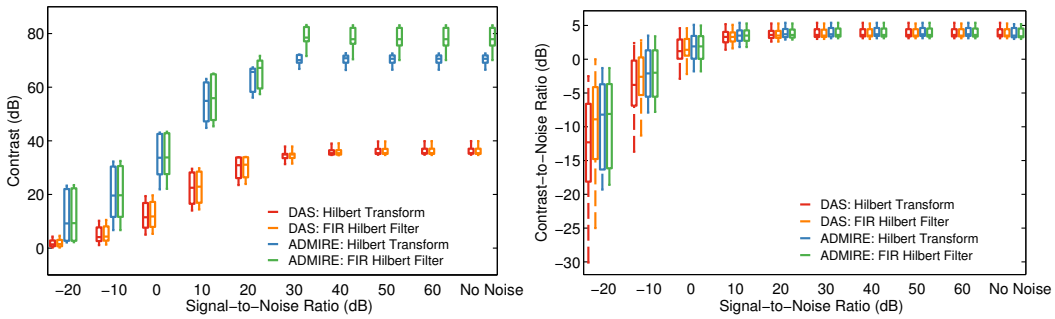

(a) (b)

Figure 5.10: Image quality metrics with respect to SNR along with no noise of DAS and ADMIRE B-mode images processed by the conventional Hilbert Transform and the proposed FIR Hilbert filter envelope detectors. (a) contrast and (b) CNR.

Fig. 5.11 presents two reconstructed speckle patterns after applying ADMIRE, each of which was simulated using Field II simulation in (a) a focused transmit beam sequence at 5 cm depth, and (b) unfocused transmit beam sequences using 75 angled plane waves followed by synthetic aperture focusing. It is interesting to note that the focused case shows that speckle texture is well recovered at a focal depth of 5 cm, but speckle patterns in the near and far fields were distorted. In contrast, the use of plane wave sequencing with synthetic aperture focusing provides a uniformly distributed speckle texture reconstructed after the application of ADMIRE. As a quantitative measure, the speckle SNR in (5.9) was computed with respect to depth in Fig. 5.10 (c), indicating that ADMIRE has the ability to

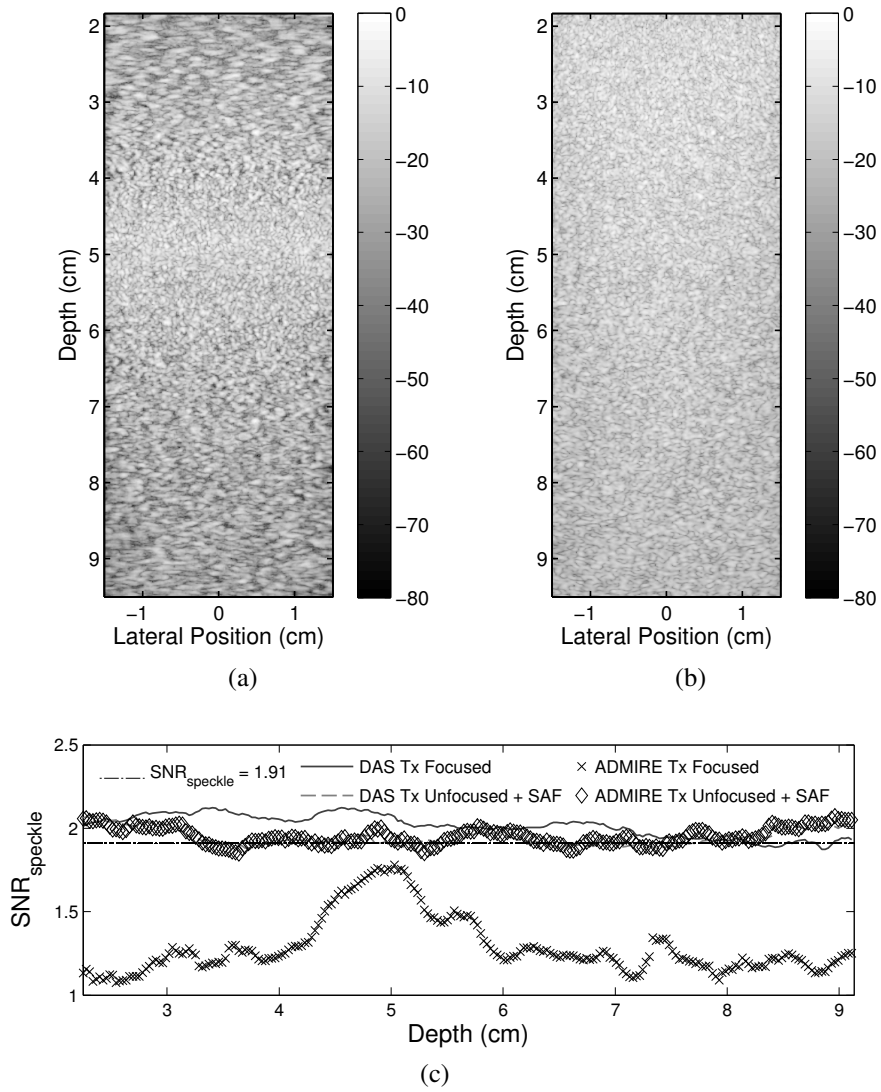

Figure 5.11: Post-ADMIRE reconstructed uniform speckles in (a) a focused transmit (Tx) beam sequence at 5 cm depth, (b) an unfocused transmit beam sequence with 75 steered angles, which are summed to synthesize transmit aperture focusing at all depths (i.e., plane wave sequence of 75 angles with an increment of 0.43°, using synthetic aperture focusing (SAF)). The speckle signal-to-noise ratios ($\mathrm{SNR}_{speckle}$) are measured and plotted as a function of depth for each acquisition in (c).

preserve the first order speckle statistics (= 1.91) over the depth of field when applied to plane wave imaging with multiple acquisition angles [139, 1]. However, ADMIRE speckle patterns obtained from focused transmit beam sequences show only high speckle SNR at and near the focal depth, while DAS provides high speckle SNR through the depth of field.

5.4 Discussion

Referring to the results in Fig. 5.4, the contrast improvements of images obtained from single and multiple steered plane waves with and without applying ADMIRE are improved by nearly a factor of 2 on a dB scale in the case of simulated cyst phantoms, while the tissue-mimicking phantom cases have over 10 dB improvement in contrast after the application of ADMIRE. In comparing CNR values, ADMIRE may provide more relative benefit when applied to images obtained using single plane waves or fewer steered plane waves. As demonstrated in Fig. 5.7, we also observed both qualitative and quantitative improvements in *in vivo* images. The findings indicate that ADMIRE improves images generated from plane wave sequences even beyond the benefits realized by synthetic aperture processing alone.

In Fig. 5.2, we demonstrated that ADMIRE must be tuned appropriately to accommodate the additional clutter encountered in plane wave sequences. It is worth noting that the results of the *in vivo* cases may improve when applying ADMIRE with a model space that also accounts for reverberation clutter. This should be considered in future work.

Using the same simulated cyst phantom data, we also investigated the impact of thermal noise (i.e., white Gaussian noise) on ADMIRE model decomposition and reconstruction. The results in Fig. 5.8 show that ADMIRE outperforms DAS. In Figs. 5.9 and 5.10, we showed that for at least some simulations with and without random noise, ADMIRE induced improvements exceed the limitations of the conventional software Hilbert transform-based envelope detector. But, as demonstrated in Fig. 5.9 (f) and (i), the DAS cases using a conventional and the proposed envelope detection methods do not show any difference.

These findings suggest that other envelope detection algorithms may be required to fully realize the benefits provided by ADMIRE or other advanced beamformers.

One major concern with respect to ADMIRE is its lengthy run-time due to its high computational complexity. The ADMIRE algorithm is "embarrassingly" parallel so GPUs or multicore CPUs will speed up performance. There are several potential approaches in related literature, such as support vector machine (SVM)-based elastic-net regularization [140] and beamforming using deep neural networks (DNN) [141] that may also speed up ADMIRE.

Finally, the results in Fig. 5.11 indicate that adaptive tuning would be necessary to preserve the speckle in other regions outside the focal depth of field, but this is not necessary when using synthetic aperture techniques. Ultimately, these findings suggest that ADMIRE performance and its outcome rely not only on selection of the tuning parameters but also on the acquisition sequence.

5.5 Conclusions

In this study, we demonstrated that ADMIRE can be adapted to full field insonification sequences. We specifically showed this using plane wave transmit sequences with and without synthetic aperture focusing. ADMIRE also shows an ability to suppress random white noise to provide a boost in thermal SNR. Finally, we demonstrated that in some cases a further improvement can be achieved by using a different envelope detector.

Chapter 6

COMPUTATIONALLY-EFFICIENT MODEL-BASED BEAMFORMING

This work is part of a manuscript submitted and in review:
K. Dei, S. Schlunk, and B. Byram, "Computationally-Efficient Implementation of Aperture Domain Model Image Reconstruction (ADMIRE)," *IEEE Transaction on Ultrasonics, Ferroelectrics, and Frequency Controls*.

6.1 Introduction

Ultrasound has been used extensively as a medical imaging modality, with an excellent safety record. It is also a real-time imaging method and is readily accessible and affordable [5]. For these reasons, ultrasound imaging is one of the most frequently used tools for diagnosis and therapeutic guidance [6, 142, 143].

However, imaging artifacts frequently encountered in clinical ultrasound are still problematic and impair its usefulness of ultrasound. These artifacts degrade ultrasound image quality, allowing a clinician to misinterpret an image and obscure diagnosis [144]. Widely reported artifacts include: i) beam-width and off-axis artifacts caused by intrinsic characteristics of acoustic waves, decreasing spatial resolution and contrast [3], ii) attenuation artifacts producing acoustic enhancement and shadowing, related to errors in attenuation of acoustic signals propagating through tissues [15], iii) speed of sound artifacts, which are related to sound speed inhomogeneity in tissue, locally distorting wavefront of propagating and scattering waves (i.e., phase aberration) [40, 42], and also producing inconsistent images with actual appearance in the presence of gross sound speed errors [39], and iv) reverberation artifacts, which occur when a transmitted signal is reflected back and forth between two interfaces during signal acquisition [145], which may severely degrade images in modern ultrasound platforms [7, 2, 41].

To mitigate such artifacts, numerous beamformers have been developed [58, 51, 81, 126, 84, 62, 146, 66], including a model-based beamformer called aperture domain model image reconstruction (ADMIRE) introduced by our group [41, 69]. Others have also recently applied these model-based methods to acoustics more generally [147, 148]. In the ADMIRE algorithm, we create a model based on the physics of wave propagation including multipath scattering. ADMIRE uses the model predictors to reconstruct decluttered images after decomposition and selection processes to identify scattering signals from the region of interest (ROI), as shown in Fig. 6.1.

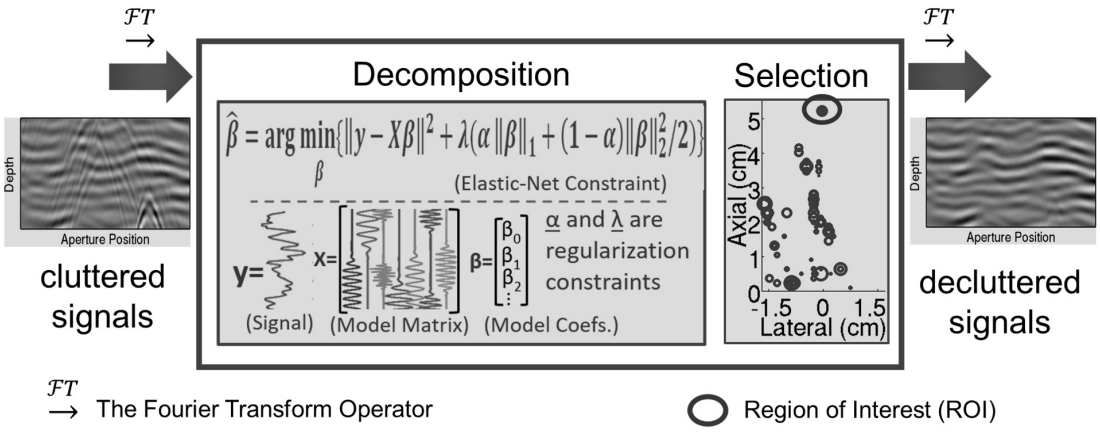

Figure 6.1: Overview of ADMIRE algorithm. When implementing ADMIRE, the signal to the left is decomposed into wavefronts scattered from within the region of interest (ROI) and unwanted signals scattered from the clutter region. After decomposition, ADMIRE then reconstructs only signals from the ROI to form the signal on the right. Both decomposition and reconstruction processes are applied to the frequency domain data at each depth.

In our previous studies, we evaluated and demonstrated the algorithm's performance and ability to mitigate ultrasound artifacts including off-axis, reverberation and phase-aberration [69, 101]. ADMIRE is also robust to sound speed deviation, minimizing the speed of sound artifacts caused by gross sound speed mismatch [90]. ADMIRE can also be adapted to full field insonification sequences (i.e., plane wave imaging) to recover image quality in challenging high clutter environments with high levels of thermal noise [125]. Based on these findings, ADMIRE is a useful tool in reducing imaging artifacts in medical ultrasound.

However, a major problem with ADMIRE is its computational complexity, which impairs its usefulness. ADMIRE has high computational requirements caused by the large model and the non-linear elastic-net regularization. The decomposition process must be repeated for every frequency per depth, further increasing the computational cost. We are interested in reduced model methods and other strategies to reduce complexity without sacrificing improvements.

Previously, we examined the role of singular value decomposition (SVD) in reducing computational complexity [149]. It was computationally more efficient using orthonormal column vectors that are linearly independent, but its performance was reduced compared to ADMIRE. In this study, we aim to conduct a more comprehensive analysis to identify the usefulness of dimensionally reduced models when implementing ADMIRE. Here, we consider other models reduced using Gram-Schmidt orthonormalization (GSO) [150, 151] and independent component analysis (ICA) [152], in comparison with images obtained using a full model or a model reduced using SVD. Furthermore, in considering other effects to accelerate ADMIRE, a simple solution may be to reduce the number of sliding window steps through depth. Similar to other beamforming methods [84, 153, 154], ADMIRE uses aperture domain signals in the frequency domain, incorporating a short-time Fourier Transform (STFT) with a 90% window overlap. Based on these findings, we also evaluate the effects of different levels of STFT window overlap on image quality and run-time. Additionally, we investigate the effect of the degrees of freedom selected during the model fit. Our ultimate goal is to enable an efficient and fast ADMIRE implementation while otherwise preserving its performance, thereby making ADMIRE more useful in real clinical applications.

6.2 Methods

6.2.1 Overview of ADMIRE

Here, we summarize several important steps in the ADMIRE algorithm, while other details are available in related literature [69, 101, 125, 90] or Chapter 2.2. The ADMIRE model matrix X is constructed using model predictors, expressed as the following matrix,

$$X = \begin{bmatrix} \Re\{p_{s_j}(x;t,\omega)\}^\top & -\Im\{p_{s_j}(x;t,\omega)\}^\top \\ \Im\{p_{s_j}(x;t,\omega)\}^\top & \Re\{p_{s_j}(x;t,\omega)\}^\top \end{bmatrix}, \tag{6.1}$$

where j indexes model space sampling, p_{s_j} is the model predictor sampled at jth model space, x is the transducer aperture location, t and ω are the time and frequency to localize the signal, $X \in \mathbb{R}^{2\mathbb{M}\times 2\mathbb{N}}$, $\mathbb{M}$ is the number of aperture elements and $\mathbb{N}$ is the total number of model predictors. The model predictor can be formulated by the location (x_n, z_n), where a signal is reflected from by delayed time τ_n, along with amplitude modulation term $A_n(x)$ across the transducer aperture [69], given by,

$$p_{s_n}(x;t,\omega) = A_n(x)e^{j\omega\tau(x;x_n,z_n,\tau_n)}. \tag{6.2}$$

Using the model matrix in (6.1), the frequency domain data at a single frequency from each depth, denoted as y in Fig. 6.1, can be expressed as a linear model, given by,

$$y = X\beta, \tag{6.3}$$

where β is the model coefficients for the real and imaginary components of the model predictors in X: $\beta \in \mathbb{R}^{2\mathbb{N}\times\mathbb{1}}$. Often, when implementing ADMIRE, the total number of model predictors is over a hundred times greater than the number of aperture elements (i.e., $\mathbb{M} < \mathbb{N}$), meaning that the solution of the linear model in (6.3) is a highly ill-posed inverse problem. To make the ill-posed problem stable, elastic-net regularization is used in model

decomposition [86], as follows.

$$\hat{\beta} = \arg\min_{\beta}(\|y - X\beta\|^2 + \lambda(\alpha\|\beta\|_1 + (1-\alpha)\|\beta\|_2^2/2)), \tag{6.4}$$

where the first term represents ordinary least squares, and the second term is the elastic-net regularization, combining the L1 norm with L2 norm, denoted as $\|\beta\|_1$ and $\|\beta\|_2$, respectively, using tunable parameters of α and λ that determine the degree and type of regularization.

The last important step is to reconstruct the signals of interest by selecting only model predictors and the corresponding coefficients within the region of interest (ROI), which is usually specified as an elliptical zone determined by the expected lateral and axial resolutions [69].

$$y_{ROI} = X_{ROI}\hat{\beta}_{ROI}, \tag{6.5}$$

where y_{ROI} is the reconstructed signal of interest, which we also call the decluttered signal, X_{ROI} is the selected model predictors and $\hat{\beta}_{ROI}$ is the corresponding coefficients. The decluttered signals in (6.5) are converted back into the original time domain using inverse short-time Fourier Transform (ISTFT) [89].

6.2.2 Model Space and Tunable Parameters

The ADMIRE model predictors in (6.2) are typically sampled from two subspaces, spatially divided into inside and outside ROI. We call the former ROI subspace, whereas the latter is referred to as clutter subspace, as demonstrated in Fig. 6.2. We rewrite the ADMIRE model matrix in (6.1), expressed as,

$$X = [X_{ROI}\ X_{clutter}], \tag{6.6}$$

where X_{ROI} is the model predictors from the ROI subspace and $X_{clutter}$ is the predictors from the clutter subspace. We also note that the ADMIRE model space is finely sampled in the ROI subspace, but coarsely sampled in the clutter subspace (i.e. $\Delta_{ROI} < \Delta_{clutter}$).

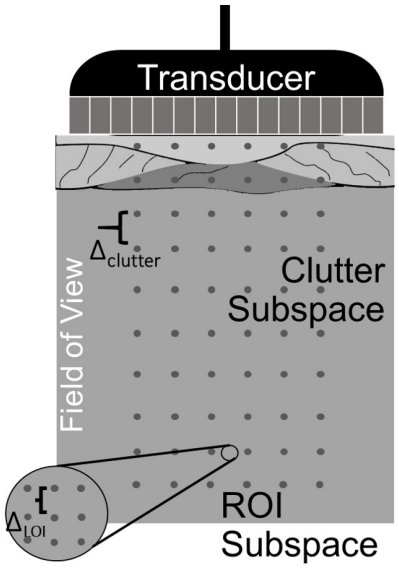

Figure 6.2: ADMIRE model space is illustrated. The ADMIRE model space is sampled in two separated subspaces: (1) region of interest (ROI) subspace and (2) clutter subspace. Because it is also necessary to identify signals of interest using model predictors, the ADMIRE model space is finely sampled in the ROI subspace but not in the clutter subspace (i.e. $\Delta_{ROI} < \Delta_{clutter}$).

It is also important to note that the ADMIRE algorithm and performance are primarily influenced by two factors. One is the model space sampling for each subspace as described above, and the other is the elastic-net regularization parameters, α and λ, in (6.4). Here, we focus only on the role of λ that controls the degrees of freedom (*df*) in this study because the dimensionality reduction will eliminate model space sampling as an important factor for run-time leaving λ as the most significant remaining factor [87]. We scaled a default value of λ set as $0.0189\sqrt{y^\top y}$. The default λ value and other ADMIRE parameters were determined in our previous findings [69, 101, 125], as indicated in Table 6.1. Note that we implemented ADMIRE using a 90% STFT window overlap unless otherwise specified.

Table 6.1: ADMIRE Default Parameters

Parameter	Value
α	0.9
λ	0.0189 $\sqrt{y^\top y}$
c_{lat}	6
c_{axl}	2
Model space (lateral) [m]	aperture length
Model space (axial) [m]	$\{0.001,\ z_r + (c_{axl} res_{axl})/2\}$
Model sampling [m]	
in ROI subspace	$\{0.0716 res_{lat},\ 0.286 res_{axl}\}$
in clutter subspace	$\{1.43 res_{lat},\ 1.43 res_{axl}\}$
STFT window size	(8log(2))/(2πBWf_c)
STFT window overlap	90%

(x_r, z_r) is the center of the ROI specified in Fig. 6.2,
c_{lat} and c_{axl} are lateral and axial scalable factors,
res_{lat} and res_{axl} denote the expected lateral and axial resolutions [69],
BW is the fractional bandwidth and
f_c is the center frequency of transmitted pulse.

6.2.3 Computational Complexity

The total computational cost of the ADMIRE algorithm is high when compared to conventional delay-and-sum (DAS) beamforming. ADMIRE requires additional operations, including short-time Fourier Transform, model decomposition, reconstruction, and the inverse short-time Fourier Transform, which all increase its computational complexity. Table 6.2 summarizes the additional computational complexity of ADMIRE beyond that of DAS. When comparing each computational order, model fitting has a computational burden related to the number of predictors and predictors used, given by $\mathcal{O}(u^3 + u^2 v)$, where u is the number of non-zero coefficients when fitting the data and v is the total number of model predictors in the matrix X in (6.1) [86, 69, 125]. Based on this, a reduced model could substantially decreases the computational time. Because the decomposition process must be repeated for every single frequency used through depth, decreasing the total number of the sliding window steps through depth (i.e., r) should also reduce complexity.

Table 6.2: ADMIRE Computational Complexity Beyond DAS

Operation	Computational Cost
Fourier Transform (FT)	$\mathcal{O}(pqr \log q)$
Model Decomposition	$\mathcal{O}(rw(u^3 + u^2v))$
Reconstruction	$\mathcal{O}(ru)$
Inverse short-time Fourier Transform (ISTFT)	$\mathcal{O}(r + qr \log q)$
Additional Computational Cost	$\mathcal{O}(r + rw(u^3 + u^2v) + ru + pqr \log q + qr \log q)$

p is the number of channels,
q is the number of samples per STFT window,
r is the total number of the sliding window steps through depth determined by STFT window overlap,
u is the number of non-zero coefficients often fitting the data,
v is the total number of model predictors in the model matrix (changes per depth),
w is the number of frequencies used.

6.2.4 ADMIRE Using Dimensionality Reduced Models

We investigated several approaches for reducing the size of the model X in (6.1). Specifically, we examined the role of Gram-Schmidt orthonormalization (GSO) [150, 151], singular value decomposition (SVD) [155, 156] and independent component analysis (ICA) [157, 152]. In this section, we briefly look into each of these methods to understand how the transformed basis vectors construct a reduced model used for a computationally-efficient ADMIRE implementation.

6.2.4.1 Gram-Schmidt Orthogonalization

Gram-Schmidt Orthogonalization (GSO), also called the Gram-Schmidt process, is a classic approach to constructing an orthonormal set from a given set of linearly dependent vectors[151]. The process starts with any one of the vectors in the set and sequentially forms the orthonormal vectors. Different outcomes are obtained from different ordering [150]. The dimension of a reduced model after applying GSO is $X_{gso} \in \mathbb{C}^{\mathbb{M} \times 2\mathbb{M}}$, much less than the original X (i.e., $2\mathbb{M} < \mathbb{N}$). We randomly reordered the model predictors in

each subspace before applying GSO.

6.2.4.2 Singular Value Decomposition

Singular value decomposition (SVD) is widely used in matrix dimensionality reduction to make computations more efficient and decrease computational complexity. We use the SVD algorithm on subspaces of the ADMIRE model matrix in (6.6) to reduce the number of model predictors in each subspace. An SVD-based reduced model, denoted as X_{svd}, has the dimension reduced to $X_{svd} \in \mathbb{C}^{\mathbb{M}\times 2\mathbb{M}}$, the same as with X_{gso}.

6.2.4.3 Independent Component Analysis

Independent component analysis (ICA) removes higher-order correlation [158, 159], leading to a set of separate independent sources that are statistically independent vectors. Given a linear mixture of underlying sources, we can reconstruct the underlying source with an unmixing matrix W. The aim of using ICA here is to solve the unmixing matrix and to form a reduced model using the columns of W^{-1} that are the independent components of the ADMIRE model, indicated by Shelens [159]. The model reduced using ICA is statistically independent but not orthogonal and have a nongaussian distribution [152]. The model dimension after applying ICA is also by $X_{ica} \in \mathbb{C}^{\mathbb{M}\times 2\mathbb{M}}$ as with the other methods.

Because there is no analytical form to determine the unmixed matrix W, the ICA solution must involve estimation techniques [152]. These estimation algorithms are based on information theoretical principles, using maximum-likelihood, information maximization, marginal entropy, negentropy or non-Gaussianity maximization and mutual information maximization, which are all related to one another [160]. In this study, we mostly used an ICA algorithm called fourth-order blind identification (FOBI), which is probably the simplest method for performing ICA [161, 159]. Additionally, we selected and compared four other ICA algorithms accounting for complex values scenarios: i) RobustICA that is a deflated version of fastICA [162, 157] with complex data support [163, 164], ii) complex

ICA-EBM, representing complex ICA by entropy bound minimization [165, 166, 167], iii) second-order blind identification (SOBI) [168], and iv) an algorithm for multiple unknown signals extraction (AMUSE) that may be useful in time structured signals or time series [169].

6.2.5 ADMIRE with Different Levels of STFT Window Overlap

When considering other effects to make ADMIRE more efficient and faster, we tested the impact of different levels of STFT window overlap on image quality using simulated speckle-based target phantoms. We applied the STFT window overlap ratio, ranging from 0.05 to 0.95, when implementing ADMIRE using full and reduced models. We then assessed the resulting ADMIRE images qualitatively and quantitatively. Additionally, we simulated a point target to compare point spread functions derived from DAS and full model ADMIRE implemented with a non-overlap and 50% and 90% overlaps with the STFT window. We also quantified the full-width at half-maximum (FWHM) of the lateral beam profiles.

6.2.6 Simulated Phantom Data

We simulated speckle-based target phantoms with a 5 mm diameter and 3 cm deep anechoic cyst using Field II [17, 18]. The background speckle was fully-developed with 25 scatterers per resolution cell [103]. We generated 6 speckle realizations. A linear array transducer was modeled with 3.0 MHz center frequency and 60% fractional bandwidth with transmit focal depth of 3 cm, as summarized in Table 6.3. We also added various levels of reverberation clutter relative to signals of interest (SOI), given by signal-to-clutter ratio (SCR),

$$SCR = 10 \log 10 \left(\frac{\text{Power}_{\text{SOI}}}{\text{Power}_{\text{Clutter}}} \right). \tag{6.7}$$

We simulated -20, -10, 0, 10 and 20 dB SCRs using an efficient pseudo non-linear simulation tool [4, 170].

Table 6.3: Field II Simulation Parameters

Parameter	Value
Number of elements	117
Number of mathematical elements (lateral)	15
Number of mathematical elements (elevational)	11
Height of element	4 mm
Width of element	0.254 mm
Kerf	0.003 mm
Lateral pitch	0.257 mm
Center frequency (f_c)	3 MHz
Sampling frequency: simulation ($f_{s_{sim}}$)	640 MHz
Sampling frequency: downsampled (f_s)	40 MHz
Fractional bandwidth	60%
Transmit focal depth	3 cm
Transmit/Receive f-number	1.0

We evaluated the resulting images formed after ADMIRE using full and reduced models. We applied the default value of λ scaled by 1/2 (i.e., $0.0189\sqrt{y^\top y}/2$). We tested the usefulness of reduced models using the methods in comparison with images formed using a full model. We also added delay-and-sum (DAS) images in order to quantify relative improvements of ADMIRE images from DAS beamforming.

6.2.7 Experimental Phantom Data

We also applied ADMIRE using these reduced models to experimental phantom data to test whether the simulation results correlate with experimental findings. We acquired data from a tissue-mimicking phantom (Multi-Purpose Multi-Tissue Ultrasound Phantom 040GSE, CIRS Inc., Norfolk, Virginia, USA) using a Verasonics Vantage Ultrasound System (Verasonics, Inc., Kirkland, WA). We used a C5-2 curvilinear array transducer to acquire 128 A-lines over a 75° degree sector, which is the same probe setting we used for our previous study [90]. Table 6.4 summarizes the settings for the curvilinear probe and the

Verasonics ultrasound system.

Table 6.4: C5-2 Curvilinear Transducer and Verasonics System Settings

Parameter	Value
Sector	75°
Number of elements	128
Pitch	0.425 mm
Center frequency (f_c)	3.125 MHz
Sampling frequency (f_s)	12.5 MHz
Fractional bandwidth	60%
Transmit focal depth	3 cm
Transmitted pulse	1.5 cycles
Transmit/Receive f-number	1.0
Speed of sound (c)	1540 m/s

The experimental data were beamformed using DAS, ADMIRE using a full model and three reduced models based on 1). GSO, 2) SVD, and 3) ICA-FOBI methods. Additionally, with the experimental data, we compared five ICA algorithms using image quality metrics and speckle statistics. We applied the default value of λ scaled by 1/2 in the implementation of ADMIRE.

6.2.8 *In Vivo* Data

We acquired *in vivo* abdominal and liver data from a healthy human subject using the same Verasonics ultrasound system and the same C5-2 transducer. The acquisition sequences and parameter settings are also indicated in Table 6.4. We applied ADMIRE to the *in vivo* data using the same models tested in the experimental data. We also applied five different λ parameters, scaled by factors of 1/10, 1/5, 1/2, 1 and 2, to the default λ value to test how the parameters of λ (i.e., the degrees of freedom *df*) impact ADMIRE's performance and efficiency using a reduced model. The Vanderbilt University Institutional Review Board approved the study.

6.2.9 Image Quality Metrics and Speckle Statistics

We compared outcomes using contrast (C), contrast-to-noise ratio (CNR) and speckle signal-to-noise ratio (SSNR) of B-mode data acquired from simulations, experimental tissue-mimicking phantoms and *in vivo* scans.

$$C = -20\log 10(\frac{\mu_l}{\mu_b}), \tag{6.8}$$

$$CNR = 20\log 10(\frac{|\mu_l - \mu_b|}{\sqrt{\sigma_l^2 + \sigma_b^2}}), \tag{6.9}$$

$$SSNR = \frac{\mu_b}{\sigma_b}, \tag{6.10}$$

where (μ_l, σ_l^2) and (μ_b, σ_b^2) are the value of (mean, variance) of the uncompressed enveloped data inside and outside anechoic or hypoechoic structures, respectively.

6.2.10 Timing Measurements

We evaluated timing reduction using simulated phantoms and *in vivo* liver data. We measured the total single-core serial run time for each case of ADMIRE in MATLAB (The Mathworks Inc., Natick, MA, USA) on a 3.40 GHz CPU desktop computer. Timing measurements were conducted in several scenarios, including ADMIRE using various λ values and with different levels of STFT window overlap ratio. We were also interested in computing the computational order from the total number of model predictors and the number of non-zero coefficients using full and reduced models through depth.

6.3 Results

6.3.1 Reduced Model Evaluation Using Simulations

Fig. 6.3 shows B-mode images of a simulated anechoic cyst phantom reconstructed after applying ADMIRE using a full model and three reduced models based on the GSO, SVD and ICA-FOBI methods, along with conventional DAS beamforming. When comparing the resulting ADMIRE images qualitatively, there are no noticeable differences in moderate or lower clutter environments. However, there are substantial discrepancies in image quality between each model in high clutter scenarios (i.e., the range of SCR $\leq$ -10 dB). They all have image artifacts at -20 dB SCR. The images obtained from ADMIRE using the GSO-based reduced model also include very obvious image artifacts in the presence of clutter of -10 dB SCR. It is also interesting to note that the ICA-FOBI reduced model may provide improved performance of ADMIRE, compared to the other two reduced models, throughout the range of clutter levels.

The matched quantitative results are presented using a box plot in Fig. 6.4. For both contrast and CNR values, we measured relative improvements of post-ADMIRE images to DAS B-mode images, but speckle SNR values were compared to the ideal value of 1.91 [103]. Unsurprisingly, ADMIRE improves contrast and CNR in moderate clutter environments while preserving speckle statistics in the cases of ADMIRE using full or ICA-based model. These findings are consistent with results reported in our previous study [125].

In comparison with the performance of ADMIRE using three reduced models, the qualitative and quantitative results are consistent, indicating that ADMIRE performance using the ICA-FOBI reduced model is the most similar to that of using a full model. It is worth noting that ADMIRE using an SVD-based reduced model provides higher contrast while decreasing the value of CNR and speckle SNR. These SVD findings have been reported in our previous study [149], which may produce dark region artifacts [104] and decrease the dynamic range [105].

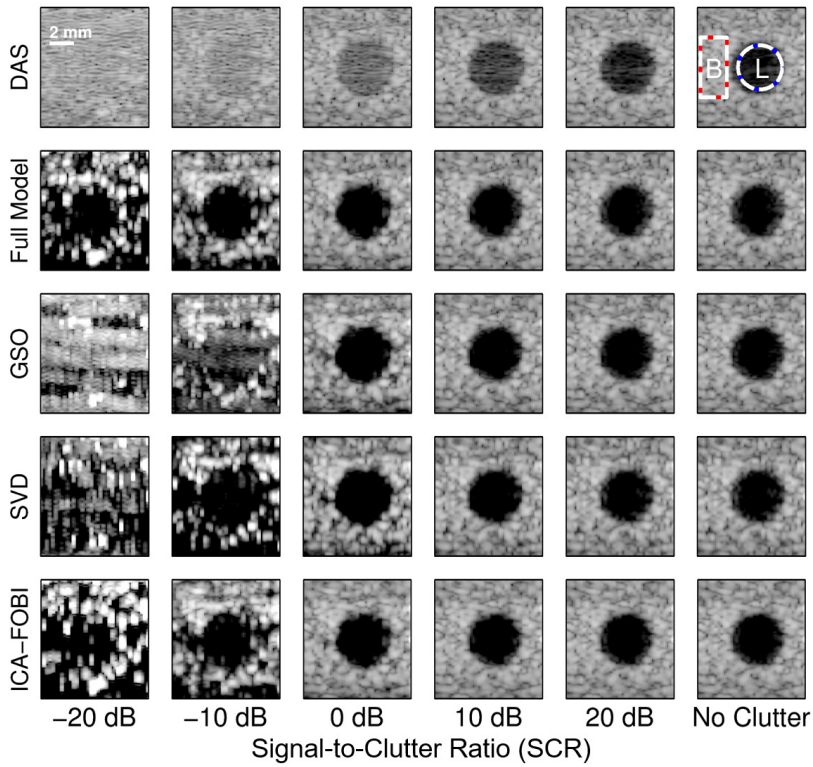

Figure 6.3: B-mode images of simulated anechoic cyst phantom reconstructed after applying delay-and-sum (DAS), ADMIRE using a full model and three reduced models based on the GSO, SVD and ICA-FOBI methods. The phantom has 5 mm diameter 3 cm deep anechoic cyst simulated using Field II. Reverberation clutter ranging from -20 dB to 20 dB SCRs was also added using our pseudo non-linear simulator [4]. The top left DAS B-mode image indicates two regions used for image quality metrics and speckle statistics measurements. We denote lesion and background, corresponding to inside and outside an anechoic structure, as L or B, respectively. The dynamic range is 60 dB.

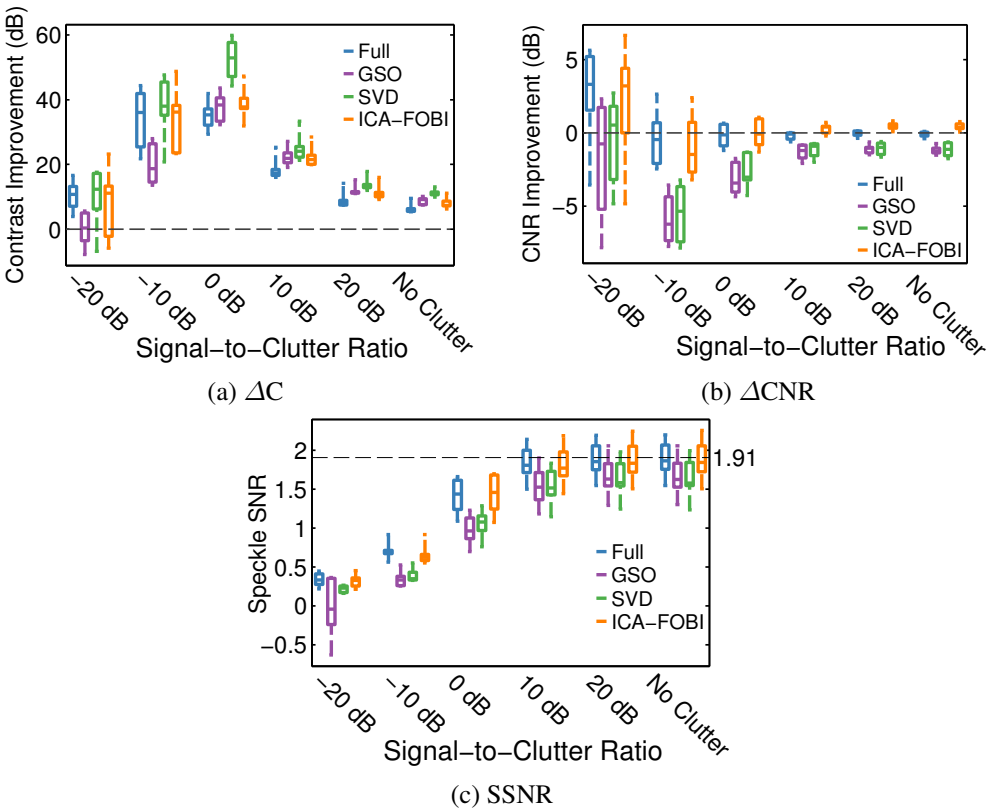

(a) ΔC

(b) ΔCNR

(c) SSNR

Figure 6.4: Box plots of the matched quantitative results of the B-mode images in Fig. 6.3, including contrast (ΔC) and CNR (ΔCNR) improvements relative to DAS, along with speckle SNR (SSNR). There are 6 speckle realizations. These results show good correlation with qualitative indications, as demonstrated in Fig. 6.3.

6.3.2 Reduced Model Evaluation Using Tissue-Mimicking Phantom

Fig. 6.5 demonstrates the methods on experimental phantom data. The figure also includes the matched DAS B-mode image, indicating two sets of regions used to calculate image quality metrics and speckle SNR. We then averaged the measured image metrics, along with the standard deviation. The matched contrast, CNR and speckle SNR values are summarized in Table 6.5. These results from experimental tissue-mimicking phantom data are mostly consistent with the results reported in the simulations, suggesting that the ICA-FOBI reduced model allows ADMIRE to perform as well as ADMIRE performance using a full model.

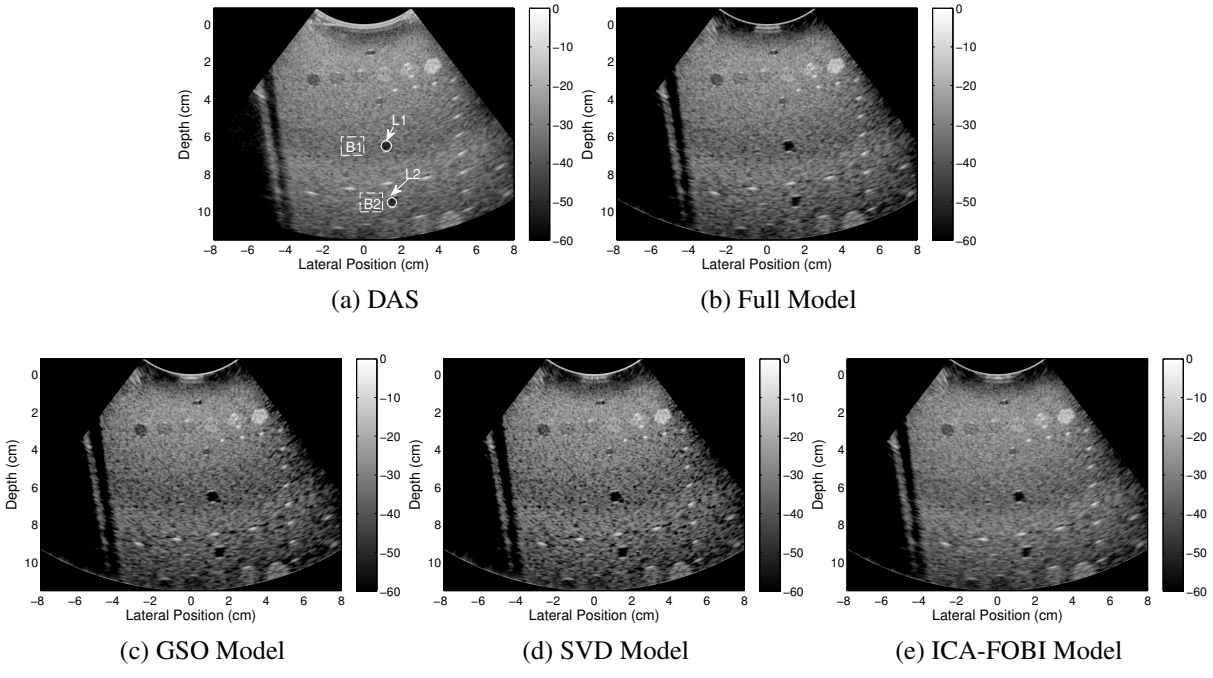

(a) DAS (b) Full Model

(c) GSO Model (d) SVD Model (e) ICA-FOBI Model

Figure 6.5: B-mode images reconstructed using experimentally acquired data on a tissue-mimicking phantom. The images were formed after applying DAS and ADMIRE using different models when implemented, including a full model and three reduced models using the GSO, SVD and ICA-FOBI methods. The dynamic range is 60 dB. The DAS B-mode image also indicates two sets of regions used to compute contrast, CNR and speckle SNR (SSNR). The measured contrast, CNR and SSNR values were averaged with the standard deviation. The corresponding results are summarized in Table 6.5.

Table 6.5: Tissue-Mimicking Phantom Image Quality Metrics and Speckle Statistics (6 realizations)

	Contrast (dB)	**CNR (dB)**	**SSNR**
DAS	8.78 ± 0.49	1.11 ± 0.53	2.23 ± 0.17
Full	11.47 ± 0.15	1.23 ± 0.20	2.02 ± 0.27
GSO	13.65 ± 0.13	0.55 ± 0.59	1.72 ± 0.23
SVD	13.43 ± 0.26	0.36 ± 0.61	1.58 ± 0.20
ICA-FOBI	11.66 ± 0.35	1.38 ± 0.25	2.12 ± 0.26

6.3.3 Reduced Model Evaluation Using *In Vivo* Liver Scan Data

Fig. 6.6 evaluates the results of using reduced models with *in vivo* abdominal liver scan data. Fig. 6.6 (a) demonstrates four sets of ADMIRE images reconstructed from implementing ADMIRE with different models, with various values of the tunable parameter λ (the default value set as $0.0189\sqrt{y^\top y}$). Fig. 6.6 (b) is the matched DAS B-mode image, and Fig. 6.6 (c) reports the matched quantitative results of contrast, CNR and speckle SNR (SSNR) as a function of λ. The metrics were calculated using the mask regions, L and B, indicating inside and outside anechoic or hypoechoic tissue structures, respectively, in Fig. 6.6 (b). Note that ADMIRE using an ICA-FOBI reduced model performs as well as use of a full model as a function of λ. The finding suggests that the ICA-FOBI reduced model has no significant impact when varying the value of λ. It is also noted that ADMIRE using the GSO- or an SVD-based reduced model may increase the performance if λ is adaptively tuned to match the use of full model ADMIRE, which usually requires higher degrees of freedom, as demonstrated in Fig. 6.6 (c).

6.3.4 Reduced Model Dimension and Computational Cost Reduction

We identified the total number of predictors and the number of predictors used while implementing ADMIRE using full and reduced models. Fig. 6.7 indicates significant di-

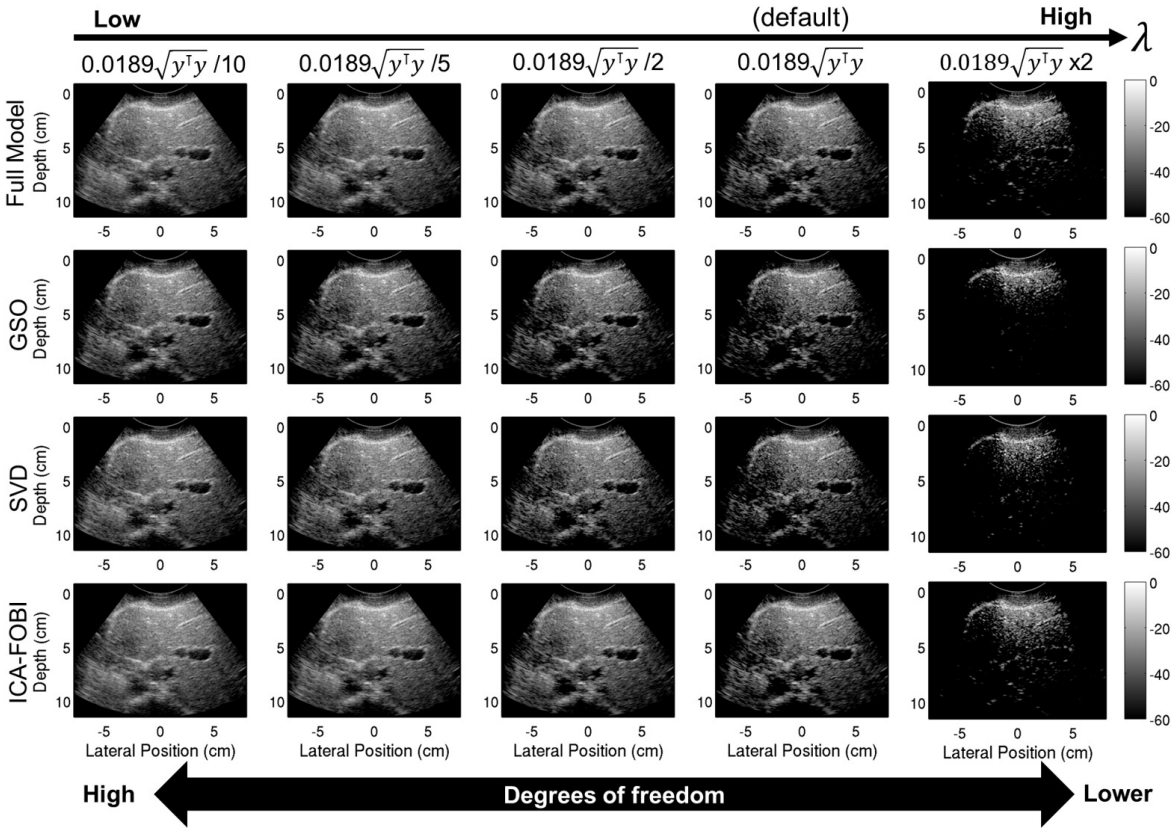

(a) ADMIRE B-mode images as a function of λ or degrees of freedom (df)

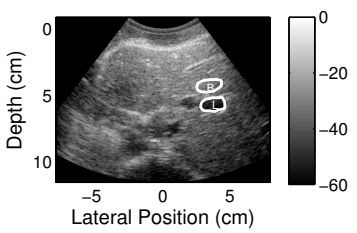

(b) DAS B-mode with mask regions

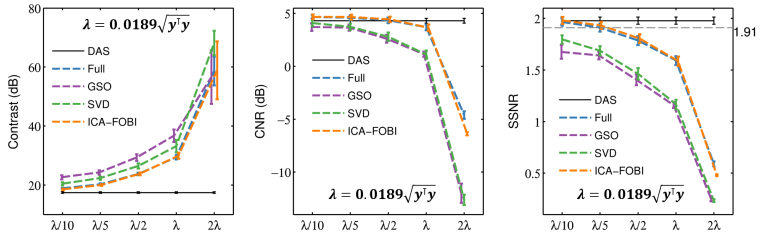

(c) Contrast, CNR and SSNR as a function of λ

Figure 6.6: *in vivo* abdominal and liver B-mode images formed from the data acquired using a Verasonics Vantage Ultrasound System with a C5-2 curvilinear array transducer. ADMIRE B-mode images were obtained from ADMIRE using a combination of different models and tunable parameter λ, in order to examine how the ADMIRE performance relates to the model and the degrees of freedom that is controlled by the parameter of λ. The top in (a) show the resulting images using ADMIRE with a full model as a function of λ. The rest in (a) is the ADMIRE images using a model reduced using the GSO, SVD and ICA-FOBI methods. We also include the matched DAS B-mode image in (b), indicating two regions, L (lesion or hypoechoic structure) and B (background), used to measure image quality metrics and speckle statistics. The dynamic range is 60 dB. The matched quantitative results of contrast, CNR and SSNR as a function of λ are reported in (c).

mensionality reduction in reduced models from simulated phantom and *in vivo* liver data, indicating that computational complexity is reduced by 3 orders of magnitude compared to the computational cost of applying a full sized model.

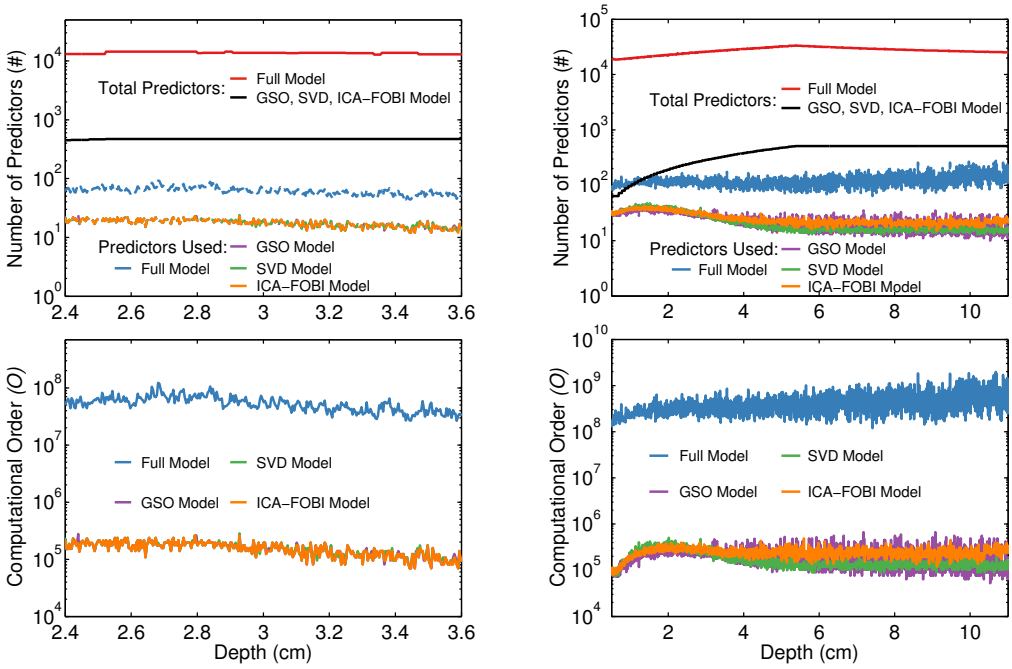

(a) Simulated phantom

(b) *in vivo* liver scan

Figure 6.7: Top figures report the total number of predictors and the number of predictors used (i.e., the number of non-zero coefficients) per depth while implementing ADMIRE using full and reduced models to (a) simulated phantom, (b) *in vivo* liver scan data. The corresponding computational order in model decomposition is also demonstrated in the below.

6.3.5 Impact on Image Quality with Different Levels of STFT Window Overlap

Fig. 6.8 shows the set of 2D point spread functions (PSF) derived from DAS and ADMIRE, using different levels of STFT window overlap, together with the corresponding axial beam profiles. We also quantified the spatial resolution axially, as indicated at upper right in Fig. 6.8 (b). It is worth noting that ADMIRE using a 50% STFT window overlap provides axial resolution as high as that derived from DAS. However, the off-peak lobes persist at a much higher level when compared to the case of ADMIRE using a 90% window

overlap.

Apart from a point target simulation to demonstrate resolution impact, we used simulated cyst phantoms with reverberation clutter at SCR 0 dB to examine how ADMIRE image quality may be correlated with the ratio of STFT window overlap. Fig. 6.9 (a) demonstrates the qualitative results obtained from DAS and ADMIRE, using four different models with different levels of STFT window overlap, ranging from 0.05 and 0.95, while the matched CNR values are reported using line plots with error bars in Fig. 6.9 (b). The results demonstrate that ADMIRE images reconstructed using STFT window overlap lower than 50% may be degraded to some extent, but the qualitative degradation is not noticeable.

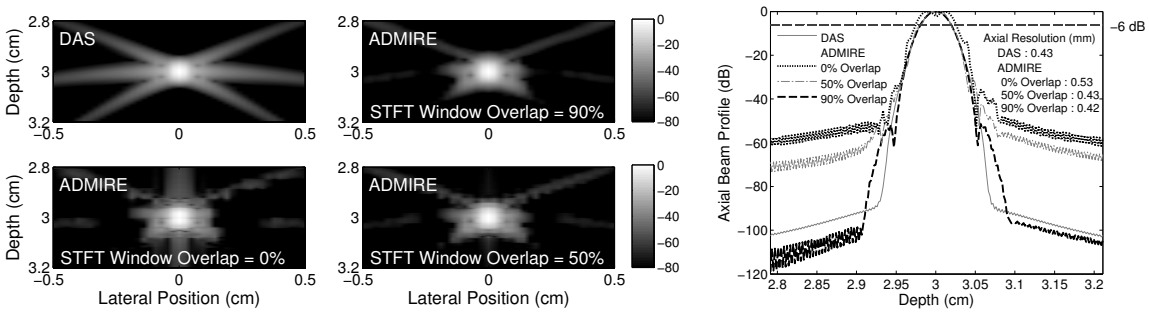

(a) (b)

Figure 6.8: 2D point spread functions (PSF) simulated using DAS and full model ADMIRE with different levels of STFT window overlap ratio are shown in (a). The corresponding axial beam profiles in (b) are used to quantify the axial spatial resolution, also indicated in (b). The dynamic range of 2D PSF images is 80 dB.

6.3.6 Timing Assessment

Table 6.6 summarizes the results of measuring total single-core serial run-times from the matched-data in Fig. 6.7. It is not surprising that an ICA-FOBI model requires a slightly

Table 6.6: Total Single-Core Serial Run Time (sec)

	Full Model	**GSO Model**	**SVD Model**	**ICA-FOBI Model**
Simulated phantom	4,308	237	242	336
in vivo liver scan	136,760	3,294	3,888	4,110

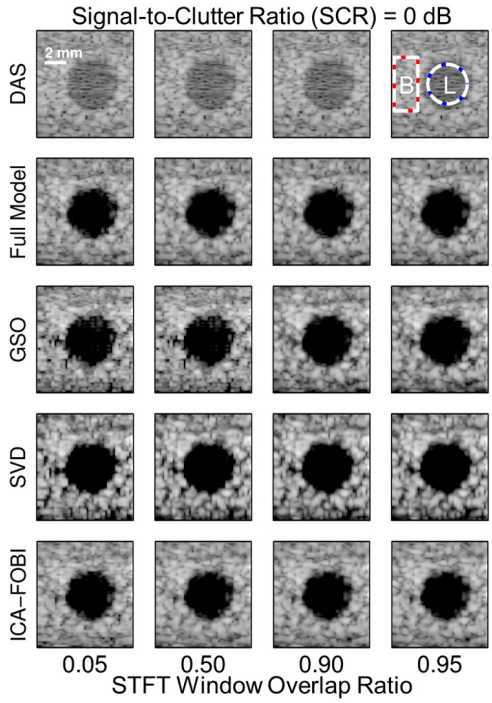

(a)

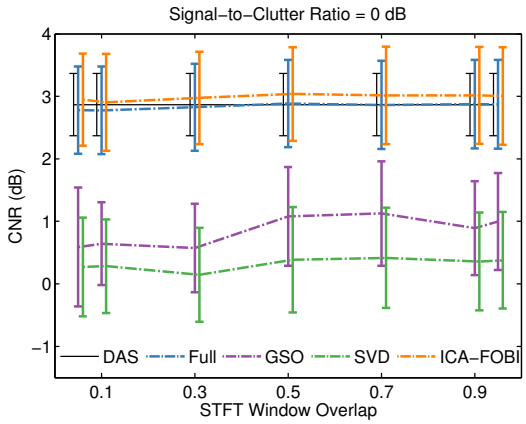

(b)

Figure 6.9: Simulated anechoic cyst images formed after DAS and ADMIRE using four different models with different levels of STFT window overlap, ranging from 0.05 (5%) and 0.95 (95%) are demonstrated in (a). The images are after adding reverberation clutter at SCR 0 dB. The dynamic range is 60 dB. (b) shows the matched contrast-to-noise ratio (CNR) as a function of a STFT window overlap ratio.

longer run-time than the other two reduced models because of the greater number of non-zero coefficients. However, because ADMIRE using an ICA-FOBI model can reduce the run-time and preserve a similar performance to ADMIRE using a full model, the usefulness and benefits of an ICA-FOBI reduced model are substantial.

Fig. 6.10 shows the timing results using various λ values when applied to *in vivo* liver data, indicating that smaller values of λ (i.e., higher degrees of freedom) require a longer run time when implementing ADMIRE, compared to cases of using higher λ values (i.e., lower degrees of freedom). As expected, ADMIRE may have a higher computational cost when implemented in higher clutter environments using higher degrees of freedom.

We also measured the corresponding total single-core run time as a function of STFT window overlap in Fig. 6.11. It is important to note that the use of a 50% STFT window overlap can accelerate ADMIRE's serial run time by more than one order of magnitude, when compared to the use of a 90% STFT window overlap, despite no substantial difference between images, as shown in Fig. 6.9.

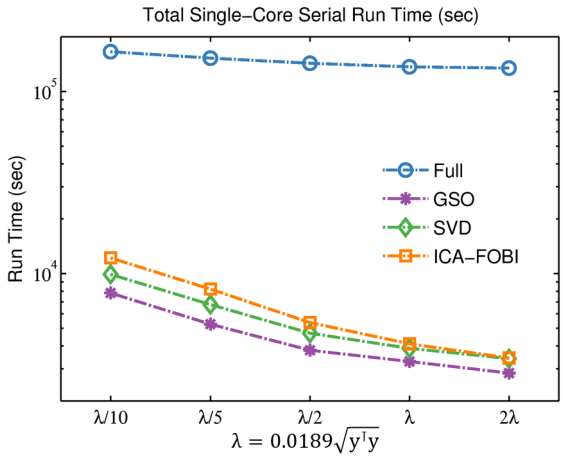

Figure 6.10: The matched total single-core serial run time to reconstruct ADMIRE B-mode images shown in Fig. 6.6 (a). The run times were measured and plotted as a function of λ that controls the degrees of freedom used when implementing ADMIRE.

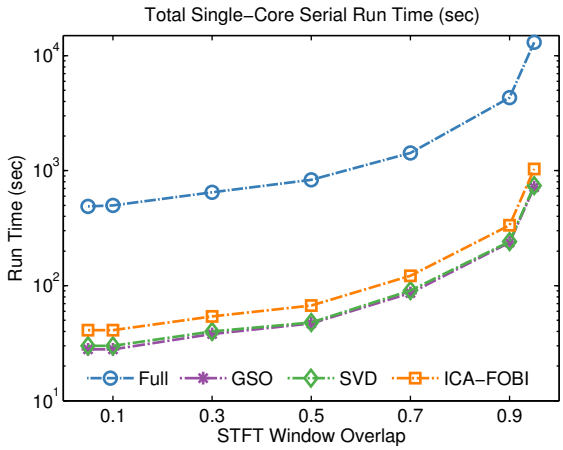

Figure 6.11: The matched total single-core serial run time to reconstruct the demonstrated ADMIRE images in Fig. 6.9. The run times are a function of STFT window overlap ratio.

6.3.7 Comparison of Models Reduced Using Different ICA Algorithms

Fig. 6.12 demonstrates qualitative comparison results, including tissue-mimicking phantom B-mode images resulting from ADMIRE using (a) a full model, a set of ICA-based reduced models using an algorithm called (b) FOBI, (c) robustICA, (d) EBM, (e) SOBI and (f) AMUSE. We then quantified the matched contrast, CNR and speckle SNR (SSNR) to identify which ICA algorithm is superior in terms of producing a high quality ADMIRE image. Table 6.7 reports the quantitative results. Note that the ICA-FOBI and robustICA algorithms show better performance than the others. The EBM and SOBI methods boost perceived contrast, but decrease CNR and speckle SNR with degraded speckle texture. These methods may produce the limitations we found in ADMIRE using a GSO-based and an SVD-based reduced model.

6.4 Discussion and Conclusions

We conducted a comprehensive analysis of dimensionality reduced model methods to identify the usefulness when implementing ADMIRE. A model reduced using an ICA-FOBI method is the most efficient way to accelerate ADMIRE implementation while pre-

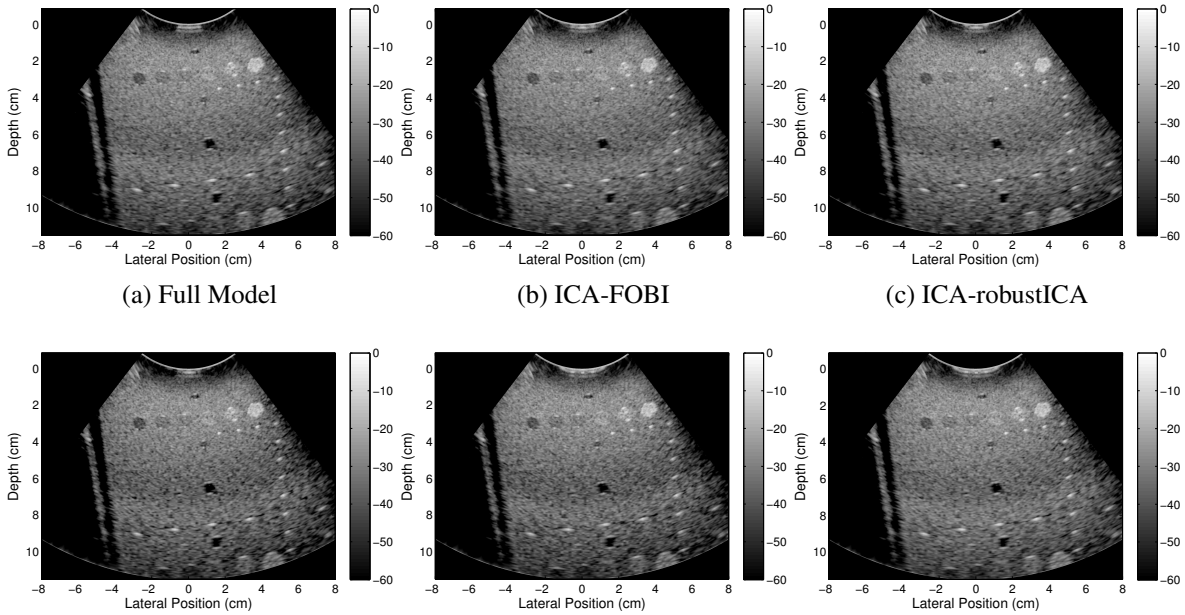

(a) Full Model (b) ICA-FOBI (c) ICA-robustICA

(d) ICA-EBM (e) ICA-SOBI (f) ICA-AMUSE

Figure 6.12: Five ICA algorithms comparison using tissue-mimicking phantom images formed after using a full model and an ICA-base reduced model, along with the ADMIRE resulting image using (a) a full model. (b)-(f) images are post-ADMIRE images using an ICA-based reduced model with five different ICA algorithms, including (b) FOBI, (c) robustICA, (d) EBM, (e) SOBI, and (f) AMUSE. The dynamic range is 60 dB.

Table 6.7: Quantitative Results Using Different ICA Algorithms

	Contrast (dB)	**CNR (dB)**	**SSNR**
DAS	8.78	1.10	2.03
Full	11.47	1.24	2.02
ICA-FOBI	11.66	1.40	2.12
ICA-robustICA	11.55	1.32	2.08
ICA-EBM	12.66	0.80	1.87
ICA-SOBI	12.41	0.85	1.88
ICA-AMUSE	11.70	1.12	1.93

serving ADMIRE performance. The simulation, experimental phantom and *in vivo* results demonstrated in Figs. 6.3, 6.5 and 6.6 indicate that an ICA-FOBI model may enable ADMIRE to perform as well as in the case of using a full model. Also note that the number of predictors of the ICA-FOBI model is reduced by apparently three orders of magnitude.

It is also worth noting that reducing STFT window overlap (default setting in ADMIRE implementation is 90%), may remarkably increase algorithmic efficiency and decrease computational complexity. Based on the findings demonstrated in Figs. 6.9 and 6.11, a 50% STFT window overlap does not result in any significant loss of image quality while speeding up ADMIRE implementation by over one order of magnitude. A combination of using a reduced model method with different levels of STFT window overlap makes ADMIRE more computationally-efficient.

Chapter 7

CONTRAST RATIO DYNAMIC RANGE: A NEW BEAMFORMER PERFORMANCE METRIC

Portions of this work were published in [105]:

K. Dei, A. Luchies, and B. Byram, "Contrast ratio dynamic range: A new beamformer performance metric," *2017 IEEE International Ultrasonics Symposium (IUS)*, Washington, D.C., 2017, pp. 1-4.

7.1 Introduction

The beamformer is one of the most important components of an ultrasound imaging system. Because of this fact, numerous beamforming methods have been proposed that purport to improve ultrasound image quality. Two well-known methods for evaluating beamformer performance include reporting the full-width at half-max (FWHM) of the lateral beam profile and the contrast ratio (CR) observed inside an anechoic cyst relative to the background signals. The anechoic cyst provides useful information about the ability of a beamformer to reject clutter, particularly off-axis clutter (i.e., bright scattering).

However, these metrics are easy to manipulate and useless at predicting how well a beamformer will preserve intrinsic contrast. This has been noted by others [171] and an effort has been made to correct for dynamic range. To address this problem, we propose that dynamic range should be reported as a quality metric, and that it should be measured as the longest continuous duration along the true contrast line. We call the proposed metric contrast ratio dynamic range.

In this study, we applied the metric to several beamformers, including delay-and-sum (DAS), coherence factor (CF) [81], minimum variance (MV) [83, 84], short-lag spatial coherence (SLSC) [66, 68] and aperture domain model image reconstruction (ADMIRE)

[69, 101].

7.2 Beamforming Algorithms

7.2.1 Delay-and-Sum (DAS)

Delay-and-sum (DAS) is a conventional beamforming method, which can be expressed as,

$$BF_{\text{DAS}}(k) = \sum_{m=1}^{M} w_m(k) s(m,k) = \boldsymbol{w(k)}^H \boldsymbol{s(k)}, \tag{7.1}$$

where k is the discrete time index, m indexes the channel, M is the total number of channel elements, $w_m(k)$ is a weighting factor at channel m, $s(m,k)$ is the delayed aperture signal of channel m, $\boldsymbol{w(k)} = [w_1 w_2 \cdots w_M]^H$, H is the conjugate (Hermitian) transpose and $\boldsymbol{s(k)}$ can be expressed in the following matrix form,

$$\boldsymbol{s(k)} = \begin{bmatrix} s_1(k) \\ s_2(k) \\ \vdots \\ s_M(k) \end{bmatrix}. \tag{7.2}$$

For DAS beamforming, the weighting factor, $\boldsymbol{w(k)}$, is determined independently from the channel signals, $\boldsymbol{s(k)}$. For example, a standard DAS uses a rectangular window function, resulting in the weighting factor of $w_m(k)$ to be constantly $1/M$ (i.e., $\boldsymbol{w(k)} = \boldsymbol{1}/M$). In this study, we refer to a standard DAS as DAS, unless otherwise specified.

7.2.2 Coherence Factor (CF)

A coherence factor (CF) is computed using delayed channel signals (i.e., aperture domain signals) [81], given by

$$CF(k) = \frac{\left|\sum_{m=1}^{M} s(m,k)\right|^2}{M\sum_{m=1}^{M}|s(m,k)|^2}. \tag{7.3}$$

The CF is used to adaptively weight beamformed radio-frequency (RF) signals obtained from DAS in (7.1), referred to as DAS+CF. The beamforming with DAS+CF can be expressed as,

$$BF_{\text{DAS+CF}}(k) = BF_{\text{DAS}}(k)CF(k). \tag{7.4}$$

7.2.3 Minimum Variance (MV)

Minimum variance (MV) beamforming uses a set of optimized apodization weights [83, 84], defined as

$$w_{\text{MV}} = \frac{R^{-1}e}{e^H R^{-1}e}, \tag{7.5}$$

where R is the covariance matrix and e is the steering vector. The covariance matrix, R, can be expressed by

$$R(k) = E\left[\boldsymbol{s(k)s(k)^H}\right], \tag{7.6}$$

where $E[\cdot]$ denotes the expectation value, and $\boldsymbol{s(k)}$ is the same as that in (1). To get an invertible R, we used sub-array averaging and diagonal loading. The MV beamforming is expressed as,

$$BF_{\text{MV}}(k) = \boldsymbol{w}_{\text{MV}}\boldsymbol{(k)}^H\boldsymbol{s(k)}. \tag{7.7}$$

7.2.4 Short-Lag Spatial Coherence (SLSC)

Short-lag spatial coherence (SLSC) beamforming was introduced by Lediju *et al.* [66]. The beamforming method does not provide conventional B-mode images, but measures the spatial coherence of received echoes to form coherence images. The concept of SLSC beamforming originated in the van Citter-Zernike (VCZ) theorem [67]. The VCZ theorem predicts the spatial coherence of backscattered signals in aperture domain, where the backscattered signals are recorded by individual aperture elements. In SLSC, the pixels are computed by summing over part of the coherence curve, expressed as

$$BF_{\text{SLSC}}(k) = \sum_{l=1}^{L} \frac{1}{M-l} \sum_{i=1}^{M-l} \frac{\sum_{k=k_1}^{k_2} s_i(k) s_{i+l}(k)}{\sqrt{\sum_{k=k_1}^{k_2} s_i^2(k) \sum_{k=k_1}^{k_2} s_{i+l}^2(k)}}, \tag{7.8}$$

where l is the lateral lag or distance, k is the discrete time, $k_2 - k_1$ is a correlation kernel size of one wavelength. The SLSC beamforming is to integrate the spatial coherence function up to the first L lags in (7.8) [68, 66].

SLSC beamforming generates the spatial coherence-based images at each depth k of each A-line. For SLSC imaging, L is typically the number of elements corresponding to 1-30% of the transmit aperture [68]. In this study, the number of L is determined by 17.1% (equivalent to 20 lags) of the transmit aperture modeled when performing Field II simulation.

7.2.5 Aperture Domain Model Image Reconstruction (ADMIRE)

Byram *et. al* developed a model-based beamforming algorithm to mitigate ultrasound imaging artifacts caused by reverberation, off-axis clutter and wavefront aberration [69, 101]. Because the algorithm uses a physical model of aperture domain signals to reconstruct ultrasound images, we call the algorithm aperture domain model image reconstruction (ADMIRE). This is the model used for the ADMIRE algorithm [69].

$$p_s(x;t,\omega) = \sum_{n=0}^{N-1} A_n(x) e^{j\omega\tau(x;x_n,z_n,\tau_n)}, \tag{7.9}$$

where x is the aperture position, t and ω locate the signal in time and frequency, $\tau(x;x_n,z_n,\tau_n)$ is the wavefront delay for a signal arriving from point (x_n,z_n) at time τ_n and $A(x)$ is the lateral amplitude modulation induced by the short-time Fourier Transform and the element sensitivity. $A(x)$ is also determined by the signal's pulse shape and $\tau(x;x_n,z_n,\tau_n)$.

Using the physical model, the post-STFT aperture domain signal at a single depth can be decomposed using a linear model. The linear model can be expressed as

$$y = X\beta, \tag{7.10}$$

where y is a single frequency and depth post-STFT aperture signal, X is the ADMIRE model matrix for that depth and frequency and β is the model coefficients for the model predictors in X. Because the linear model in (7.10) is ill-posed, the model is solved using the elastic-net regularization technique [86] in the following optimization equation.

$$\hat{\beta} = \arg\min_{\beta}(\|y - X\beta\|^2 + \lambda(\alpha\|\beta\|_1 + (1-\alpha)\|\beta\|_2^2/2)), \tag{7.11}$$

where $\|\beta\|_1$ is the L1 term, $\|\beta\|_2$ is the L2 term, α is between 0 and 1 to determine the relative weight of L1 and L2, and λ is the regularization parameter that is a function of the degrees of freedom (*df*) [87]. (i.e., the elastic-net regularized technique adjusts two independent parameters (α and λ) to determine type and degree of regularization.)

After the model-fit, a decluttered signal (i.e., signal of interest) is reconstructed with model predictors within the region of interest (ROI), given by

$$y_{\text{decluttered}} = X_{\text{ROI}}\hat{\beta}_{\text{ROI}}, \tag{7.12}$$

where $y_{\text{decluttered}}$ is a decluttered signal, X_{ROI} is the model predictors that are spatially within

the ROI and $\hat{\beta}_{\text{ROI}}$ is the corresponding model coefficients. The decluttered signals are then converted into spatial-domain RF channel data using the inverse short-time Fourier Transform (ISTFT) [89].

$$y_{\text{decluttered}} \xrightarrow{\mathscr{F}} \boldsymbol{s}_{\text{decluttered}}, \tag{7.13}$$

where $\xrightarrow{\mathscr{F}}$ is the STFT operator. The ADMIRE beamforming can be expressed as

$$BF_{\text{ADMIRE}}(k) = \boldsymbol{w}(\boldsymbol{k})^H \boldsymbol{s}_{\text{decluttered}}(\boldsymbol{k}), \tag{7.14}$$

where $\boldsymbol{w}(\boldsymbol{k}) = \mathbf{1}/M$ (i.e., a rectangular window function) and $\boldsymbol{s}_{\text{decluttered}}(\boldsymbol{k})$ is the decluttered channel data.

7.3 Methods

7.3.1 Contrast Target Phantom

We used Field II to simulate 5 mm and 10 mm diameter cysts with known scatterer contrast between -50 dB and +60 dB relative to the background. We included an anechoic cyst as well. We also used our pseudo non-linear simulation method [4] to add reverberation clutter at SCR 0 dB. Fig. 7.1 demonstrates four anechoic cyst B-mode images: (a) no clutter, (b) SCR = 0 dB with 5 mm diameter cyst, (c) no clutter, (d) SCR = 0 dB with 10 mm diameter cyst. We simulated 6 realizations of uncluttered and cluttered cases at each contrast level using simulated 5 mm and 10 mm diameter cyst data. Table 7.1 indicates the Field II simulation parameters.

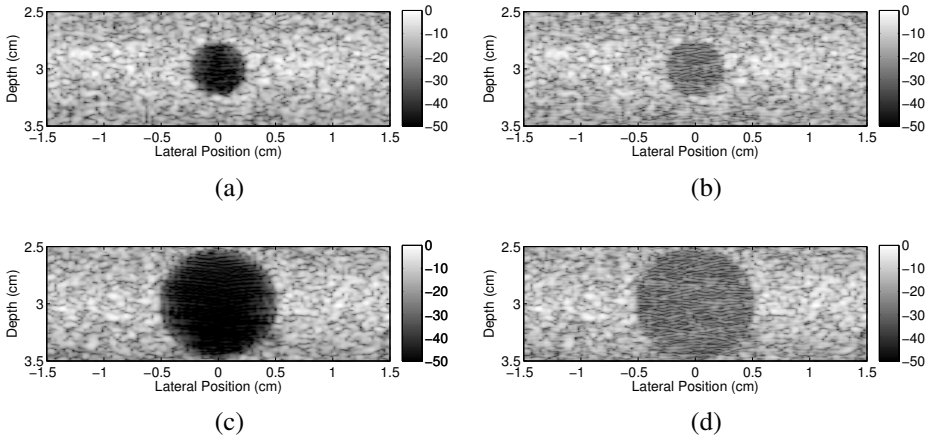

Figure 7.1: Simulated 5 mm (top) and 10 mm (bottom) diameter anechoic cyst images are shown. The images in (a) and (c) are formed by no clutter imaging data, while (b) and (d) are reconstructed after adding reverberation clutter of signal-to-clutter ratio (SCR) 0 dB.

Table 7.1: Field II Simulation Parameters for Contrast Target Phantoms

Parameter	Value
Number of elements	117
Number of mathematical elements laterally	7
Number of mathematical elements elevationally	11
Height of element	4 mm
Width of element	0.254 mm
Kerf	0.003 mm
Lateral pitch	0.257 mm
Center frequency (f_c)	3 MHz
Sampling frequency (simulation) (f_s)	640 MHz
Sampling frequency (downsampled) (f_s)	40 MHz
Bandwidth	60%
Transmit focal depth	3 cm
Transmit/Receive f-number	1

7.3.2 Contrast Ratio Dynamic Range Measurement

We measured contrast ratio (CR) of contrast target phantoms' B-mode images, computed by using

$$CR = 20\log 10(\frac{\mu_L}{\mu_B}),$$

where μ_L, μ_B are the value of mean of the enveloped but uncompressed data inside and outside a contrast cyst structure, respectively. Fig. 7.2 shows areas inside and outside the cyst using a case of 5 mm diameter cyst data.

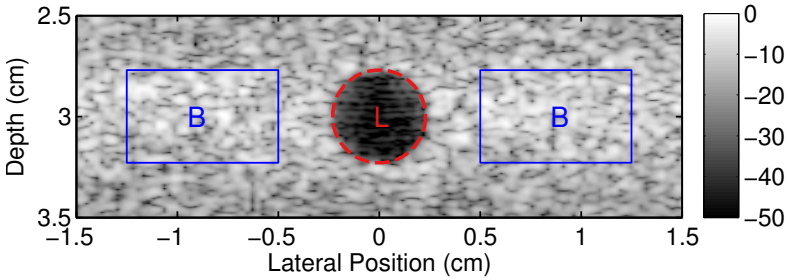

Figure 7.2: The uncompressed, enveloped data inside, indicated by a red dotted line, and outside, corresponding to two rectangular areas enclosed by blue solid lines, are used to compute contrast ratio (CR).

We then quantified the dynamic range based on when the contrast curve was statistically indistinguishable from the intrinsic contrast curve based on a two-tailed *t*-test [172]. Fig. 7.3 depicts the measured contrast ratio dynamic range from the measured contrast (red solid line) and the true contrast line (black dotted line), as one example when using DAS.

We applied the metric to several beamformers: delay-and-sum (DAS), coherence factor (CF), minimum variance (MV), short-lag spatial coherence (SLSC), and aperture domain model image reconstruction (ADMIRE), to evaluate each beamformer's dynamic range. We also implemented ADMIRE with different sets of regularization parameters to suggest how the anechoic cyst case can be gamed with regularized methods.

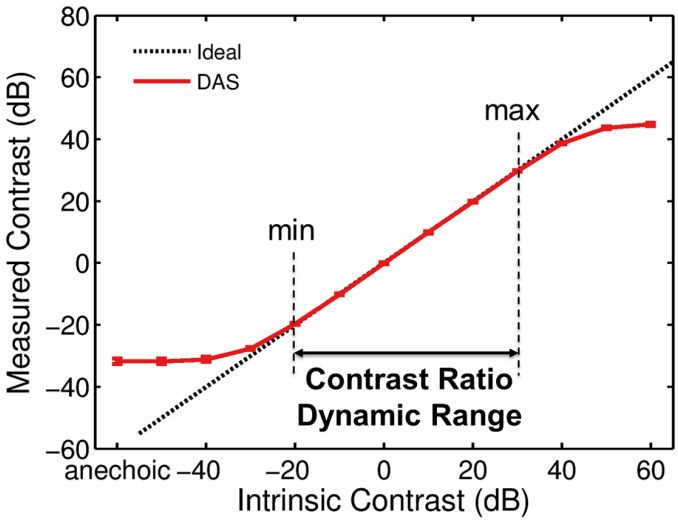

Figure 7.3: The contrast ratio dynamic range is quantified by the longest continuous duration when the measured contrast curve stays along the true line. The figure is an example using DAS beamforming.

7.4 Results and Discussion

Results of measured contrast compared to intrinsic contrast using 5 mm and 10 mm diameter cyst data are show in Fig. 7.4: (a) 5 mm diameter cyst, no clutter, (b) 5 mm diameter cyst, SCR 0 dB, (c) 10 mm diameter cyst, no clutter, (d) 10 mm diameter cyst, SCR 0 dB. The contrast ratio dynamic range using DAS, DAS+CF, MV, SLSC and ADMIRE with low and high degrees of freedom (*df*) are quantified and summarized in Table 7.2.

Figs. 7.5 to 7.8 show the matched simulated cyst images derived from applying DAS, DAS+CF, MV, SLSC and ADMIRE with low and high degrees of freedom (*df*), respectively, with intrinsic contrast between -50 dB and +60 dB relative to the background. (We also include an anechoic cyst.) The demonstrated images in Figs. 7.5 and 7.6 result from unclutter and high clutter environments with SCR 0 dB when using simulated 5 mm cyst structure data, while 10 mm cyst data images are presented in Figs. 7.7 and 7.8 that are also unclutter and SCR 0 dB clutter.

These results indicate 1) clutter decreases dynamic range, 2) most methods have worse dynamic range compared to DAS, and 3) regularized approaches may outperform DAS,

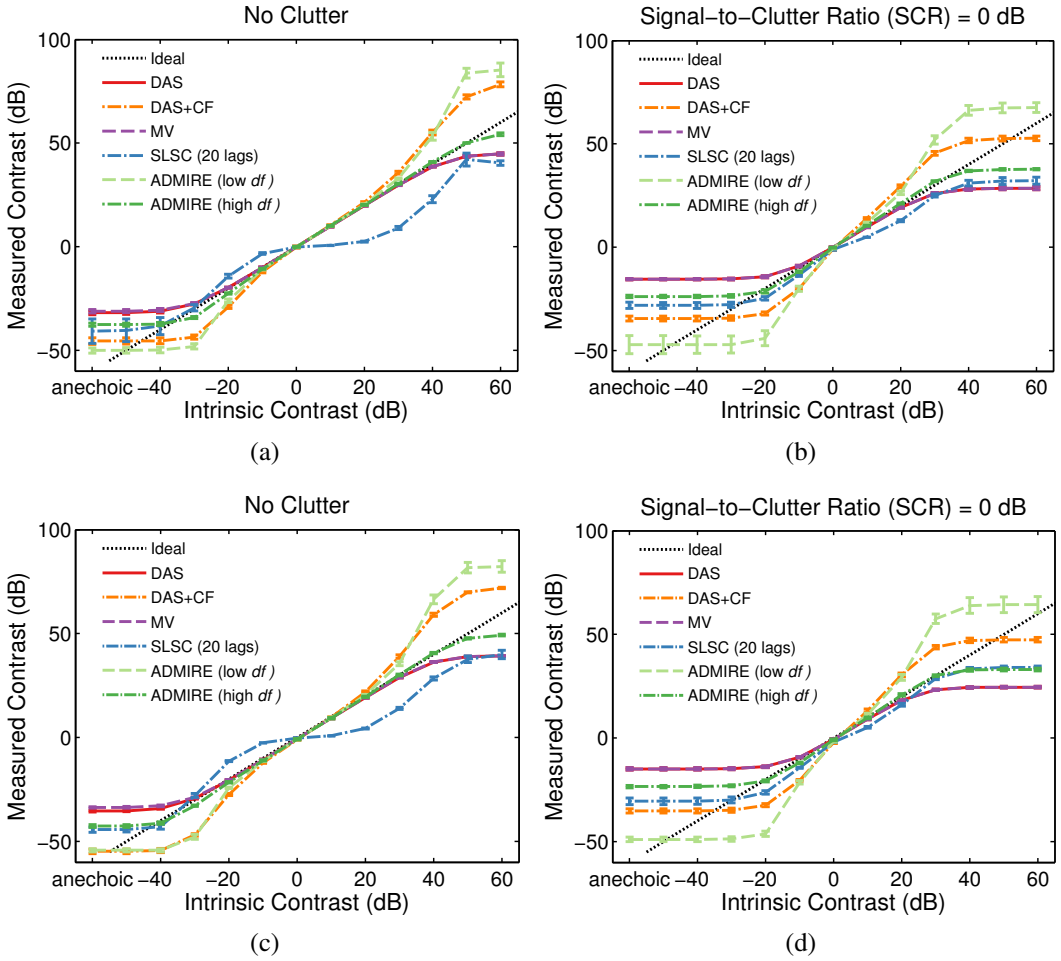

Figure 7.4: Measured contrast compared to intrinsic contrast using 5 mm (top) and 10 mm (bottom) diameter cyst data are shown: (a) 5 mm diameter cyst, no clutter, (b) 5 mm diameter cyst, SCR = 0 dB, (c) 10 mm diameter cyst, no clutter, (d) 10 mm diameter cyst, SCR = 0 dB

Table 7.2: Contrast Ratio Dynamic Range Measurements

Beamformer	**5 mm diameter cyst**		**10 mm diameter cyst**	
	No Clutter	**SCR = 0 dB**	**No Clutter**	**SCR = 0 dB**
	Dynamic Range (dB)			
DAS	56.3	27.1	58.3	27.3
DAS+CF	21.0	3.4	22.8	3.7
MV	55.5	27.1	56.4	26.7
SLSC	17.1	3.1	15.5	3.6
ADMIRE (low *df*)	28.5	3.6	30.4	7.9
ADMIRE (high *df*)	58.1	36.4	59.4	35.7

particularly in high clutter environments, but only with deliberate selection of the tuning parameters. It is also interesting to note that the trends are the same for a larger cyst. A re-evaluation using even larger diameter cyst data may be necessary to identify the maximum achievable contrast ratio dynamic range for each evaluated beamformer. Additional research should be conducted to examine how receiver operating characteristic (ROC) performance is correlated with the contrast ratio dynamic range.

7.5 Conclusions

In this study, we proposed that contrast ratio dynamic range should be reported as a quality metric to evaluate a beamformer's performance. As demonstrated in Fig. 7.4, standard DAS outperforms most novel beamformers, except for ADMIRE with high degrees of freedom (df). It is important to note that dynamic range is decreased by clutter. There is no substantial difference between results obtained from using 5 mm and 10 mm cyst data.

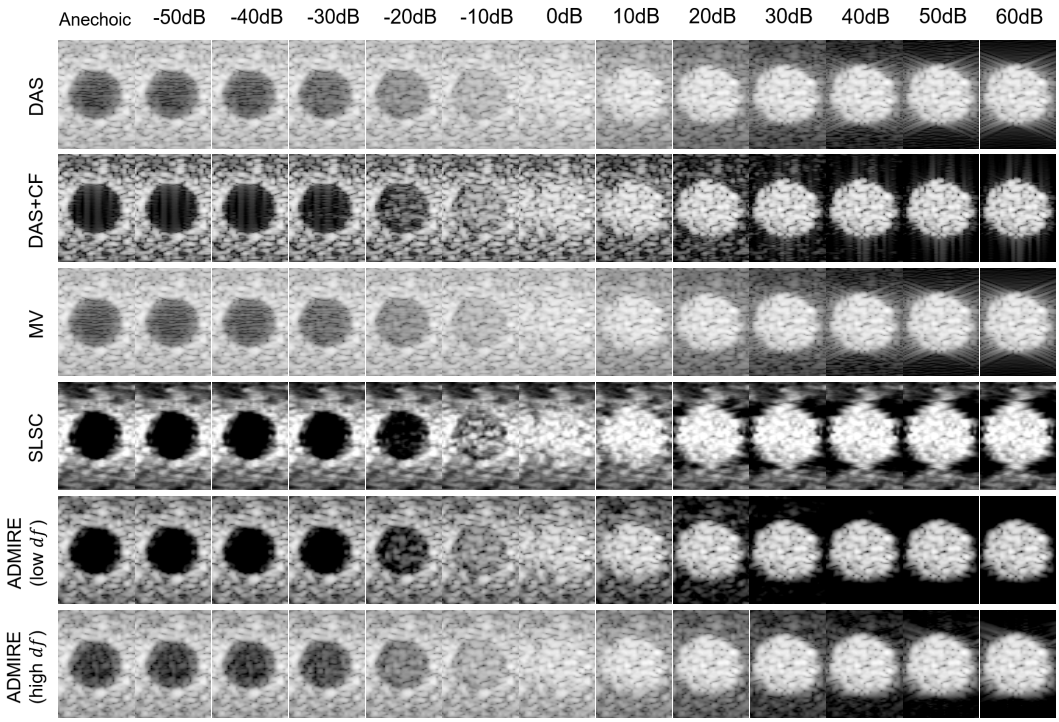

Figure 7.5: Simulated 5 mm diameter cyst images formed from applying five different beamformers with known scatterer contrast between -50 dB and +60 dB relative to the background, along with anechoic cyst. These images are no clutter added (i.e., unclutter cases). The dynamic range is 70 dB.

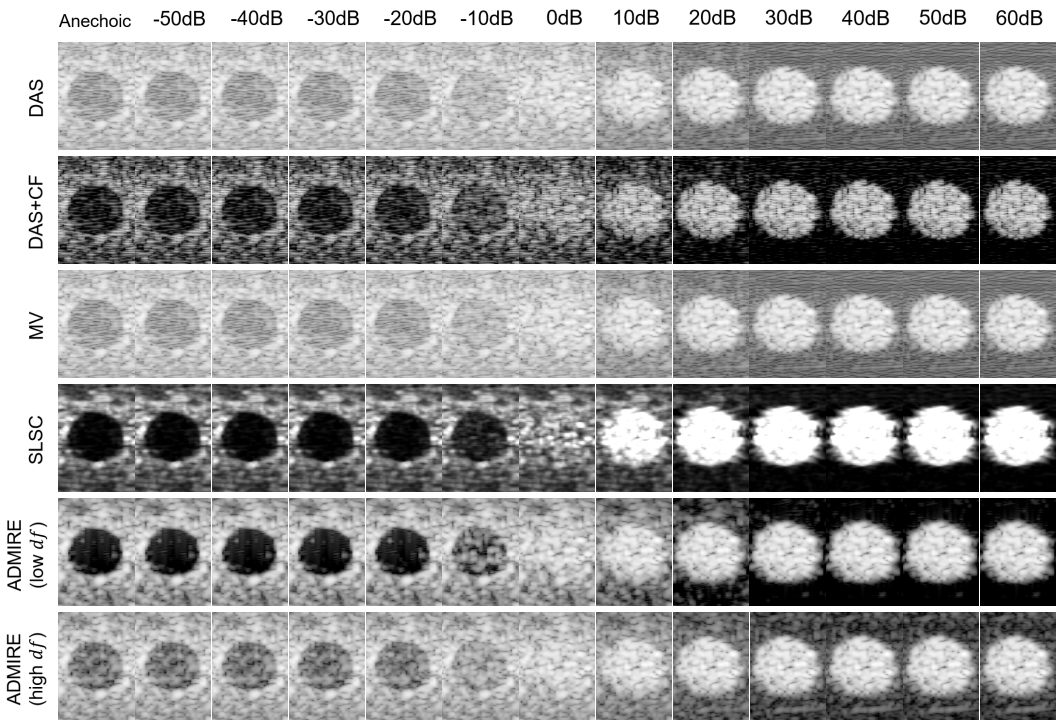

Figure 7.6: Simulated 5 mm diameter cyst images formed from applying five different beamformers with known scatterer contrast between -50 dB and +60 dB relative to the background, along with anechoic cyst. These images are after adding reverberation clutter at signal-to-clutter ratio (SCR) 0 dB. The dynamic range is 70 dB.

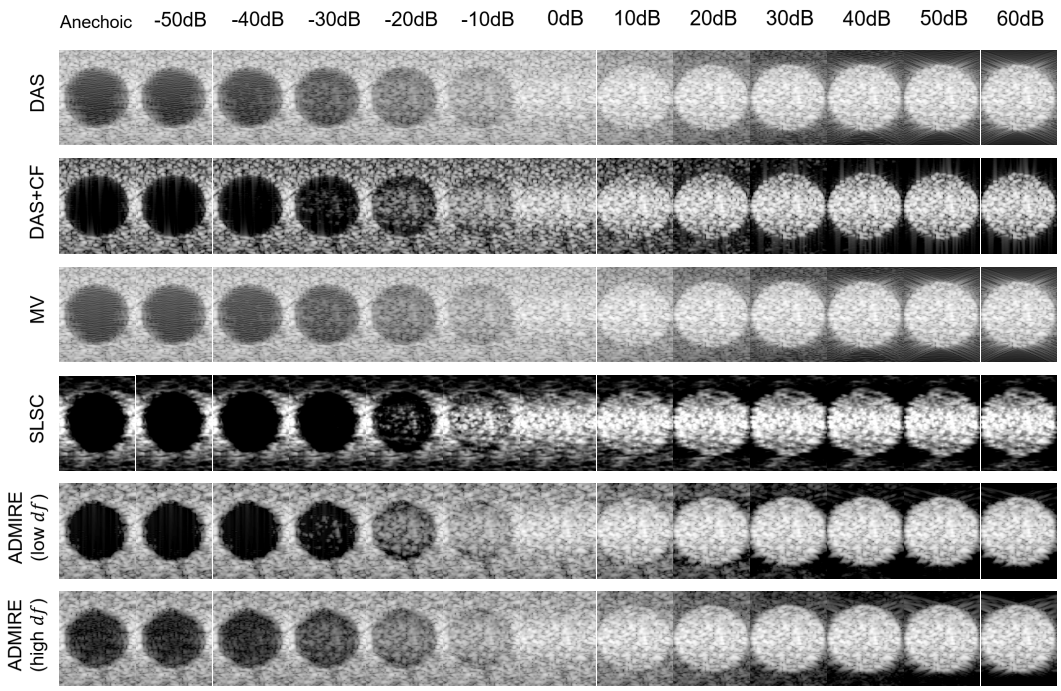

Figure 7.7: Simulated 10 mm diameter cyst images formed from applying five different beamformers with known scatterer contrast between -50 dB and +60 dB relative to the background, along with anechoic cyst. These images are no clutter added (i.e., unclutter cases). The dynamic range is 70 dB.

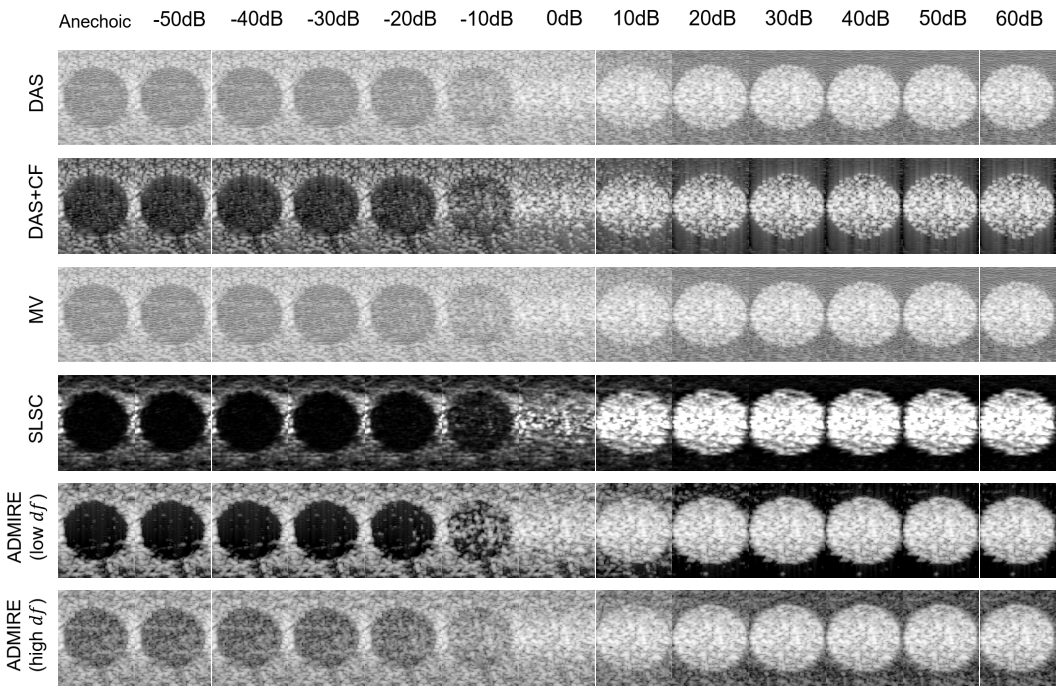

Figure 7.8: Simulated 10 mm diameter cyst images formed from applying five different beamformers with known scatterer contrast between -50 dB and +60 dB relative to the background, along with anechoic cyst. These images are after adding reverberation clutter at signal-to-clutter ratio (SCR) 0 dB. The dynamic range is 70 dB.

Chapter 8

TRANSLATING MODEL-BASED ULTRASOUND IMAGING INTO REAL CLINICAL APPLICATIONS: A PILOT STUDY INTO PERCUTANEOUS RENAL BIOPSY GUIDANCE

This work is part of two published conference proceedings and a manuscript in preparation titled:

- K. Dei, A. Luchies, and B. Byram, "ADMIRE applied to fundamental and harmonic data acquired using a modern clinical platform," *Proc. SPIE*, vol. 10580, pp. 105800F, Mar. 2018. [173]
- K. Dei, S. Schlunk, A. Luchies, D. Brown, and B. Byram, "Assessment of tissue boundary delineation using fundamental and harmonic ADMIRE and SLSC for percutaneous biopsy guidance," *2018 IEEE International Ultrasonics Symposium (IUS)*, Kobe, 2018, pp. 1-4. [174]
- K. Dei, S. Schlunk, A. Luchies, D. Brown, and B. Byram, "Translating Model-Based Beamforming into Real Clinical Applications: A Pilot Study into Renal Imaging."

8.1 Introduction

Ultrasound is used extensively to guide percutaneous biopsies. Ultrasound images used to guide percutaneous biopsy are often of poor quality because of patient orientation and less-than-optimal probe positioning, as the probe position is restricted to the biopsy site. It is also crucial to delineate tissue boundaries during biopsy, but conventional ultrasound images are often too poor to provide well-delineated tissue boundaries. This may be worse in the presence of an acoustic bright needle, and in general, high levels of clutter will blur boundaries. To address such obstacles, numerous beamformers have been developed,

including aperture domain model image reconstruction (ADMIRE) that is a model-based beamformer [41, 69, 101, 90].

Previous studies demonstrated that ADMIRE beamforming mitigates some common ultrasound imaging artifacts, which may increase ultrasound's clinical utility and reliability. Specifically, ADMIRE can suppress clutter caused by reverberation [69], off-axis scattering [90] and wavefront aberration [101]. Along with this, we demonstrated that ADMIRE is robust to model-mismatch caused by gross sound speed deviation [90]. These findings suggest that ADMIRE may be an effective tool to provide high quality images in real clinical applications.

Many of our previous effort have occurred on research platforms because, in general, the configuration of clinical ultrasound systems does not make raw (i.e., pre-beamformed) channel data available [175, 176]. Access to such data is crucial in developing improved beamforming and imaging techniques. Recent work in this area has enabled us to obtain raw channel data using research oriented platforms [177]. However, it is thought that dedicated clinical systems have better front-end electronics and transducers compared to research oriented platforms. If this is true then it is important to perform *in vivo* evaluations using the highest quality data possible in order to appropriately characterize (and not overemphasize possible) algorithmic gains. To this end, we modified a Siemens ACUSON SC2000 ultrasound system (Siemens Medical Solutions USA Inc., Mountain View, CA) to capture I/Q channel data using a 6C1 HD curvilinear array transducer (Siemens Healthcare, Ultrasound Business Unit, Mountain View, CA), as shown in Fig. 7.1. We also acquired channel data in conjunction with pulse inversion (PI) sequencing to enable harmonic images [178].

Using the developed data acquisition tools, we acquired both fundamental and second harmonic frequency data from 12 patients undergoing biopsy and cryoablation. We applied ADMIRE to the data and compared the resulting images of fundamental B-mode and harmonic B-mode before and after ADMIRE beamforming using image quality metrics

Figure 8.1: Siemens ACUSON SC2000 ultrasound system and a 6C1 HD curvilinear array transducer are shown.

and speckle statistics (i.e., speckle signal-to-noise ratio). We also aimed to assess whether ADMIRE provides better delineation of tissue boundaries. To conduct the aim, we quantified the sharpness of axial and lateral edges at the boundary of a kidney, using a sigmoid function to estimate the transition length between 10% and 90% of amplitude difference of uncompressed enveloped data. We also applied this methods to imaging data after applying DAS and SLSC [66] beamforming to identify which beamformer can provide sharper and better boundary delineation.

8.2 Beamforming

8.2.1 Delay-and-Sum (DAS)

Delay-and-sum (DAS) is considered a conventional beamforming method that is used as a benchmark tool, compared to newly-developed beamforming methods. The method involves applying relevant delays to received aperture signals (i.e., channel data), followed by a summation of the delayed aperture signals. The post-beamformed signals can be

expressed as,

$$RF_{\text{DAS}}(k) = \sum_{m=1}^{M} w_m(k)s(m,k) = \boldsymbol{w(k)}^H \boldsymbol{s(k)}, \tag{8.1}$$

where k is the discrete time index, m indexes the channel, M is the total number of channel elements, $w_m(k)$ is a weighting factor at channel m, $s(m,k)$ is the delayed aperture signal of channel m, $\boldsymbol{w(k)} = [w_1 w_2 \cdots w_M]^H$, H is the conjugate (Hermitian) transpose. The following matrix forms $\boldsymbol{s(k)}$, given by,

$$\boldsymbol{s(k)} = [s_1(k)s_2(k)\cdots s_M(k)]^\top, \tag{8.2}$$

where $\top$ denotes the matrix transpose. For DAS beamforming, the weighting factor, $\boldsymbol{w(k)}$, is determined independently from the channel signals, $\boldsymbol{s(k)}$. In this study, we used a rectangular window function, constantly weighting each aperture element by a factor of $1/M$ (i.e., $\boldsymbol{w(k)} = \mathbf{1}/M$), unless otherwise specified.

8.2.2 Aperture Domain Model Image Reconstruction (ADMIRE)

A model-based beamforming method is called ADMIRE when abbreviating "A"perture "D"main "M"odel "I"mage "RE"construction. ADMIRE uses physics-based model predictors 1) to decompose received cluttered signals and 2) to reconstruct only signals of interest (i.e., decluttered signals), resulting in improved ultrasound images [69].

We use the physical model in (2.1) to decompose the post-STFT aperture domain signals per a single frequency at a given depth using a linear model, as follows.

$$y = X\beta, \tag{8.3}$$

where y is a single frequency and depth post-STFT aperture signal, X is the ADMIRE model matrix for that depth and frequency and β is the model coefficients for the model

predictors in X. Because the number of model predictors is typically over a hundred times greater than the number of aperture elements, the solution of the linear model in (8.3) is highly ill-posed. To make the ill-posed problem amenable, we apply an elastic-net regularization technique [86]. The solution for β may be expressed as,

$$\hat{\beta} = \arg\min_{\beta}(\|y - X\beta\|^2 + \lambda(\alpha\|\beta\|_1 + (1-\alpha)\|\beta\|_2^2/2)), \tag{8.4}$$

where $\|\beta\|_1$ is the L1 term, $\|\beta\|_2$ is the L2 term, α is between 0 and 1 to determine the relative weight of L1 and L2, and λ is the regularization parameter that is a function of the degrees of freedom (df) [87]. (i.e., α and λ can be used to determine type and degree of regularization.) We call the process model decomposition or model-fit.

After the process, only model predictors within the region of interest (ROI) are selected to reconstruct a decluttered signal, given by

$$y_{\text{decluttered}} = X_{\text{ROI}}\hat{\beta}_{\text{ROI}}, \tag{8.5}$$

where $y_{\text{decluttered}}$ is a decluttered signal, X_{ROI} is the model predictors that are spatially sampled within the ROI and $\hat{\beta}_{\text{ROI}}$ is the corresponding model coefficients. We then apply the inverse short-time Fourier Transform (ISTFT) [89] to covert the decluttered signal into spatial domain channel data, called decluttered channel data, $\boldsymbol{s}_{\text{decluttered}}$. The post-ADMIRE beamformed signals can be expressed as,

$$RF_{\text{ADMIRE}}(k) = \boldsymbol{w}(\boldsymbol{k})^H \boldsymbol{s}_{\text{decluttered}}(\boldsymbol{k}), \tag{8.6}$$

where $\boldsymbol{w}(\boldsymbol{k}) = \mathbf{1}/M$ (i.e., a rectangular window function), unless otherwise specified.

8.2.3 Short-Lag Spatial Coherence (SLSC)

Lediji *et al.* also introduced an acoustic clutter suppression algorithm, called short-lag spatial coherence (SLSC) [66]. In related literature, SLSC demonstrates its robustness in

reducing clutter and improving contrast, contrast-to-noise ratio (CNR) and speckle signal-to-noise ratio (SSNR) from fundamental B-mode images [66, 179, 180, 68]. Furthermore, Dahl *et al.* implemented SLSC using 2^{nd} harmonic imaging data, referred to as harmonic spatial coherence imaging (HSCI), which showed further improvement of ultrasound image quality [112].

Because the idea of SLSC is originated in the van Citter-Zernike (VCZ) theorem [67], predicting the spatial coherence of backscattered aperture signals, the beamforming method does not form a conventional B-mode image, but a coherence image using the measured spatial coherence of received echoes. The coherence imaging data are computed by summing over part of the coherence curve, given by,

$$RF_{\text{SLSC}}(k) = \sum_{l=1}^{L} \hat{R}_l(k), \tag{8.7}$$

where $\hat{R}_l(k)$ is the spatial coherence, often expressed as the spatial correlation which can be estimated by,

$$\hat{R}_l(k) = \frac{1}{M-l} \sum_{i=1}^{M-l} \frac{\sum_{k=k_1}^{k_2} s_i(k) s_{i+l}(k)}{\sqrt{\sum_{k=k_1}^{k_2} s_i^2(k) \sum_{k=k_1}^{k_2} s_{i+l}^2(k)}}, \tag{8.8}$$

where M is the total number of channel elements, l is the lateral lag or distance, $s_i(k)$ is the received aperture signal at the ith element, k is the time or depth in samples, $k_2 - k_1$ is a correlation kernel size (typically, using one wavelength). The SLSC beamforming is derived from integration of the spatial coherence function up to the first L lags in (8.8), stemmed from the second order statistics [66, 68].

Compared to regular B-mode images, SLSC forms the spatial coherence images at each depth k of each A-line. In this study, the number of L is determined by 17.1% of the transmit aperture used for *in vivo* data acquisition.

8.3 Methods

8.3.1 Channel Data Acquisition

We developed a channel data acquisition protocol using a 6C1 HD curvilinear array transducer that is connected to a modified Siemens ACUSON SC2000 ultrasound system. The SC2000 platform essentially supports useful features to access beamformed I/Q data and an additional set of transducer parameters, which is manipulated by using Matlab (The Mathworks Inc., Natick, MA, USA). We modified the features using its internal parameters to extend the system's capabilities to acquire I/Q channel data. The modified channel data acquisition system digitizes the signals received by the transducer.

The I/Q channel data were acquired using a full synthetic receive sequence [181, 182]. Using the method, all aperture elements are used when firing, but the signal from a subset of individual channels is collected when receiving. The same transmit event is repeated until the single channel data are acquired, as illustrated in Fig. 8.2. The acquired I/Q channel data are modulated to reconstruct RF channel signals [183]. Fig. 8.3 demonstrates the channel data reconstruction flow. In this study, we used 16:1 parallel-receive beamforming to acquire 64 channels [179]. With an 11 cm depth field of view, 0.07 sec was required to collect a complete single channel data set (i.e., a complete frame) for a fundamental frequency imaging sequence, while PI harmonic imaging data sets took 0.14 sec.

8.3.2 Pulse Inversion Harmonic Data Acquisition

For pulse inversion (PI) sequencing, we repeated the channel acquisition with an inverted pule immediately following the acquisition of a particular subset of channels. The channel data obtained after summation is the PI harmonic data we used to form the harmonic B-mode image, to which we also applied ADMIRE. Fig. 8.4 demonstrates a set of pulse inverted and non-inverted channel data after reconstruction.

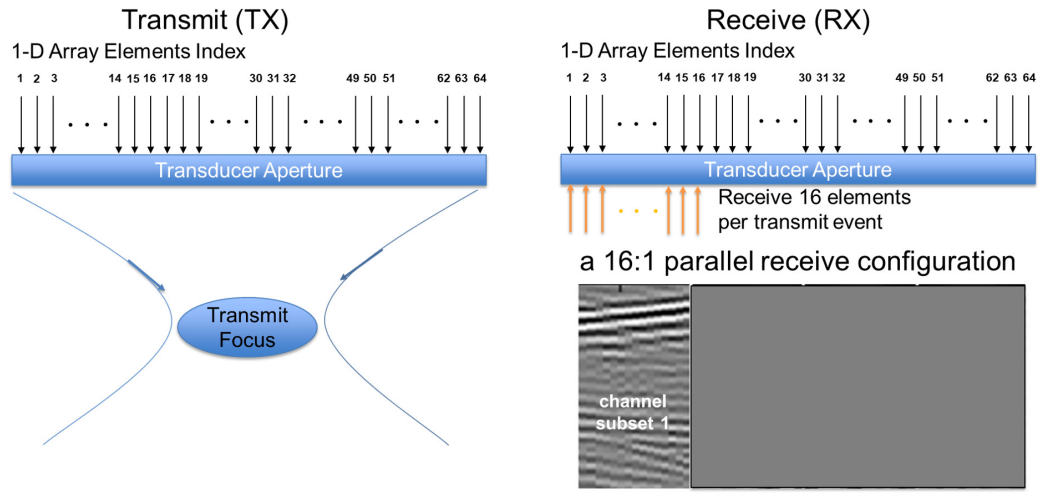

Figure 8.2: The full synthetic receive sequence acquires individual channel data by firing on all aperture elements and receiving on a subset of individual channel. The same transmit event is repeated until the single channel data are acquired. The right figure demonstrates channel data on a first subset of elements are received.

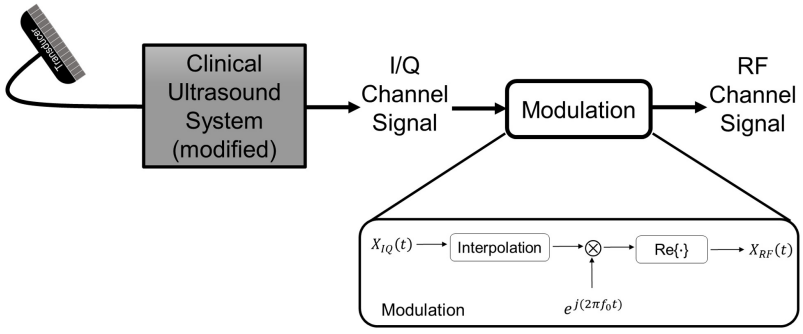

Figure 8.3: RF Channel data reconstruction from I/Q channel data acquired using the developed channel data acquisition protocol.

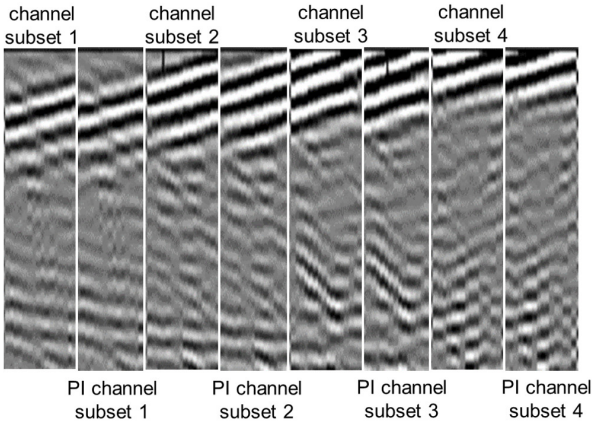

Figure 8.4: Single channel data acquired from a pulse inversion harmonic imaging sequence. The channel data are acquired in clusters and the pulse is inverted between each repeated cluster of channel data.

8.3.3 *In Vivo* Data

We acquired *in vivo* kidney data from 12 patients undergoing biopsy and cryoablation using the developed channel data acquisition protocol. Table 8.1 indicates parameters used to acquire channel data on the modified Siemens ACUSON SC2000 ultrasound system and the 6C1 HD curvilinear transducer array. The Vanderbilt University Institutional Review Board approved this study. We also obtained the written consent of each patient in this study.

Table 8.1: 6C1 HD Curvilinear Probe Settings

Parameter	Value
Sector	40°
Number of elements used	64
Center frequency (fundamental)	Tx/Rx: 3.5 MHz
Center frequency (2^{nd} harmonic)	Tx: 1.8 MHz Rx: 3.6 MHz
Fractional bandwidth	60 %
Transmit focal depth	6 cm %
Transmitted pulse	2.0 cycles
Transmit/Receive f-number	2.0
Speed of sound (c)	1540 m/s

8.3.4 Image Quality Assessment

Image quality was quantified using measured contrast and contrast-to-noise ratio (CNR), calculated using

$$C = -20\log 10(\frac{\mu_{in}}{\mu_{out}}), \tag{8.9a}$$

$$CNR = 20\log 10(\frac{|\mu_{in} - \mu_{out}|}{\sqrt{\sigma_{in}^2 + \sigma_{out}^2}}), \tag{8.9b}$$

$$sSNR = \frac{\mu_{out}}{\sigma_{out}}, \tag{8.9c}$$

where (μ_{in}, σ_{in}^2) and (μ_{out}, σ_{out}^2) are the value of (mean, variance) of the uncompressed envelope data inside and outside hypoechoic structure, respectively.

8.3.5 The Sharpness of Tissue Boundaries

The data set consists of channel data acquired using fundamental frequency and 2^{nd} harmonic pulse inversion sequencing. We then applied ADMIRE and SLSC to the data. Using uncompressed enveloped signals at axial and lateral kidney boundaries, we fit sigmoid functions in order to estimate the transition length τ between 10% and 90% of amplitude difference at the boundary of the kidney. We applied this method to DAS, ADMIRE and SLSC data for fundamental and 2^{nd} harmonic implementations. Fig. 8.5 demonstrates an example of estimates of the transition length (i.e., τ) using a sigmoid function. Better delineation of boundaries should have shorter transitions (i.e., smaller τ values).

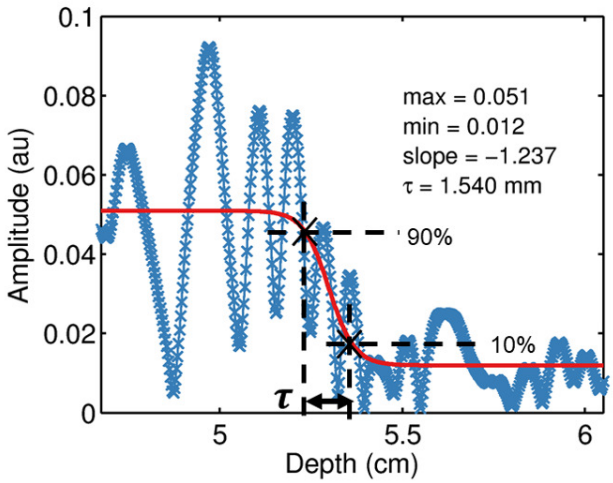

Figure 8.5: An example of estimates of the transition length (i.e., τ) using a sigmoid function. A blue dotted line is an uncompressed enveloped signal, whereas a red solid line indicates the sigmoid curve after fitting. Shorter transitions indicate sharper and better delineated boundaries.

8.4 Results

8.4.1 Fundamental and Harmonic DAS and ADMIRE B-modes

Figs. 8.6 and 8.7 demonstrate two examples of *in vivo* kidney fundamental and harmonic B-mode images reconstructed from DAS and ADMIRE. Table 8.2 summarizes the quantitative results of relative improvements in contrast and CNR from fundamental and harmonic DAS B-modes. Contrast and CNR values measured from DAS and ADMIRE images are shown in Fig. 8.8. In the *in vivo* case, the fundamental and harmonic ADMIRE images qualitatively and quantitatively increase image quality, especially contrast. These results are correlated with our previous study [69, 90].

ADMIRE boosts over +5 dB in contrast from the fundamental DAS B-mode, while the harmonic image formed after applying ADMIRE also improves in contrast (>+4 dB increase relative to the harmonic DAS B-mode). The CNR values of post-ADMIRE images do not show any remarkable improvement. It is notable, though, that hypoechoic lesions inside kidneys are much more apparent in post-ADMIRE images, whereas persistent acoustic clutter causes blurring of DAS B-mode images.

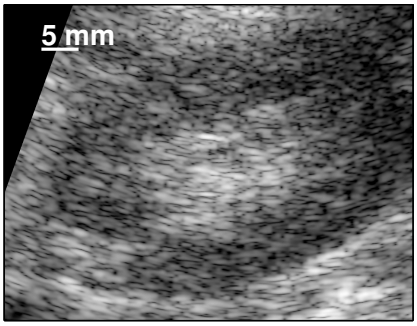

(a) Fundamental DAS B-mode

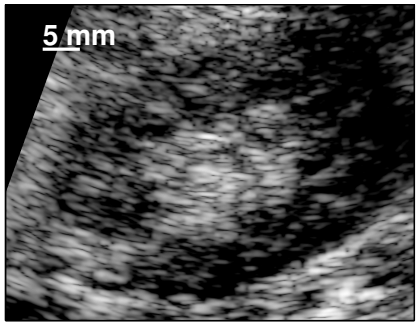

(b) Fundamental ADMIRE B-mode

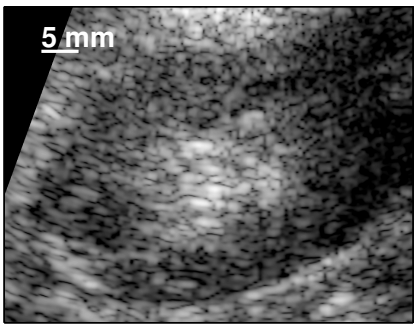

(c) Harmonic DAS B-mode

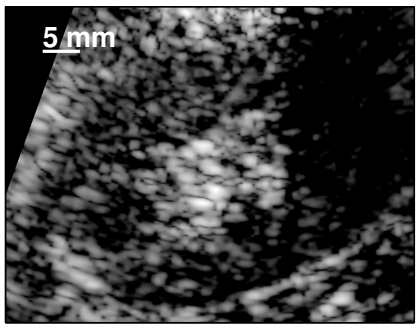

(d) Harmonic ADMIRE B-mode

Figure 8.6: Example 1 of *in vivo* B-mode images. Top images are based on fundamental B-mode images using DAS and ADMIRE. Bottom are pulse inversion (PI) harmonic images of DAS and ADMIRE. Fundamental and harmonic images are nearly matched.

Table 8.2: Contrast and CNR Improvements Relative to DAS B-mode: Fundamental and Harmonic Imaging (12 *in vivo* realizations)

	Fundamental		**Harmonic**	
B-mode	**ΔC (dB)**	**ΔCNR (dB)**	**ΔC (dB)**	**ΔCNR (dB)**
Fundamental DAS	—	—	-2.84 $\pm$ 1.49	-0.50 $\pm$ 1.33
Fundamental ADMIRE	5.62 $\pm$ 1.42	0.11 $\pm$ 0.42	2.77 $\pm$ 1.90	-0.38 $\pm$ 1.90
Harmonic DAS	2.84 $\pm$ 1.49	0.50 $\pm$ 1.33	—	—
Harmonic ADMIRE	7.16 $\pm$ 2.08	0.09 $\pm$ 1.47	4.32 $\pm$ 1.89	-0.40 $\pm$ 0.88

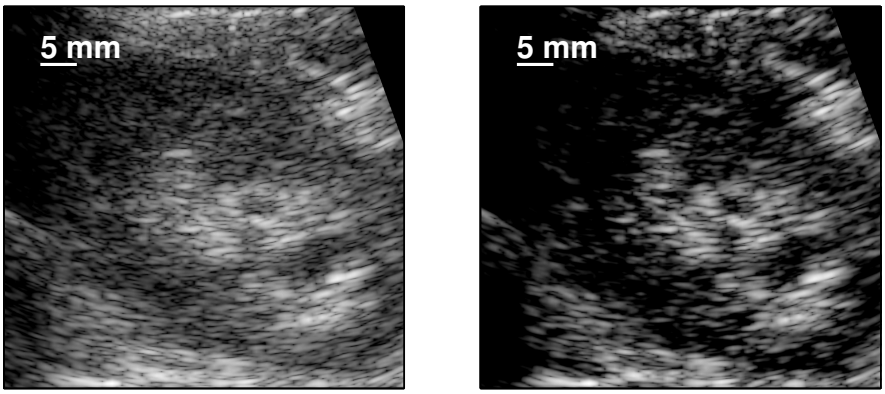

(a) Fundamental DAS B-mode

(b) Fundamental ADMIRE B-mode

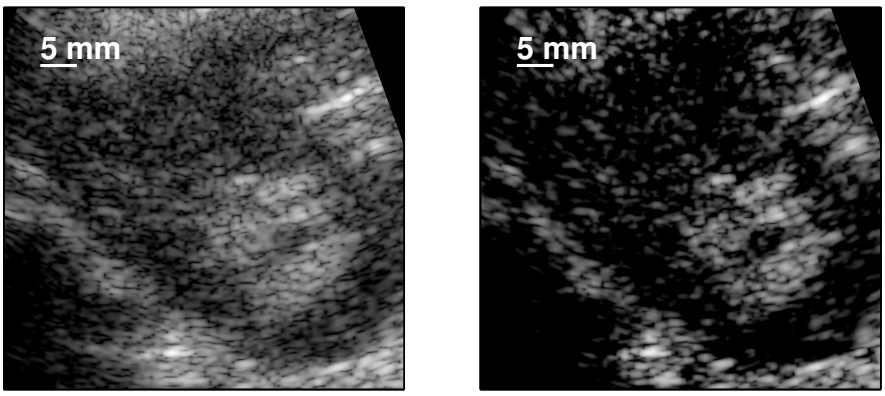

(c) Harmonic DAS B-mode

(d) Harmonic ADMIRE B-mode

Figure 8.7: Example 2 of *in vivo* B-mode images. Top images are based on fundamental B-mode images using DAS and ADMIRE. Bottom are pulse inversion (PI) harmonic images of DAS and ADMIRE. Fundamental and harmonic images are nearly matched.

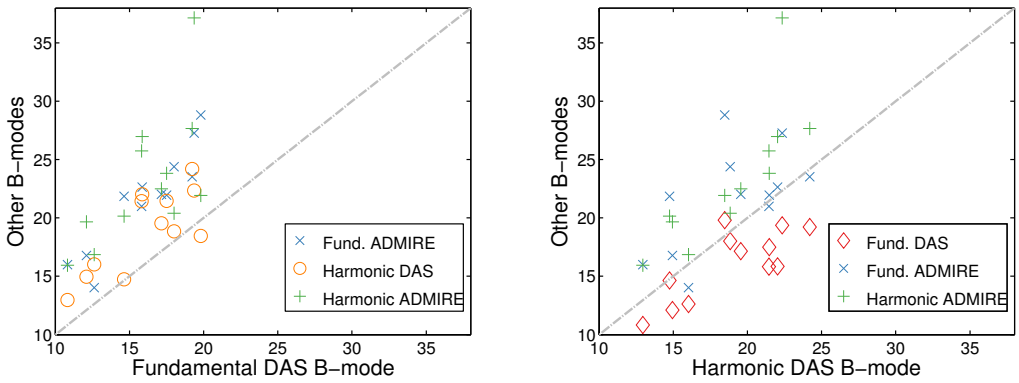

(a) Contrast (dB)

(b) Contrast (dB)

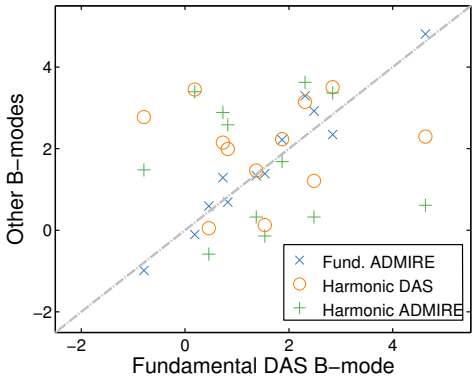

(c) CNR (dB)

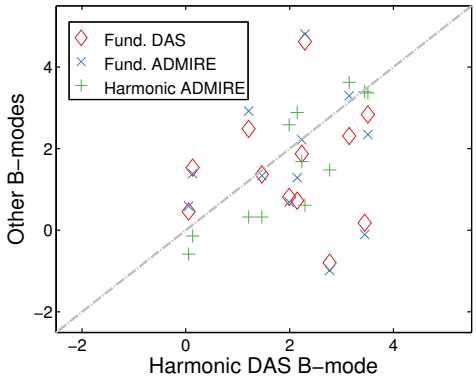

(d) CNR (dB)

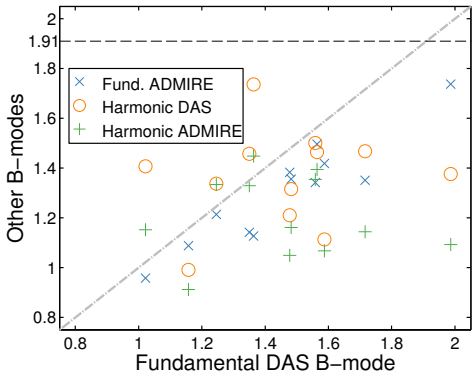

(e) sSNR

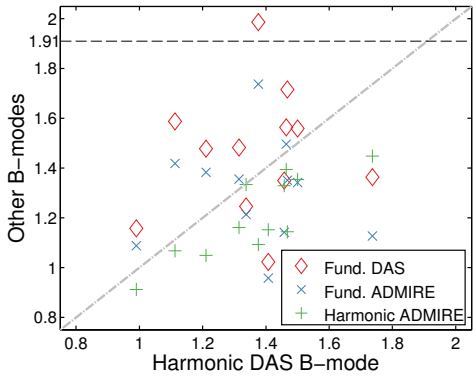

(f) sSNR

Figure 8.8: Contrast, CNR and sSNR comparison, relative to: (a), (c) and (e) fundamental DAS B-mode, (b), (d) and (f) harmonic DAS B-mode. There are 12 realizations of *in vivo* kidney scan data acquired from patients undergoing biopsy and cryoablation.

8.4.2 Assessment of Tissue Boundary Delineation

We demonstrate examples of *in vivo* kidney boundary images reconstructed after applying DAS, ADMIRE and SLSC in fundamental and harmonic implementations, along with estimates of the transition length at axial edge by fitting a sigmoid function, as shown in Figs. 8.9 and 8.10. Figs 8.11 and 8.12 are the matched *in vivo* kidney boundary images of Figs. 8.9 and 8.10 to estimate the transition length at lateral edge of the kidney boundary. Fig. 8.13 shows measured τ values in box plots for fundamental and 2^{nd} harmonic data reconstructed from DAS, ADMIRE and SLSC beamforming. Table 8.3 also summarizes the estimated τ values.

Based on these findings, ADMIRE has the shortest transition length axially and laterally for both fundamental and harmonic cases, suggesting that ADMIRE provides better axial and lateral boundary delineation than DAS and SLSC beamforming. When comparing the τ values between fundamental and harmonic implementations, we also noticed that it is beneficial to use harmonic imaging data.

8.5 Discussion and Conclusions

In this study, we evaluated fundamental and harmonic ADMIRE images using nearly-matched *in vivo* kidney data acquired from patients undergoing biopsy. Based on the findings, as expected, harmonic imaging improves image quality in both contrast and CNR compared to fundamental B-mode. ADMIRE improves contrast over +5 dB relative to fun-

Table 8.3: Measured τ Values at Axial/Lateral Edges of Kidney Boundaries (mm)

Beamforming	**Edge**	**Fundamental**	**2^{nd} Harmonic**
DAS	axial	2.09 ± 1.19	1.24 ± 0.57
	lateral	1.49 ± 0.48	0.88 ± 0.44
ADMIRE	axial	0.32 ± 0.36	0.24 ± 0.07
	lateral	0.55 ± 0.16	0.28 ± 0.15
SLSC	axial	1.75 ± 1.05	0.61 ± 0.48
	lateral	1.51 ± 0.80	0.58 ± 0.44

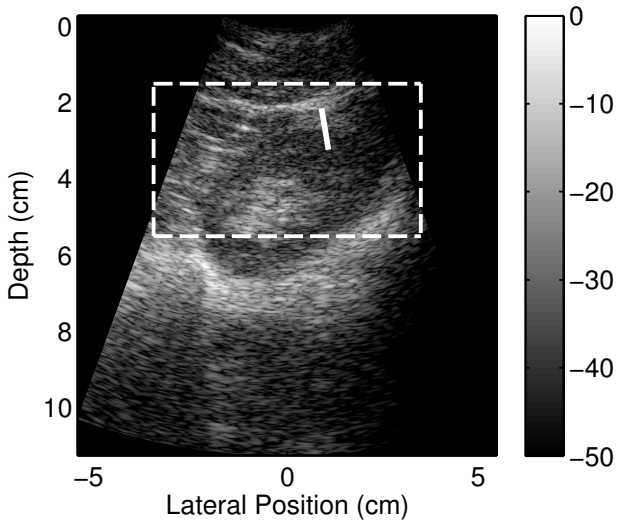

(a) Fundamental B-mode (DAS)

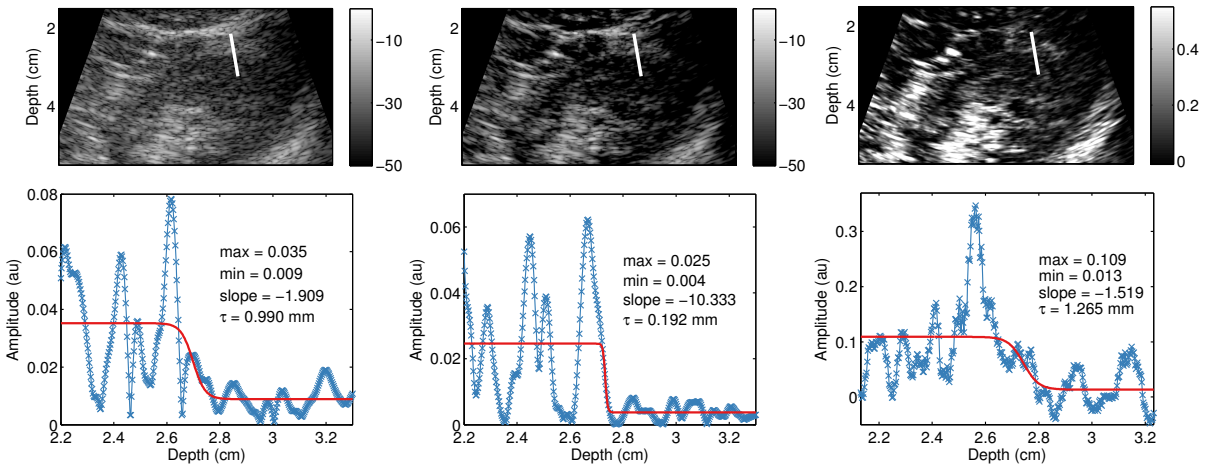

(b) DAS (c) ADMIRE (d) SLSC

Figure 8.9: An example of *in vivo* kidney boundary images reconstructed after applying DAS, ADMIRE and SLSC in fundamental implementation, along with estimates of the transition length by fitting a sigmoid function. (a) Fundamental B-mode image is demonstrated with a vertical solid line used to estimate the transition length at axial edge of the kidney boundary. The figure also includes a dashed rectangular box, where (b) DAS, (c) ADMIRE and (d) SLSC images are zoomed in. The (b), (c) and (d) figures also show sigmoid functions after fitting.

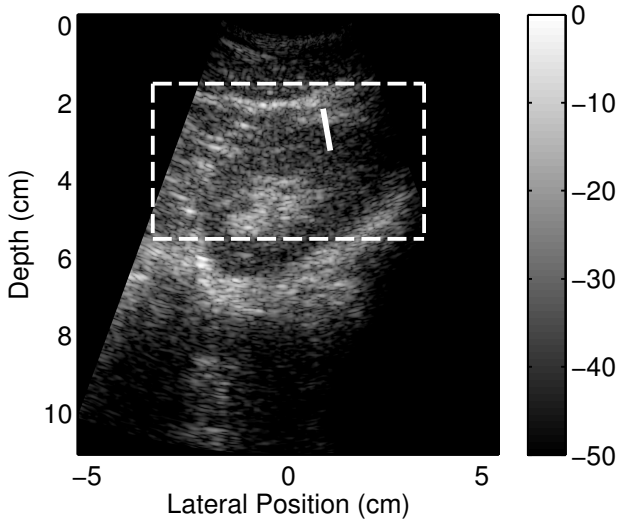

(a) Harmonic B-mode (DAS)

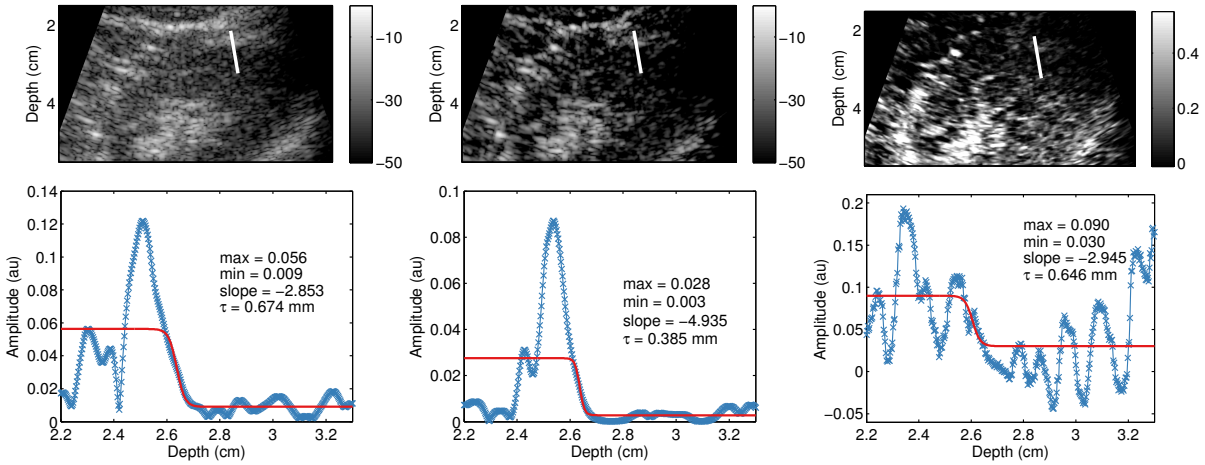

(b) DAS (c) ADMIRE (d) SLSC

Figure 8.10: An example of *in vivo* kidney boundary images reconstructed after applying DAS, ADMIRE and SLSC in harmonic implementation, along with estimates of the transition length by fitting a sigmoid function. (a) Harmonic B-mode image is demonstrated with a vertical solid line used to estimate the transition length at axial edge of the kidney boundary. The figure also includes a dashed rectangular box, where (b) DAS, (c) ADMIRE and (d) SLSC images are zoomed in. The (b), (c) and (d) figures also show sigmoid functions after fitting.

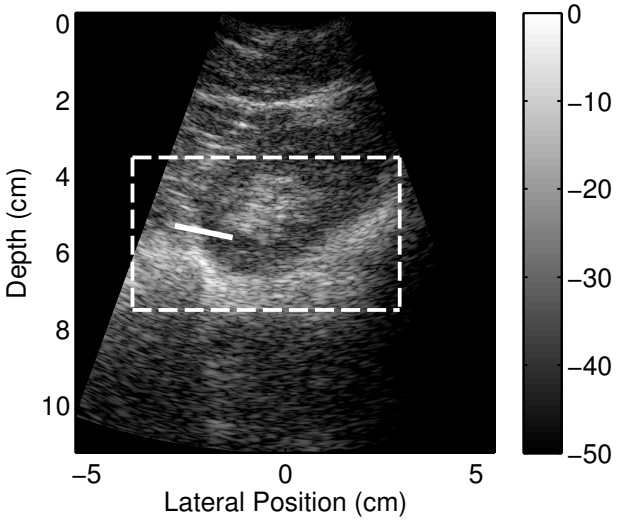

(a) Fundamental B-mode (DAS)

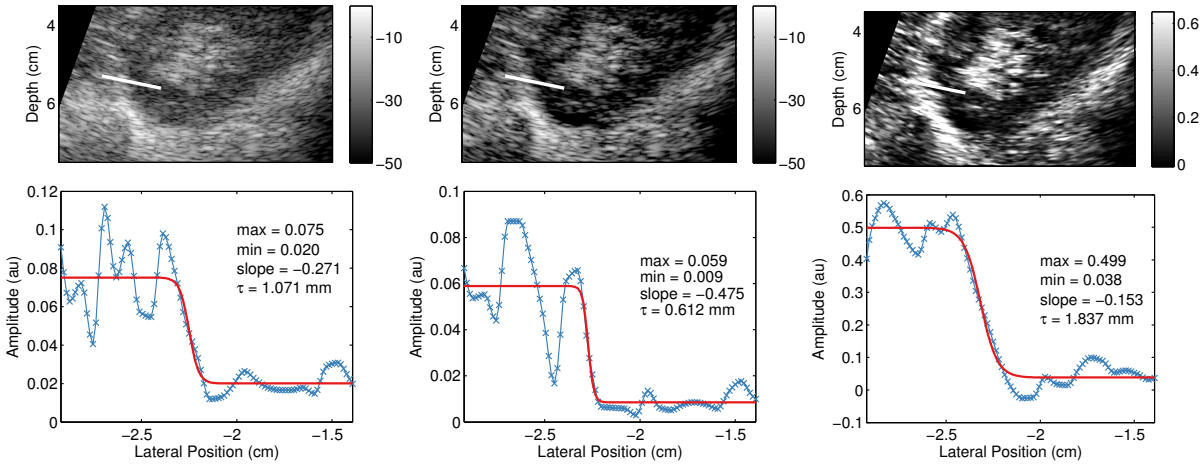

(b) DAS (c) ADMIRE (d) SLSC

Figure 8.11: The matched *in vivo* kidney boundary images of Fig. 8.6 to estimate the transition length at lateral edge of the kidney boundary. (a) Fundamental B-mode image is demonstrated with a horizontal solid line used to estimate the transition length at lateral edge of the kidney boundary. The figure also includes a dashed rectangular box, where (b) DAS, (c) ADMIRE and (d) SLSC images are zoomed in. The (b), (c) and (d) figures also show sigmoid functions after fitting.

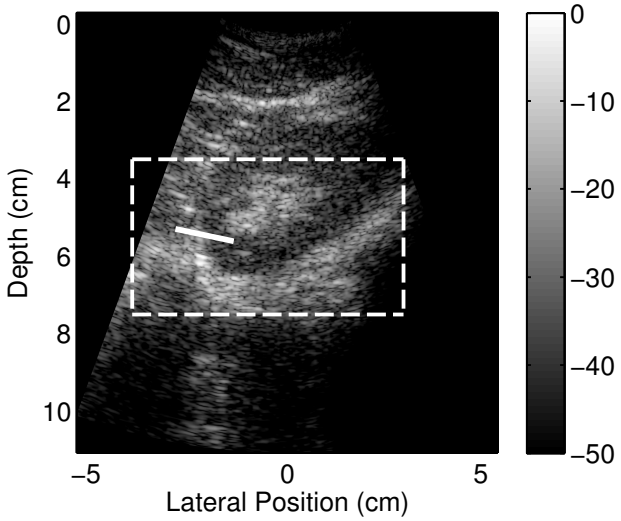

(a) Harmonic B-mode (DAS)

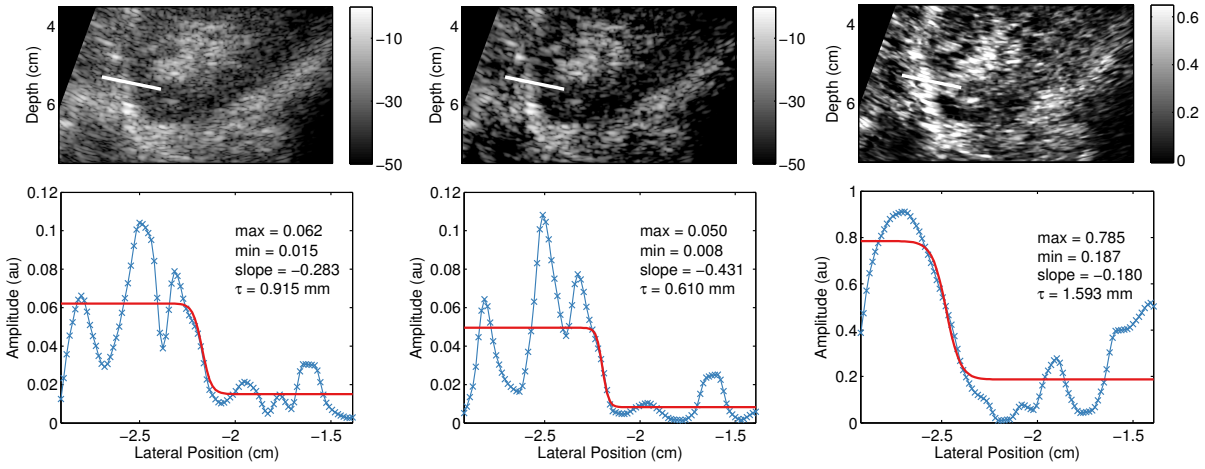

(b) DAS (c) ADMIRE (d) SLSC

Figure 8.12: The matched *in vivo* kidney boundary images of Fig. 8.7 to estimate the transition length at lateral edge of the kidney boundary. (a) Harmonic B-mode image is demonstrated with a horizontal solid line used to estimate the transition length at lateral edge of the kidney boundary. The figure also includes a dashed rectangular box, where (b) DAS, (c) ADMIRE and (d) SLSC images are zoomed in. The (b), (c) and (d) figures also show sigmoid functions after fitting.

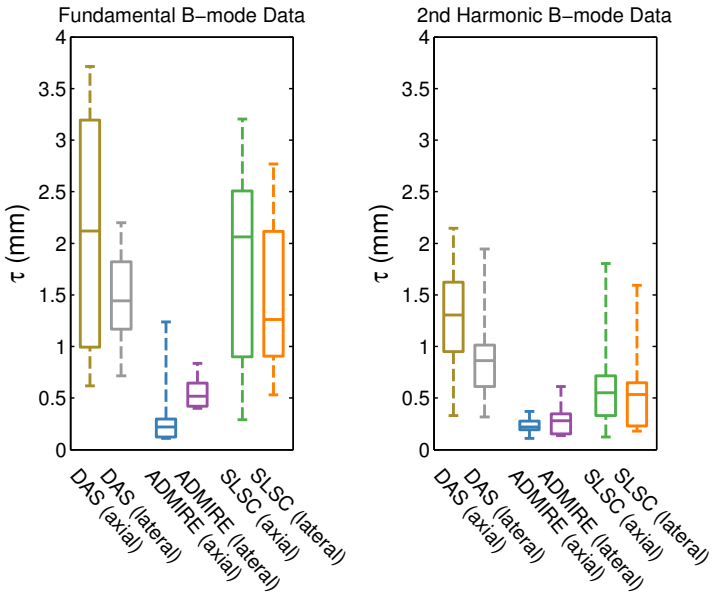

Figure 8.13: Results of measured τ values in box plots for fundamental and 2^{nd} harmonic data after applying DAS, ADMIRE and SLSC beamforming. The τ values are also estimated at axial and lateral edges at the kidney boundary.

damental DAS, and boosts +4 dB in harmonic imaging data. The improvements in the *in vivo* kidney data may increase when deliberately selecting tunable parameter of λ when implementing ADMIRE.

We also quantified the sharpness of lateral and axial edges at the tissue boundary of the kidney using the same data set. The findings indicate that uncompressed envelope data after applying ADMIRE provide the shortest transition length at axial and lateral edges for both fundamental and harmonic imaging. It could thus be suggested that ADMIRE images may provide better boundary delineation than DAS and SLSC images. The qualitative comparison using images demonstrated in Figs. 8.9 to 8.12 shows consistent results. It it crucial to delineate boundaries in percutaneous biopsy guidance and such applications. Future work is required to investigate correlated aspects between contrast, contrast-to-noise ratio measurements and the sharpness of tissue boundaries using data acquired from contrast target phantoms or *in vivo* scan.

Chapter 9

CONCLUSIONS AND FUTURE WORK

This dissertation has identified several factors that are important in understanding the ability and limitations of the model-based beamforming method, ADMIRE. The basis of ADMIRE is a decomposition of received aperture domain signals using a physical model followed by reconstruction using only model signals from the region of interest. In fact, ADMIRE has demonstrated an ability to suppress acoustic clutter and significantly improve ultrasound image quality in challenging high clutter environments. However, some limitations associated with ADMIRE's performance and efficiency are identified.

First, because recent studies reveal that both reverberation (or multipath scattering) and wavefront aberration are primary sources of *in vivo* image degradation [7, 112], this dissertation includes the first qualitative and quantitative measurements of these two effects in ultrasound imaging using ADMIRE. However, the evaluated *in vivo* data is restricted to abdominal imaging, and it is well-known that levels of aberration are different in other scenarios. It can be suggested that this study may be applied to other research fields of medical ultrasound, including breast imaging and echocardiography, thus further adding to the clinical value of the ADMIRE algorithm.

Second, this dissertation addresses the recent interest in high-speed imaging with full field insonification sequences (e.g., plane wave imaging). Plane wave imaging allows for much higher frame rates to be achieved compared to conventional transmit focus which acquires single lines at a time. However, due to the lack of focusing on transmit, plane wave images are often of poor quality. The images included in the dissertation indicate that ADMIRE can be adapted to full-field insonification sequences to effectively improve plane wave image quality. An implication of this is the possibility that ADMIRE may play an important role in providing improved image quality when imaging non-stationary

structures, such as with echocardiography and blood flow imaging. Such applications typically require higher frame rates for maintaining image quality and real-time capabilities, suggesting more benefits using plane wave imaging.

Third, this dissertation demonstrates a computationally-efficient approach for accelerating the ADMIRE algorithm towards a real-time implementation, enabling use of the algorithm in clinical applications. It is worth noting that the ability to provide a real-time high quality ultrasound is crucial for practical use in a clinical setting.

Fourth, this dissertation proposes a new quality metric for evaluating beamformer performance, called contrast ratio dynamic range. The metric quantifies dynamic range as the longest continuous duration along the intrinsic contrast line. The evaluated results demonstrate that conventional DAS beamforming outperforms most novel beamformers, except for ADMIRE using higher degrees of freedom. These findings indicate ultrasound beamforming suffers from limited dynamic range [105]. Thus, it is also important to provide high dynamic range ultrasound imaging [184, 185], especially in cardiac imaging in order to visualize endocardial borders. It may be possible to increase the dynamic range of ADMIRE with deliberate selection of tuning parameters or more sophisticated approaches applied during model-fit, allowing for further increased potential of ADMIRE used in the clinic.

Lastly, this dissertation assesses ADMIRE's clinical utility using *in vivo* kidney fundamental and harmonic B-mode data. The data was acquired from patients undergoing biopsy and cryoablation using a dedicated clinical platform. The demonstrated results are promising, because ADMIRE provides better tissue boundary delineation compared to conventional B-mode and SLSC imaging. This work also showed that ADMIRE suppresses acoustic clutter and significantly improves *in vivo* B-mode image quality, especially in contrast. These results, however, should not yet be generalized, given the limited scope of this study.

However, many problems and challenges remain. To increase ADMIRE performance,

tunable parameters (α and λ) in the model decomposition should be deliberately and adaptively selected as a function of clutter level in the imaging field. In the preceding chapters, the dissertation shows that higher degrees of freedom are required to increase performance when implementing ADMIRE in higher clutter environments. Furthermore, tool development is pivotal in order to adaptively tune the degrees of freedom (i.e., λ) when implementing ADMIRE. The tool could also serve as an indicator of the detected clutter level of each patient and their respective organs and tissues. The collected data may be applied to scientific or medical research field to assess how clutter level may be correlated with tissue anatomical structure and disease.

It is also challenging to implement ADMIRE in real-time due to its high computational requirements, which are caused by the large model and the non-linear elastic-net regularization. Computationally-efficient methods are addressed in Chapter 6, which examines the reduction of the ADMIRE algorithm's computational complexity. Several potential approaches to implement ADMIRE in real-time should be considered, including: 1) the porting of the ADMIRE algorithm to GPUs, similar to others [186, 187], 2) integration of state-of-the art machine learning methods, such as deep learning algorithms, into ADMIRE [141], while leaving the original framework of ADMIRE intact.

Furthermore, given the growing demand for 3D ultrasound imaging, ADMIRE should also process 3D imaging data. To this end, a first step would be to develop a physical model on 2-D matrix arrays to extend the ADMIRE algorithm for use in a 3D field of imaging. The model for 2-D matrix array transducers would be assessed using simulated data for validation, as described in Chapter 2. ADMIRE would also have to accommodate a drastic increase in computational complexity that would result from increasing the number of model predictors in the implementation of ADMIRE on 3D imaging data. However, 3D images reconstructed using ADMIRE may have significant implications for further understanding of how ultrasound *in vivo* B-mode image degradation occurs.

All of the above problems and challenges must be explored in order to fully realize the

benefits and utilities of ADMIRE in challenging acoustic clutter suppression and providing improved image quality, especially when scanning ”difficult-to-image” patients who are usually obese. The most important objective, however, is to provide ADMIRE B-mode images in a clinical setting (in real-time, if possible), to enable clinicians and sonographers to directly evaluate and examine how the resulting ADMIRE images show improvements compared to conventional B-mode images, in terms of visibility and detectability of target lesions or a biopsy needle. A future goal may be the development of a soft hook to process ADMIRE images, together with the matched DAS B-mode images.

There are various applications of interest for the use of ADMIRE. ADMIRE may be a robust tool for use in passive cavitation imaging and for identifying scattering locations where cavitation emission is passively received. Passive cavitation imaging has been used in the field of therapeutic ultrasound, including high-intensity focused ultrasound (HIFU), focused ultrasound (FUS) and ultrasound mediated localized drug delivery [188]. Another possibility may be the application of post-ADMIRE decluttered channel data to power Doppler imaging for the detection of blood flow. In related areas of medical imaging modality, the ADMIRE algorithm may also be applicable to the data of photoacoustic imaging or optical coherence tomography (OCT).

One of main objectives of this dissertation is to thoroughly investigate the effectiveness, and to identify the inefficiencies of this model-based beamforming algorithm. The author believes that the results and proposed solutions presented in this dissertation will be referred to and utilized in future studies related to the provision of decluttered ultrasound images in a real clinical setting.

BIBLIOGRAPHY

[1] M. E. Anderson and G. E. Trahey, "A seminar on k-space applied to medical ultrasound," *Department of Biomedical Engineering, Duke University*, 2000.

[2] J. J. Dahl and N. M. Sheth, "Reverberation clutter from subcutaneous tissue layers: Simulation and in vivo demonstrations," *Ultrasound in medicine & biology*, vol. 40, no. 4, pp. 714–726, 2014.

[3] J. T. Bushberg and J. M. Boone, *The essential physics of medical imaging*. Lippincott Williams & Wilkins, 2011.

[4] B. Byram and J. Shu, "Pseudononlinear ultrasound simulation approach for reverberation clutter," *Journal of Medical Imaging*, vol. 3, no. 4, pp. 046 005–046 005, 2016.

[5] T. L. Szabo, *Diagnostic ultrasound imaging: inside out*. Academic Press, 2004.

[6] W. M. Marks, *Ultrasound: A Practical Approach*. CreateSpace North Carolina, 2012.

[7] G. Pinton, G. E. Trahey, and J. J. Dahl, "Erratum: Sources of image degradation in fundamental and harmonic ultrasound imaging using nonlinear, full-wave simulations," *Ultrasonics, Ferroelectrics, and Frequency Control, IEEE Transactions on*, vol. 58, no. 6, pp. 1272–1283, 2011.

[8] J. J. Dahl, D. Hyun, Y. Li, M. Jakovljevic, M. A. Bell, W. J. Long, N. Bottenus, V. Kakkad, and G. E. Trahey, "Coherence beamforming and its applications to the difficult-to-image patient," in *Ultrasonics Symposium (IUS), 2017 IEEE International*. IEEE, 2017, pp. 1–10.

[9] P. T. James, R. Leach, E. Kalamara, and M. Shayeghi, "The worldwide obesity epidemic," *Obesity research*, vol. 9, no. S11, pp. 228S–233S, 2001.

[10] T. Bhurosy and R. Jeewon, "Overweight and obesity epidemic in developing countries: a problem with diet, physical activity, or socioeconomic status?" *The Scientific World Journal*, vol. 2014, 2014.

[11] C. L. Ogden, M. D. Carroll, B. K. Kit, and K. M. Flegal, "Prevalence of childhood and adult obesity in the united states, 2011-2012," *Jama*, vol. 311, no. 8, pp. 806–814, 2014.

[12] K. A. Smith and H. S. Kim, "Interventional radiology and image-guided medicine: interventional oncology," in *Seminars in oncology*, vol. 38, no. 1. Elsevier, 2011, pp. 151–162.

[13] S. T. Kee, D. C. Madoff, and R. Murthy, *Clinical Interventional Oncology*. Elsevier Health Sciences, 2013.

[14] T. G. Nyland, J. S. Mattoon, E. Herrgesell, and E. Wisner, "Ultrasound-guided biopsy," *Small Animal Diagnostic Ultrasound*, pp. 30–48, 2002.

[15] R. S. Cobbold, *Foundations of biomedical ultrasound*. Oxford University Press on Demand, 2007.

[16] J. W. Goodman, *Introduction to Fourier optics*. Roberts and Company Publishers, 2005.

[17] J. A. Jensen and N. B. Svendsen, "Calculation of pressure fields from arbitrarily shaped, apodized, and excited ultrasound transducers," *Ultrasonics, Ferroelectrics, and Frequency Control, IEEE Transactions on*, vol. 39, no. 2, pp. 262–267, 1992.

[18] J. A. Jensen, "Field: A program for simulating ultrasound systems," in *10th Nordic-Baltic Conference on Biomedical Imaging, Vol. 4, Supplement 1, Part 1: 351–353*, 1996.

[19] M. Patterson and F. Foster, "The improvement and quantitative assessment of b-mode images produced by an annular array/cone hybrid," *Ultrasonic Imaging*, vol. 5, no. 3, pp. 195–213, 1983.

[20] P. F. Stetson, F. G. Sommer, and A. Macovski, "Lesion contrast enhancement in medical ultrasound imaging," *IEEE transactions on medical imaging*, vol. 16, no. 4, pp. 416–425, 1997.

[21] R. N. Bracewell and R. N. Bracewell, *The Fourier transform and its applications*. McGraw-Hill New York, 1986, vol. 31999.

[22] O. T. Von Ramm and S. W. Smith, "Beam steering with linear arrays," *Biomedical Engineering, IEEE Transactions on*, no. 8, pp. 438–452, 1983.

[23] J. A. Jensen, S. I. Nikolov, K. L. Gammelmark, and M. H. Pedersen, "Synthetic aperture ultrasound imaging," *Ultrasonics*, vol. 44, pp. e5–e15, 2006.

[24] R. Rohling, A. Gee, and L. Berman, "Three-dimensional spatial compounding of ultrasound images," *Medical Image Analysis*, vol. 1, no. 3, pp. 177–193, 1997.

[25] V. Behar, D. Adam, and Z. Friedman, "A new method of spatial compounding imaging," *Ultrasonics*, vol. 41, no. 5, pp. 377–384, 2003.

[26] M. Tanter and M. Fink, "Ultrafast imaging in biomedical ultrasound," *IEEE transactions on ultrasonics, ferroelectrics, and frequency control*, vol. 61, no. 1, pp. 102–119, 2014.

[27] M. Tanter, J. Bercoff, L. Sandrin, and M. Fink, "Ultrafast compound imaging for 2-d motion vector estimation: Application to transient elastography," *IEEE transactions*

on ultrasonics, ferroelectrics, and frequency control, vol. 49, no. 10, pp. 1363–1374, 2002.

[28] J. A. Jensen, S. I. Nikolov, C. Alfred, and D. Garcia, "Ultrasound vector flow imagingpart i: Sequential systems," *IEEE transactions on ultrasonics, ferroelectrics, and frequency control*, vol. 63, no. 11, pp. 1704–1721, 2016.

[29] ——, "Ultrasound vector flow imagingpart ii: Parallel systems," *IEEE transactions on ultrasonics, ferroelectrics, and frequency control*, vol. 63, no. 11, pp. 1722–1732, 2016.

[30] R. L. Tutwiler, "Ultrasonic beamforming architectures," in *Medical Imaging'98*. International Society for Optics and Photonics, 1998, pp. 43–54.

[31] K. E. Thomenius, "Evolution of ultrasound beamformers," in *Ultrasonics Symposium, 1996. Proceedings., 1996 IEEE*, vol. 2. IEEE, 1996, pp. 1615–1622.

[32] B. D. Steinberg, "Digital beamforming in ultrasound," *Ultrasonics, Ferroelectrics, and Frequency Control, IEEE Transactions on*, vol. 39, no. 6, pp. 716–721, 1992.

[33] J. Ma, K. Karadayi, M. Ali, and Y. Kim, "Software-based ultrasound phase rotation beamforming on multi-core dsp," in *Ultrasonics Symposium (IUS), 2011 IEEE International*. IEEE, 2011, pp. 503–506.

[34] B. Y. Yiu, I. K. Tsang, and C. Alfred, "Real-time gpu-based software beamformer designed for advanced imaging methods research," in *Ultrasonics Symposium (IUS), 2010 IEEE*. IEEE, 2010, pp. 1920–1923.

[35] R. E. Daigle, "Ultrasound imaging system with pixel oriented processing," May 12 2015, uS Patent 9,028,411.

[36] K. Karadayi, C. Lee, and Y. Kim, "Software-based ultrasound beamforming on multi-core dsps," in *IEEE International Ultrasonics Symposium*, 2011, pp. 503–506.

[37] T. Y. Phuong and J.-G. Lee, "Software based ultrasound b-mode/beamforming optimization on gpu and its performance prediction," in *High Performance Computing (HiPC), 2014 21st International Conference on*. IEEE, 2014, pp. 1–10.

[38] M. E. Anderson and G. E. Trahey, "The direct estimation of sound speed using pulse–echo ultrasound," *The Journal of the Acoustical Society of America*, vol. 104, no. 5, pp. 3099–3106, 1998.

[39] M. Anderson, M. McKeag, and G. Trahey, "The impact of sound speed errors on medical ultrasound imaging," *The Journal of the Acoustical Society of America*, vol. 107, no. 6, pp. 3540–3548, 2000.

[40] S. Flax and M. O'Donnell, "Phase-aberration correction using signals from point reflectors and diffuse scatterers: Basic principles," *Ultrasonics, Ferroelectrics, and Frequency Control, IEEE Transactions on*, vol. 35, no. 6, pp. 758–767, 1988.

[41] B. Byram and M. Jakovljevic, "Ultrasonic multipath and beamforming clutter reduction: a chirp model approach," *Ultrasonics, Ferroelectrics, and Frequency Control, IEEE Transactions on*, vol. 61, no. 3, pp. 428–440, 2014.

[42] M. O'Donnell and S. Flax, "Phase aberration measurements in medical ultrasound: human studies," *Ultrasonic Imaging*, vol. 10, no. 1, pp. 1–11, 1988.

[43] M. Karaman, A. Atalar, H. Köymen, and M. O'Donnell, "A phase aberration correction method for ultrasound imaging," *Ultrasonics, Ferroelectrics, and Frequency Control, IEEE Transactions on*, vol. 40, no. 4, pp. 275–282, 1993.

[44] D. L. Liu and R. C. Waag, "Correction of ultrasonic wavefront distortion using backpropagation and a reference waveform method for time-shift compensation," *The Journal of the Acoustical Society of America*, vol. 96, no. 2, pp. 649–660, 1994.

[45] L. M. Hinkelman, D.-L. Liu, R. C. Waag, Q. Zhu, and B. D. Steinberg, "Measurement and correction of ultrasonic pulse distortion produced by the human breast," *The Journal of the Acoustical Society of America*, vol. 97, no. 3, pp. 1958–1969, 1995.

[46] M. Tabei, T. D. Mast, and R. C. Waag, "Simulation of ultrasonic focus aberration and correction through human tissue," *The Journal of the Acoustical Society of America*, vol. 113, no. 2, pp. 1166–1176, 2003.

[47] J. J. Dahl, D. Guenther, G. E. Trahey *et al.*, "Adaptive imaging and spatial compounding in the presence of aberration," *Ultrasonics, Ferroelectrics, and Frequency Control, IEEE Transactions on*, vol. 52, no. 7, pp. 1131–1144, 2005.

[48] J. J. Dahl, S. McAleavey, G. F. Pinton, M. S. Soo, G. E. Trahey *et al.*, "Adaptive imaging on a diagnostic ultrasound scanner at quasi real-time rates," *Ultrasonics, Ferroelectrics, and Frequency Control, IEEE Transactions on*, vol. 53, no. 10, pp. 1832–1843, 2006.

[49] J. C. Tillett, J. P. Astheimer, and R. C. Waag, "A model of distributed phase aberration for deblurring phase estimated from scattering," *Ultrasonics, Ferroelectrics, and Frequency Control, IEEE Transactions on*, vol. 57, no. 1, pp. 214–228, 2010.

[50] B. Byram, "Ultrasonic reverberation and off-axis clutter suppression using aperture domain signal decomposition," in *SPIE Medical Imaging*. International Society for Optics and Photonics, 2013, pp. 86 750T–86 750T.

[51] T. Christopher, "Finite amplitude distortion-based inhomogeneous pulse echo ultrasonic imaging," *Ultrasonics, Ferroelectrics, and Frequency Control, IEEE Transactions on*, vol. 44, no. 1, pp. 125–139, 1997.

[52] B. Ward, A. Baker, and V. Humphrey, "Nonlinear propagation applied to the im-

provement of resolution in diagnostic medical ultrasound," *The Journal of the Acoustical Society of America*, vol. 101, no. 1, pp. 143–154, 1997.

[53] M. A. Averkiou, D. N. Roundhill, and J. E. Powers, "A new imaging technique based on the nonlinear properties of tissues," in *Ultrasonics Symposium, 1997. Proceedings., 1997 IEEE*, vol. 2. IEEE, 1997, pp. 1561–1566.

[54] T. Muir and E. Carstensen, "Prediction of nonlinear acoustic effects at biomedical frequencies and intensities," *Ultrasound in medicine & biology*, vol. 6, no. 4, pp. 345–357, 1980.

[55] H. Starritt, F. Duck, A. Hawkins, and V. Humphrey, "The development of harmonic distortion in pulsed finite-amplitude ultrasound passing through liver," *Physics in medicine and biology*, vol. 31, no. 12, p. 1401, 1986.

[56] V. F. Humphrey, "Nonlinear propagation in ultrasonic fields: measurements, modelling and harmonic imaging," *Ultrasonics*, vol. 38, no. 1, pp. 267–272, 2000.

[57] A. Anvari, F. Forsberg, and A. E. Samir, "A primer on the physical principles of tissue harmonic imaging," *Radiographics*, vol. 35, no. 7, pp. 1955–1964, 2015.

[58] M. Fink, "Time reversal of ultrasonic fields. i. basic principles," *Ultrasonics, Ferroelectrics, and Frequency Control, IEEE Transactions on*, vol. 39, no. 5, pp. 555–566, 1992.

[59] M. Fink, D. Cassereau, A. Derode, C. Prada, P. Roux, M. Tanter, J.-l. Thomas, and F. Wu, "Time-reversed acoustics," *Reports on progress in Physics*, vol. 63, no. 12, p. 1933, 2000.

[60] B. A. Angelsen and R. Hansen, "7a-1 surf imaging-a new method for ultrasound contrast agent imaging," in *Ultrasonics Symposium, 2007. IEEE*. IEEE, 2007, pp. 531–541.

[61] S. E. Masoy, O. Standal, P. Nasholm, T. F. Johansen, B. Angelsen, and R. Hansen, "Surf imaging: In vivo demonstration of an ultrasound contrast agent detection technique," *Ultrasonics, Ferroelectrics, and Frequency Control, IEEE Transactions on*, vol. 55, no. 5, pp. 1112–1121, 2008.

[62] S. P. Näsholm, R. Hansen, S.-E. Måsøy, T. F. Johansen, and B. A. Angelsen, "Transmit beams adapted to reverberation noise suppression using dual-frequency surf imaging," *Ultrasonics, Ferroelectrics, and Frequency Control, IEEE Transactions on*, vol. 56, no. 10, pp. 2124–2133, 2009.

[63] S. P. Näsholm, R. Hansen, and B. A. Angelsen, "Post-processing enhancement of reverberation-noise suppression in dual-frequency surf imaging," *Ultrasonics, Ferroelectrics, and Frequency Control, IEEE Transactions on*, vol. 58, no. 2, pp. 338–348, 2011.

[64] S. P. Nasholm and B. A. Angelsen, "Surf imaging beams in an aberrative medium: generation and postprocessing enhancement," *Ultrasonics, Ferroelectrics, and Frequency Control, IEEE Transactions on*, vol. 59, no. 11, 2012.

[65] J. M. Rau, S.-E. Måsøy, R. Hansen, B. Angelsen, and T. A. Tangen, "Methods for reverberation suppression utilizing dual frequency band imaging," *The Journal of the Acoustical Society of America*, vol. 134, no. 3, pp. 2313–2325, 2013.

[66] M. Lediju, G. E. Trahey, B. C. Byram, J. J. Dahl *et al.*, "Short-lag spatial coherence of backscattered echoes: imaging characteristics," *Ultrasonics, Ferroelectrics, and Frequency Control, IEEE Transactions on*, vol. 58, no. 7, pp. 1377–1388, 2011.

[67] R. Mallart and M. Fink, "The van cittert–zernike theorem in pulse echo measurements," *The Journal of the Acoustical Society of America*, vol. 90, no. 5, pp. 2718–2727, 1991.

[68] M. A. L. Bell, J. J. Dahl, and G. E. Trahey, "Resolution and brightness characteristics of short-lag spatial coherence (slsc) images," *IEEE transactions on ultrasonics, ferroelectrics, and frequency control*, vol. 62, no. 7, pp. 1265–1276, 2015.

[69] B. Byram, K. Dei, J. Tierney, and D. Dumont, "A model and regularization scheme for ultrasonic beamforming clutter reduction," *Ultrasonics, Ferroelectrics, and Frequency Control, IEEE Transactions on*, vol. 62, no. 11, pp. 1913–1927, 2015.

[70] B. Byram, K. Dei, and D. Dumont, "An improved acoustic clutter model and direct in vivo assessment of off-axis and multipath clutter energy in the liver," in *Ultrasonics Symposium (IUS), 2014 IEEE International*. IEEE, 2014, pp. 531–534.

[71] C. H. Seo and J. T. Yen, "Evaluating the robustness of dual apodization with cross-correlation," *Ultrasonics, Ferroelectrics, and Frequency Control, IEEE Transactions on*, vol. 56, no. 2, pp. 291–303, 2009.

[72] J. Shin and J. T. Yen, "Synergistic enhancements of ultrasound image contrast with a combination of phase aberration correction and dual apodization with cross-correlation," *Ultrasonics, Ferroelectrics, and Frequency Control, IEEE Transactions on*, vol. 59, no. 9, 2012.

[73] I. Trots, "Mutually orthogonal golay complementary sequences in synthetic aperture imaging systems," *Archives of Acoustics*, vol. 40, no. 2, pp. 283–289, 2015.

[74] J. F. Synnevåg, A. Austeng, and S. Holm, "Benefits of minimum-variance beamforming in medical ultrasound imaging," *Ultrasonics, Ferroelectrics, and Frequency Control, IEEE Transactions on*, vol. 56, no. 9, pp. 1868–1879, 2009.

[75] A. Rabinovich, Z. Friedman, and A. Feuer, "Multi-line acquisition with minimum variance beamforming in medical ultrasound imaging," *Ultrasonics, Ferroelectrics, and Frequency Control, IEEE Transactions on*, vol. 60, no. 12, pp. 2521–2531, 2013.

[76] M. H. Bae and M.-K. Jeong, "A study of synthetic-aperture imaging with virtual source elements in b-mode ultrasound imaging systems," *Ultrasonics, Ferroelectrics, and Frequency Control, IEEE Transactions on*, vol. 47, no. 6, pp. 1510–1519, 2000.

[77] C. Kim, C. Yoon, J.-H. Park, Y. Lee, W. H. Kim, J. M. Chang, B. I. Choi, T.-K. Song, and Y.-M. Yoo, "Evaluation of ultrasound synthetic aperture imaging using bidirectional pixel-based focusing: Preliminary phantom and in vivo breast study," *Biomedical Engineering, IEEE Transactions on*, vol. 60, no. 10, pp. 2716–2724, 2013.

[78] N. Nguyen and R. Prager, "High-resolution ultrasound imaging with unified pixel-based beamforming," 2015.

[79] R. Mallart and M. Fink, "Adaptive focusing in scattering media through sound-speed inhomogeneities: The van cittert zernike approach and focusing criterion," *The Journal of the Acoustical Society of America*, vol. 96, no. 6, pp. 3721–3732, 1994.

[80] K. Hollman, K. Rigby, and M. O'donnell, "Coherence factor of speckle from a multi-row probe," in *Ultrasonics Symposium, 1999. Proceedings. 1999 IEEE*, vol. 2. IEEE, 1999, pp. 1257–1260.

[81] P.-C. Li and M.-L. Li, "Adaptive imaging using the generalized coherence factor," *IEEE transactions on ultrasonics, ferroelectrics, and frequency control*, vol. 50, no. 2, pp. 128–141, 2003.

[82] J. Camacho, M. Parrilla, and C. Fritsch, "Phase coherence imaging," *IEEE transactions on ultrasonics, ferroelectrics, and frequency control*, vol. 56, no. 5, 2009.

[83] J. F. Synnevag, A. Austeng, and S. Holm, "Adaptive beamforming applied to medical ultrasound imaging," *IEEE transactions on ultrasonics, ferroelectrics, and frequency control*, vol. 54, no. 8, 2007.

[84] I. K. Holfort, F. Gran, and J. A. Jensen, "Broadband minimum variance beamforming for ultrasound imaging," *IEEE transactions on ultrasonics, ferroelectrics, and frequency control*, vol. 56, no. 2, pp. 314–325, 2009.

[85] A. Selfridge, G. Kino, and B. Khuri-Yakub, "A theory for the radiation pattern of a narrow-strip acoustic transducer," *Applied Physics Letters*, vol. 37, no. 1, pp. 35–36, 1980.

[86] H. Zou and T. Hastie, "Regularization and variable selection via the elastic net," *Journal of the Royal Statistical Society: Series B (Statistical Methodology)*, vol. 67, no. 2, pp. 301–320, 2005.

[87] R. J. Tibshirani, J. Taylor *et al.*, "Degrees of freedom in lasso problems," *The Annals of Statistics*, vol. 40, no. 2, pp. 1198–1232, 2012.

[88] X. Lv, G. Bi, C. Wan, and M. Xing, "Lv's distribution: principle, implementation, properties, and performance," *IEEE Transactions on Signal Processing*, vol. 59, no. 8, pp. 3576–3591, 2011.

[89] B. Yang, "A study of inverse short-time fourier transform," in *2008 IEEE International Conference on Acoustics, Speech and Signal Processing*, 2008, pp. 3541–3544.

[90] K. Dei and B. Byram, "A robust method for ultrasound beamforming in the presence of off-axis clutter and sound speed variation," *Ultrasonics*, vol. 89, pp. 34–45, 2018.

[91] J. E. Aldrich, "Basic physics of ultrasound imaging," *Critical care medicine*, vol. 35, no. 5, pp. S131–S137, 2007.

[92] J. Synnevag, A. Austeng, and S. Holm, "Minimum variance adaptive beamforming applied to medical ultrasound imaging," in *Proc. IEEE Ultrason. Symp*, vol. 2, no. 3, 2005, pp. 1199–1202.

[93] Z. Wang, J. Li, and R. Wu, "Time-delay-and time-reversal-based robust capon beamformers for ultrasound imaging," *IEEE transactions on medical imaging*, vol. 24, no. 10, pp. 1308–1322, 2005.

[94] B. M. Asl and A. Mahloojifar, "Minimum variance beamforming combined with adaptive coherence weighting applied to medical ultrasound imaging," *IEEE transactions on ultrasonics, ferroelectrics, and frequency control*, vol. 56, no. 9, pp. 1923–1931, 2009.

[95] C. H. Seo and J. Yen, "Sidelobe suppression in ultrasound imaging using dual apodization with cross-correlation," *Ultrasonics, Ferroelectrics, and Frequency Control, IEEE Transactions on*, vol. 55, no. 10, pp. 2198–2210, 2008.

[96] J. H. Sung and J. S. Jeong, "Dual-/tri-apodization techniques for high frequency ultrasound imaging: a simulation study," *Biomedical engineering online*, vol. 13, no. 1, p. 1, 2014.

[97] D. A. Guenther and W. F. Walker, "Optimal apodization design for medical ultrasound using constrained least squares part i: theory," *IEEE transactions on ultrasonics, ferroelectrics, and frequency control*, vol. 54, no. 2, pp. 332–342, 2007.

[98] ——, "Optimal apodization design for medical ultrasound using constrained least squares part ii simulation results," *IEEE transactions on ultrasonics, ferroelectrics, and frequency control*, vol. 54, no. 2, pp. 343–358, 2007.

[99] Z. He, F. Zheng, Y. Ma, H. H. Kim, Q. Zhou, and K. K. Shung, "A sidelobe suppressing near-field beamforming approach for ultrasound array imaging," *The Journal of the Acoustical Society of America*, vol. 137, no. 5, pp. 2785–2790, 2015.

[100] M. K. Jeong and S. J. Kwon, "Estimation of side lobes in ultrasound imaging systems," *Biomedical Engineering Letters*, vol. 5, no. 3, pp. 229–239, 2015.

[101] K. Dei and B. Byram, "The impact of model-based clutter suppression on cluttered, aberrated wavefronts," *IEEE Transactions on Ultrasonics, Ferroelectrics, and Frequency Control*, vol. 64, no. 10, pp. 1450–1464, 2017.

[102] B. Byram, J. Shu, and K. Dei, "Nonlinear beamforming of aperture domain signals," in *Ultrasonics Symposium (IUS), 2015 IEEE International*. IEEE, 2015, pp. 1–6.

[103] R. F. Wagner, S. W. Smith, J. M. Sandrik, and H. Lopez, "Statistics of speckle in ultrasound b-scans," *Sonics and Ultrasonics, IEEE Transactions on*, vol. 30, no. 3, pp. 156–163, 1983.

[104] O. M. H. Rindal, A. Rodriguez-Molares, and A. Austeng, "The dark region artifact in adaptive ultrasound beamforming," in *Ultrasonics Symposium (IUS), 2017 IEEE International*. IEEE, 2017, pp. 1–4.

[105] K. Dei, A. Luchies, and B. Byram, "Contrast ratio dynamic range: A new beamformer performance metric," in *Ultrasonics Symposium (IUS), 2017 IEEE International*. IEEE, 2017, pp. 1–4.

[106] L. L. Foldy, "The multiple scattering of waves. i. general theory of isotropic scattering by randomly distributed scatterers," *Physical Review*, vol. 67, no. 3-4, p. 107, 1945.

[107] R. Chivers, "The scattering of ultrasound by human tissuessome theoretical models," *Ultrasound in medicine & biology*, vol. 3, no. 1, pp. 1–13, 1977.

[108] D. Nicholas, C. Hill, and D. Nassiri, "Evaluation of backscattering coefficients for excised human tissues: principles and techniques," *Ultrasound in Medicine & Biology*, vol. 8, no. 1, pp. 7–15, 1982.

[109] D. Nicholas, "Evaluation of backscattering coefficients for excised human tissues:

results, interpretation and associated measurements," *Ultrasound in Medicine & Biology*, vol. 8, no. 1, pp. 17–28, 1982.

[110] S. Bly, F. Foster, M. Patterson, D. Foster, and J. Hunt, "Artifactual echoes in b-mode images due to multiple scattering," *Ultrasound in medicine & biology*, vol. 11, no. 1, pp. 99–111, 1985.

[111] M. A. Lediju, M. J. Pihl, J. J. Dahl, and G. E. Trahey, "Quantitative assessment of the magnitude, impact and spatial extent of ultrasonic clutter," *Ultrasonic imaging*, vol. 30, no. 3, pp. 151–168, 2008.

[112] J. J. Dahl, M. Jakovljevic, G. F. Pinton, and G. E. Trahey, "Harmonic spatial coherence imaging: an ultrasonic imaging method based on backscatter coherence," *Ultrasonics, Ferroelectrics, and Frequency Control, IEEE Transactions on*, vol. 59, no. 4, pp. 648–659, 2012.

[113] K. Dei and B. Byram, "Model-based clutter suppression in the presence of phase-aberration from in vivo data and simulations," in *Ultrasonics Symposium (IUS), 2015 IEEE International*, Oct 2015, pp. 1–4.

[114] D. L. Liu and R. C. Waag, "Time-shift compensation of ultrasonic pulse focus degradation using least-mean-square error estimates of arrival time," *The Journal of the Acoustical Society of America*, vol. 95, no. 1, pp. 542–555, 1994.

[115] T. Loupas, J. Powers, and R. W. Gill, "An axial velocity estimator for ultrasound blood flow imaging, based on a full evaluation of the doppler equation by means of a two-dimensional autocorrelation approach," *Ultrasonics, Ferroelectrics, and Frequency Control, IEEE Transactions on*, vol. 42, no. 4, pp. 672–688, 1995.

[116] R. C. Gauss, G. E. Trahey, and M. S. Soo, "Wavefront estimation in the human breast." International Society for Optics and Photonics, 2001, pp. 172–181.

[117] J. J. Dahl and T. J. Feehan, "Direction of arrival filters for improved aberration estimation," *Ultrasonic imaging*, vol. 30, no. 1, pp. 1–20, 2008.

[118] J. J. Dahl and G. E. Trahey, "Off-axis scatterer filters for improved aberration measurements," in *Ultrasonics, 2003 IEEE Symposium on*, vol. 2. IEEE, 2003, pp. 1094–1098.

[119] B. Byram and J. Shu, "A pseudo non-linear method for fast simulations of ultrasonic reverberation," in *SPIE Proceedings Vol. 9790: Medical Imaging 2016: Ultrasonic Imaging and Tomography*, 2016.

[120] A. Fernandez, J. J. Dahl, D. M. Dumont, and G. E. Trahey, "Aberration measurement and correction with a high resolution 1.75 d array," in *Ultrasonics Symposium, 2001 IEEE*, vol. 2. IEEE, 2001, pp. 1489–1494.

[121] J. C. Lacefield, W. C. Pilkington, and R. C. Waag, "Distributed aberrators for emulation of ultrasonic pulse distortion by abdominal wall," *Acoustics Research Letters Online*, vol. 3, no. 2, pp. 47–52, 2002.

[122] L. M. Hinkelman, D.-L. Liu, L. A. Metlay, and R. C. Waag, "Measurements of ultrasonic pulse arrival time and energy level variations produced by propagation through abdominal wall," *The Journal of the Acoustical Society of America*, vol. 95, no. 1, pp. 530–541, 1994.

[123] Y. Sumino and R. C. Waag, "Measurements of ultrasonic pulse arrival time differences produced by abdominal wall specimens," *The Journal of the Acoustical Society of America*, vol. 90, no. 6, pp. 2924–2930, 1991.

[124] W. F. Walker and G. E. Trahey, "Aberrator integration error in adaptive imaging," *IEEE transactions on ultrasonics, ferroelectrics, and frequency control*, vol. 44, no. 4, pp. 780–791, 1997.

[125] K. Dei, J. E. Tierney, and B. C. Byram, "Model-based beamforming with plane wave synthesis in medical ultrasound," *Journal of Medical Imaging*, vol. 5, no. 2, p. 027001, 2018.

[126] Q. Ma, Y. Ma, X. Gong, and D. Zhang, "Improvement of tissue harmonic imaging using the pulse-inversion technique," *Ultrasound in medicine & biology*, vol. 31, no. 7, pp. 889–894, 2005.

[127] M. Cikes, L. Tong, G. R. Sutherland, and J. Dhooge, "Ultrafast cardiac ultrasound imaging: technical principles, applications, and clinical benefits," *JACC: Cardiovascular Imaging*, vol. 7, no. 8, pp. 812–823, 2014.

[128] J. Bercoff, "Ultrafast ultrasound imaging," in *Ultrasound imaging-Medical applications*. InTech, 2011.

[129] L. Tong, H. Gao, H. F. Choi, and J. D'hooge, "Comparison of conventional parallel beamforming with plane wave and diverging wave imaging for cardiac applications: A simulation study," *IEEE transactions on ultrasonics, ferroelectrics, and frequency control*, vol. 59, no. 8, pp. 1654–1663, 2012.

[130] J. Udesen, F. Gran, K. L. Hansen, J. A. Jensen, C. Thomsen, and M. B. Nielsen, "High frame-rate blood vector velocity imaging using plane waves: simulations and preliminary experiments," *IEEE transactions on ultrasonics, ferroelectrics, and frequency control*, vol. 55, no. 8, pp. 1729–1743, 2008.

[131] K. Dei, J. Tierney, and B. Byram, "Aperture domain model image reconstruction (ADMIRE) with plane wave synthesis," in *SPIE Medical Imaging 2017: Ultrasonic Imaging and Tomography*, vol. 10139. International Society for Optics and Photonics, 2017, pp. 1 013 911–1 013 911–10.

[132] H. Liebgott, A. Rodriguez-Molares, F. Cervenansky, J. A. Jensen, and O. Bernard,

"Plane-wave imaging challenge in medical ultrasound," in *Ultrasonics Symposium (IUS), 2016 IEEE International*. IEEE, 2016, pp. 1–4.

[133] "Plane-wave Imaging Challenge in Medical UltraSound (PICMUS), IEEE IUS 2016, Tours, France,"
https://www.creatis.insa-lyon.fr/Challenge/IEEE_IUS_2016/, accessed: 2016-09-21.

[134] J. Friedman, T. Hastie, and R. Tibshirani, "Regularization paths for generalized linear models via coordinate descent," *Journal of statistical software*, vol. 33, no. 1, p. 1, 2010.

[135] G. Montaldo, M. Tanter, J. Bercoff, N. Benech, and M. Fink, "Coherent plane-wave compounding for very high frame rate ultrasonography and transient elastography," *IEEE transactions on ultrasonics, ferroelectrics, and frequency control*, vol. 56, no. 3, pp. 489–506, 2009.

[136] J. T. Ylitalo and H. Ermert, "Ultrasound synthetic aperture imaging: monostatic approach," *IEEE transactions on ultrasonics, ferroelectrics, and frequency control*, vol. 41, no. 3, pp. 333–339, 1994.

[137] D. E. T. Romero and G. J. Dolecek, *Digital FIR Hilbert Transformers: Fundamentals and Efficient Design Methods*. INTECH Open Access Publisher, 2012.

[138] M. A. Hassan and Y. M. Kadah, "Digital signal processing methodologies for conventional digital medical ultrasound imaging system," *American Journal of Biomedical Engineering*, vol. 3, no. 1, pp. 14–30, 2013.

[139] C. B. Burckhardt, "Speckle in ultrasound b-mode scans," *Sonics and Ultrasonics, IEEE Transactions on*, vol. 25, no. 1, pp. 1–6, 1978.

[140] Q. Zhou, W. Chen, S. Song, J. R. Gardner, K. Q. Weinberger, and Y. Chen, "A

reduction of the elastic net to support vector machines with an application to GPU computing," in *AAAI*, 2015, pp. 3210–3216.

[141] A. C. Luchies and B. C. Byram, "Deep neural networks for ultrasound beamforming," *IEEE Transactions on Medical Imaging*, vol. PP, no. 99, pp. 1–1, 2018.

[142] K. D. Lindor, C. Bru, R. A. Jorgensen, J. Rakela, J. M. Bordas, J. B. Gross, J. Rodes, D. B. McGill, C. C. Reading, E. M. James *et al.*, "The role of ultrasonography and automatic-needle biopsy in outpatient percutaneous liver biopsy," *Hepatology*, vol. 23, no. 5, pp. 1079–1083, 1996.

[143] M. Ahmed, L. Solbiati, C. L. Brace, D. J. Breen, M. R. Callstrom, J. W. Charboneau, M.-H. Chen, B. I. Choi, T. De Baère, G. D. Dodd III *et al.*, "Image-guided tumor ablation: standardization of terminology and reporting criteriaa 10-year update," *Journal of Vascular and Interventional Radiology*, vol. 25, no. 11, pp. 1691–1705, 2014.

[144] M. Baad, Z. F. Lu, I. Reiser, and D. Paushter, "Clinical significance of US artifacts," *RadioGraphics*, vol. 37, no. 5, pp. 1408–1423, 2017.

[145] P. C. Tay, S. T. Acton, and J. A. Hossack, "A wavelet thresholding method to reduce ultrasound artifacts," *Computerized Medical Imaging and Graphics*, vol. 35, no. 1, pp. 42–50, 2011.

[146] M. A. Ellis, F. Viola, and W. F. Walker, "Super-resolution image reconstruction using diffuse source models," *Ultrasound in medicine & biology*, vol. 36, no. 6, pp. 967–977, 2010.

[147] Y. Yankelevsky, Z. Friedman, and A. Feuer, "Component-based modeling and processing of medical ultrasound signals," *IEEE Transactions on Signal Processing*, vol. 65, no. 21, pp. 5743–5755, 2017.

[148] M. Jakovljevic, S. Hsieh, R. Ali, G. Chau Loo Kung, D. Hyun, and J. J. Dahl, "Local speed of sound estimation in tissue using pulse-echo ultrasound: Model-based approach," *The Journal of the Acoustical Society of America*, vol. 144, no. 1, pp. 254–266, 2018.

[149] K. Dei and B. Byram, "Computationally-efficient model-based clutter suppression with ADMIRE," in *Ultrasonics Symposium (IUS), 2016 IEEE International*. IEEE, 2016, pp. 1–4.

[150] G. B. Arfken and H.-J. Weber, *Mathematical methods for physicists*. Academic Press New York 1970, 1972.

[151] S. S. Bayin, *Essentials of Mathematical Methods in Science and Engineering*. John Wiley & Sons, 2013.

[152] A. Hyvärinen, J. Karhunen, and E. Oja, *Independent Component Analysis. John Willey & Sons*, 2001.

[153] J. Shin and L. Huang, "Spatial prediction filtering of acoustic clutter and random noise in medical ultrasound imaging," *IEEE transactions on medical imaging*, vol. 36, no. 2, pp. 396–406, 2017.

[154] A. C. Luchies and B. C. Byram, "Deep neural networks for ultrasound beamforming," *IEEE transactions on medical imaging*, 2018.

[155] J. Nash, "The singular-value decomposition and its use to solve least-squares problems," *Compact Numerical Methods for Computers: Linear Algebra and Function Minimisation,*, pp. 30–48, 1990.

[156] X. Liu, Z. Wen, and Y. Zhang, "Limited memory block krylov subspace optimization for computing dominant singular value decompositions," *SIAM Journal on Scientific Computing*, vol. 35, no. 3, pp. A1641–A1668, 2013.

[157] A. Hyvärinen and E. Oja, "Independent component analysis: algorithms and applications," *Neural networks*, vol. 13, no. 4-5, pp. 411–430, 2000.

[158] J. Wang and C.-I. Chang, "Independent component analysis-based dimensionality reduction with applications in hyperspectral image analysis," *IEEE transactions on geoscience and remote sensing*, vol. 44, no. 6, pp. 1586–1600, 2006.

[159] J. Shlens, "A tutorial on independent component analysis," *arXiv preprint arXiv:1404.2986*, 2014.

[160] T. Adali, H. Li, M. Novey, and J.-F. Cardoso, "Complex ICA using nonlinear functions," *IEEE Transactions on Signal Processing*, vol. 56, no. 9, pp. 4536–4544, 2008.

[161] J.-F. Cardoso, "Source separation using higher order moments," in *Acoustics, Speech, and Signal Processing, 1989. ICASSP-89., 1989 International Conference on*. IEEE, 1989, pp. 2109–2112.

[162] A. Hyvarinen, "Fast and robust fixed-point algorithms for independent component analysis," *IEEE transactions on Neural Networks*, vol. 10, no. 3, pp. 626–634, 1999.

[163] V. Zarzoso and P. Comon, "Robust independent component analysis by iterative maximization of the kurtosis contrast with algebraic optimal step size," *IEEE Transactions on Neural Networks*, vol. 21, no. 2, pp. 248–261, 2010.

[164] "RobustICA algorithm for independent component analysis," http://www.i3s.unice.fr/~zarzoso/robustica.html, accessed: 2018-04-01.

[165] X.-L. Li and T. Adali, "Independent component analysis by entropy bound minimization," *IEEE Transactions on Signal Processing*, vol. 58, no. 10, pp. 5151–5164, 2010.

[166] ——, "Complex independent component analysis by entropy bound minimization,"

IEEE Transactions on Circuits and Systems I: Regular Papers, vol. 57, no. 7, pp. 1417–1430, 2010.

[167] "Independent component analysis (ICA) by entropy bound minimization (EBM) and entropy rate minimization (ERM)," http://www.mlsp.umbc.edu/ica_ebm.html, accessed: 2018-04-01.

[168] A. Belouchrani, K. Abed-Meraim, J.-F. Cardoso, and E. Moulines, "A blind source separation technique using second-order statistics," *IEEE Transactions on signal processing*, vol. 45, no. 2, pp. 434–444, 1997.

[169] L. Tong, R.-W. Liu, V. C. Soon, and Y.-F. Huang, "Indeterminacy and identifiability of blind identification," *IEEE Transactions on circuits and systems*, vol. 38, no. 5, pp. 499–509, 1991.

[170] B. Byram and J. Shu, "A pseudo non-linear method for fast simulations of ultrasonic reverberation," International Society for Optics and Photonics, pp. 97 900U–97 900U–7, 2016.

[171] O. M. H. Rindal, A. Austeng, H. Torp, S. Holm, and A. Rodriguez-Molares, "The dynamic range of adaptive beamformers," in *Ultrasonics Symposium (IUS), 2016 IEEE International*. IEEE, 2016, pp. 1–4.

[172] B. Rosner, "Fundamentals of biostatistics. 1995," *Duxbury Press: New York*.

[173] K. Dei, A. Luchies, and B. Byram, "ADMIRE applied to fundamental and harmonic data acquired using a modern clinical platform," in *Medical Imaging 2018: Ultrasonic Imaging and Tomography*, vol. 10580. International Society for Optics and Photonics, 2018, p. 105800F.

[174] K. Dei, S. Schlunk, A. Luchies, D. Brown, and B. Byram, "Assessment of tissue boundary delineation using fundamental and harmonic ADMIRE and SLSC for per-

cutaneous biopsy guidance," in *Ultrasonics Symposium (IUS), 2018 IEEE International*. IEEE, 2018, pp. 1–4.

[175] M. Ashfaq, S. S. Brunke, J. J. Dahl, H. Ermert, C. Hansen, and M. F. Insana, "An ultrasound research interface for a clinical system," *Ultrasonics, Ferroelectrics, and Frequency Control, IEEE Transactions on*, vol. 53, no. 10, pp. 1759–1771, 2006.

[176] C. C. Cheung, C. Alfred, N. Salimi, B. Y. Yiu, I. K. Tsang, B. Kerby, R. Z. Azar, and K. Dickie, "Multi-channel pre-beamformed data acquisition system for research on advanced ultrasound imaging methods," *IEEE transactions on ultrasonics, ferroelectrics, and frequency control*, vol. 59, no. 2, pp. 243–253, 2012.

[177] P. Kaczkowski, "Arbitrary waveform generation with the verasonics research ultrasound platform."

[178] C.-C. Shen, Y.-H. Chou, and P.-C. Li, "Pulse inversion techniques in ultrasonic nonlinear imaging," *Journal of Medical Ultrasound*, vol. 13, no. 1, pp. 3–17, 2005.

[179] M. Jakovljevic, G. E. Trahey, R. C. Nelson, and J. J. Dahl, "In vivo application of short-lag spatial coherence imaging in human liver," *Ultrasound in medicine & biology*, vol. 39, no. 3, pp. 534–542, 2013.

[180] D. Hyun, G. Trahey, M. Jakovljevic, and J. Dahl, "Short-lag spatial coherence imaging on matrix arrays, part 1: Beamforming methods and simulation studies," *IEEE transactions on ultrasonics, ferroelectrics, and frequency control*, vol. 61, no. 7, pp. 1101–1112, 2014.

[181] J. J. Dahl, M. S. Soo, and G. E. Trahey, "Spatial and temporal aberrator stability for real-time adaptive imaging," *Ultrasonics, Ferroelectrics, and Frequency Control, IEEE Transactions on*, vol. 52, no. 9, pp. 1504–1517, 2005.

[182] M. Jakovljevic, B. Byram, D. Hyun, J. Dahl, and G. Trahey, "Short-lag spatial coherence imaging on matrix arrays, part ii: Phantom and in vivo experiments," *IEEE transactions on ultrasonics, ferroelectrics, and frequency control*, vol. 61, no. 7, pp. 1113–1122, 2014.

[183] J. Kirkhorn, "Introduction to IQ-demodulation of RF-data," *IFBT, NTNU*, vol. 15, 1999.

[184] A. Degirmenci, D. P. Perrin, and R. D. Howe, "High dynamic range ultrasound imaging," *International journal of computer assisted radiology and surgery*, vol. 13, no. 5, pp. 721–729, 2018.

[185] Y. Xiao, M. Boily, H. S. Hashemi, and H. Rivaz, "High-dynamic-range ultrasound: Application for imaging tendon pathology," *Ultrasound in medicine & biology*, vol. 44, no. 7, pp. 1525–1532, 2018.

[186] D. Hyun, G. E. Trahey, and J. J. Dahl, "Real-time high-framerate in vivo cardiac SLSC imaging with a gpu-based beamformer," in *Ultrasonics Symposium (IUS), 2015 IEEE International*. IEEE, 2015, pp. 1–4.

[187] M. K. Jeong, S. J. Kwon, C. D. Park, B. S. Kim, S. H. Chang, and K. S. Jang, "Ultrasonic imaging research platform with gpu-based software focusing," in *Ultrasonics Symposium (IUS), 2017 IEEE International*. IEEE, 2017, pp. 1–4.

[188] K. J. Haworth, K. B. Bader, K. T. Rich, C. K. Holland, and T. D. Mast, "Quantitative frequency-domain passive cavitation imaging," *IEEE transactions on ultrasonics, ferroelectrics, and frequency control*, vol. 64, no. 1, pp. 177–191, 2017.